NTNU
Norwegian University of
Science and Technology

Stability Analysis of Preikestolen

Katrine Mo

Ingeniørgeologi
Masteroppgave 60p

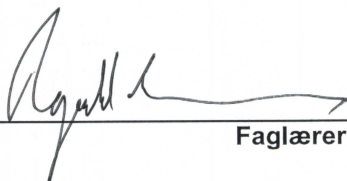|	
Studentens navn:	Katrine Mo
Studieretning:	Ingeniørgeologi
Tittel:	Stability analysis of Preikestolen
Faglærer:	Reginald Hermanns
Samarbeidspartner, bedrift el.l:	Norges Geologiske Undersøkelse

Utfyllende tekst for oppgaven:

Preikestolen is one of Norway's most famous rock formations hanging approximately 600 m above Lysefjorden. Although the rock face is visited by more than 100.000 of tourists every year, no stability analysis has been carried out. The assignments will focus on a comparison of several remote sensing techniques (ground based LIDAR scanning, photogrammetry from helicopter and drone) for structural data extraction. These will be compared with data taken in the field by field mapping. Based upon those various types of data a kinematic analysis will be carried out. This kinematic analysis will be the basis for stability modeling including data taken in the field and rock mechanical tests from the lab. A numerical model will be produced in RS^2 (previously Phase^2) and used as basis for the stability anlysis. Furthermore a hazard and risk classification will be carried out following the standards from NGU.

Supervisor: Reginald Hermanns, NTNU/NGU
Cosupervisor: Martina Böhme, NGU

Innleveringsfrist: 29.05.2018

Faglærer

Summary

The Geological Survey of Norway (NGU) in currently in the process of mapping all unstable slopes in Rogaland county. This master thesis is included as a supplementary part of this and focuses on the stability assessment of Preikestolen. The stability was investigated through structural mapping in the field supported by 3D analyses, using LiDAR and photogrammetry (drone and single lens reflex camera). In addition, a 2D numerical analysis was carried out in the RS^2 program, with calculations of the factor of safety.

Detailed geological mapping of Preikestolen revealed that the rock formation consist of two lithologies. The upper and lower part consist of porphyritic granite devided by a section of granitic gneiss. Structurally the study area can be divided in three domain with Preikestolen being the central one. The area is characterized by two steep joint sets J1 (213/87) and J2 (126/86), in addition to the shallower dipping joint set J3 (141/52). All the structures were mapped in the field and on the high resolution 3D models. The orientation of joints is indistinguishable, as they are almost identical in all models. However there is a variance in the foliation measurements. Field data indicate a dip towards the NW, while the 3D data suggest a dip towards SW.

Three remote sensing techniques were used to create 3D models of Preikestolen, including ground based LiDAR scanning, photogrammetry with drone and photogrammetry from helicopter (with a Nikon D 800 camera). A relatively high focus on remote sensing techniques is present throughout this thesis, as was requested by NGU. The main focus of the 3D models in this study, was the use for structural mapping. Based on the compared data sets, the photogrammetry models were evaluated as sufficient replacements for the ground based LiDAR scanner, dependent on several factors. Therefore throughout planning prior to fieldwork, and knowledge on how the different factors like vegetation, light conditions, accessibility in field, among others, are evaluated as important to successfully decide which remote sensing technique that will be most suitable for the specific site.

The input parameters for the numerical model were gathered both in the field and though laboratory testing of rock-samples from Preikestolen. The stress used in the model is based on existing in-situ stress measurements from the area along Lysefjorden, as there were no existing measurements at Preikestolen. The geometry of the model is based on a high quality point cloud produced with photogrammetry that was rasterized and combined with an existing 10 m digital elevation model.

The numerical simulation includes three versions of the slope (Model 1, 2 and 2a). Model 1 is an elastic model with the Hoek-Brown failure criterion. In model 1, only the profile of the rock formation was included. Model 2 was simulated as plastic material, with the joint extensions observed in the field included. In model 2a (plastic material), the joint was extended in order to daylight the slope. For model 2 and 2a, the Mohr-Coulomb failure criterion was applied. The simulation of model 2 resulted in a high critical strength reduction factor as the joints present at the plateau does not fully go through the rock mass at the toe of the slope. However, even when this joint was extended, the safety factor was still high. In the numerical model, the failure occurs through the joint located at the back

end of the plateau, which is defined as scenario A.

Furthermore, observations from the field and 3D models are included in a risk-matrix. One matrix was made for each of the scenarios, where scenario B has the highest hazard score. The join crossing the plateau, which is the back fracture in scenario B, is fully developed. For scenario A, the fracture is only partly developed across the slope which contributed to the lower hazard score. The hazard score for both models have a large uncertainties, as no data on acceleration, displacement rates or bathymetric data (past events) exists. Updating of the hazard score once measurements from the extensometers at Preikestolen are available, is therefore recommended.

Sammendrag

Norges Geologiske Undersøkelse (NGU) er n i prosessen med å identifisere og kartlegge ustabile fjellpartier i Rogaland. Denne masteroppgaven er en del av kartleggingen og har fokusert på å gi en første indikasjon på stabiliteten av Preikestolen. Dette er gjort ved hjelp av en standard strukturgeologisk kartlegging i felt samt ved hjelp av 3D-modelleringer. I tillegg er det kjørt en numerisk analyse i RS^2, der sikkerhetsfaktoren er kalkulert.

Detaljerte undersøkelser av geologien i felt, har vist at Preikestolen består av to bergart-styper. Øvre og nedre del av fjellformasjonen består av porfyryttisk granitt, mens den midterste delen består av granittisk gneis. Med bakgrunn i strukturene målt i felt, er området delt inn i tre domener, der Preikestolen er en del av domene 2. Området er karakterisert av de to bratte sprekkesettene J1 (213/87) og J2 (126/86), i tillegg til det slakere sprekkesettet J3 (141/52). Alle strukturer ble kartlagt både i felt og ved hjelp av 3D-modeller. Orienteringen av sprekkesettene er nærmest identisk for samtlige av stereonettene. Derimot viser foliasjonen en annen orientering i data fra 3D modellene sammenlignet med data fra felt.

I tillegg til selve analysen av stabiliteten er det lagt stor vekt på remote sensing, da det var ønskelig fra NGU sin side. Tre metoder for 3D-modellering ble benyttet, henholdsvis bakkebasert laser-scanning (LiDAR), fotogrammetri fra drone og fotogrammetri fra helikopter ved bruk av speilreflekskamera (Nikon D 800). Ettersom LiDAR tidligere har vært standard metode for NGU, både for å måle deformasjon og for strukturmålinger, var det en målsetting å sammenligne bakkebasert LiDAR med fotogrammetri for å evaluere hvilken som er best egnet som standard metode. Ettersom det kun ble gjennomført undersøkelser av strukturer, og det ikke eksisterer flere serier av målinger, er det strukturgeologiske undersøkelser som har vært hovedfokuset når modellene er sammenlignet. Basert på modellene som ble produsert, ble fotogrammetrimodellene vurdert som gode erstatninger for LiDAR, avhengig av flere stedegne faktorer for lokaliteten. Derfor er god planlegging av feltarbeid, samt kjennskap til området i forhold til fremkommelighet, vegetasjon, etc. vurdert som viktige faktorer for å bestemme hvilken teknikk som er best egnet.

Input-verdier i den numeriske modellen er samlet inn enten i felt, eller gjennom tester av bergartsegenskaper i laboratoriet. Spenningene i modellen er riktignok hentet ut fra eksisterende litteratur, ettersom måling ikke var gjennomførbart ved Preikestolen. Geometrien ble definert basert på en rasterisert høykvalitets punktsky, ettersom en digital terrengmodell på 1 m ikke eksisterer enda for Preikestolen.

Tre modeller ble undersøkt i RS^2, inkludert en modell uten sprekker, der Hoek-Brown er brukt som bruddkriterium, og bergarten er satt som et elastisk materiale. Modell 2 inkluderer sprekker med utbredelse som ble observert i felt. Modell 2a inneholder noen modifikasjoner av sprekkene, for simulering av et verst tenkelig scenario. Både model ell 2 og 2a er kjørt som plastiske materialer, der Mohr-Coulomb er satt som bruddkriterium. Simuleringene resulterte i høye sikkerhetsfaktorer, ettersom sprekkene fra toppen av platået ikke gjennomsetter berget helt, og relativt intakt berg må knuses opp for å kunne

resultere i en utglidning. Selv med en forlengelse av sprekken ut i dagen forble sikkerhetsfaktoren relativt høy. I den numeriske modellen oppstår bruddet igjennom sprekken lokalisert bakerst på platået, som er scenario A.

Videre er de observasjonene som ble gjort i felt og i 3D modellene inkludert i en risikomatrise. Matrisen ble laget både for scenario A og scenario B, der scenario B resulterte i høyest fareklasse. Sprekken i scenario B krysser platået på Preikestolen, og er fullt utviklet over hele platået, som gir den en høyere score enn scenario A. Dette er fordi sprekken i scenario A bare er delvis utviklet, og kun fullt åpen på en side av platået. Begge farevurderingene har store usikkerheter, ettersom data om akselerasjon, bevegelseshastighet eller betymetri ikke eksisterer per dags dato for Preikestolen. En oppdatering av risiko og fareklassifisering er derfor anbefalt når slike data er tilgjengelig.

Preface

This thesis is the final work of my master's degree in geology at NTNU. The thesis accounts for 60 stp and is written over one year (fall 2017/spring 2018). The thesis is written in collaboration with the Geological Survey of Norway, supervised by Reginald Hermanns (NTNU/NGU) and Martina Böhme (NGU).

First of all I would like to thank my main supervisor, Reginald Hermanns, for important feedback and useful discussions. Also thanks to both you and the others at NGU for the decision of focusing a masters thesis on Preikestolen, and for trusting me with this topic. I am very grateful for this opportunity.

Secondly I want to thank Martina Böhme, which has answered all of my questions with the greatest interest and energy. She also used a lot of time to help me with the large amount of software used in this thesis.

Also Nicolet Pierrick (NGU) was of great importance for this thesis, as he made the photogrammetry models, and has answered all my questions regarding the photogrammetry.

Professor Bjørn Nilsen at NTNU has my biggest gratitude, for giving important information about the input parameters in the numerical model. This was highly appreciated.

Furthermore I have to mention Gunnar Vistnes (NTNU) and Joakim Eggen (SINTEF), as they helped me with preparing the rock samples, and carry out the laboratory tests.

My fellow "fjellskred"-student, that I spent a lot of time with in the field during the summer and fall of 2017, Hermann Berntsen, also has my biggest gratitude.

My dad deserves a huge thank you for accepting the (challenging) task of correcting the grammar in large parts of this thesis. Your comments have been of great importance. Also thanks to both Christine and Andreas who assisted me by reading through parts of this thesis.

Last but not least, I would like to thank both of my parents for being supportive and interested in my study. Of course my three siblings needs to be mentioned here as well, as they are all extremely hard workers within their field of interest. You have all given me inspiration and motivation to finish this thesis.

Trondheim - May 29, 2018
Katrine Mo

Table of Contents

List of Tables

List of Figures

Abbreviations

NGU	=	Geological Survey of Norway
NVE	=	Norwegian Water Resources and Energy Directorate.
JRC	=	Joint Roughness Coefficient
JCS	=	Joint wall Compressive Strength
GSI	=	Geological Strength Index
SRF	=	Strength Reduction Factor
CSRF	=	Critical Strength Reduction Factor
ISRM	=	International Society for Rock Mechanics
ALS	=	Airborne Laser Scanning
TLS	=	Terrestrial Laser Scanning
DEM	=	Digital Elevation Model
LiDAR	=	Light Detection and Ranging
NTNU	=	Norwegian University og Science and Technology
FEM	=	Finite Element Method
SSR	=	Shear Strength Reduction
UCS	=	Uniaxial Compressive Strength
SfM	=	Structure from Motion
UAV	=	Unmanned Aerial Vehicle
SLR	=	Single Lens Reflex
FS	=	Factor of Safety

Chapter 1

Introduction

1.1 General Introduction

Since the first recorded landslide in Norway, more than 4000 humans have lost their life in different types of landslides (Furseth, 2006). The process of landslides plays an important role in the development of landscapes in Norway due to glacial effects and adverse climate conditions (Hermanns et al., 2012a). During several glaciations, intensive erosion carved out large fjord systems (Vorren and Mangerud, 2008). The glaciations resulted in an extensive coastline, containing both areas below marine limit with sensitive clay, and over steepened rock slopes.

Steep slopes facilitate hazards connected to slides and flows, dependent on the slope degree, aspect and geological conditions. Slopes with a slope degree above 30° and below 45° can be appropriate release areas for snow avalanches, while a slope degree of more than 45° often is connected to rock fall activity. In western Norway, hazards connected to steep mountain sides and the potentially secondary effects are considered problematic. Such secondary effects will vary based on several factors, such as the geological conditions and topography at the location. Rock slope failures within fjords can cause huge displacement waves, while rock slope failures in valleys can lead to damming of rivers resulting in destructive floods. During the last century, incidents where rock avalanches have triggered displacement waves have occurred several times and often been catastrophic as many of them have resulted in a large amount of casualties (Blikra et al., 2006; Hermanns et al., 2012a, 2013c).

From 1905 to 1936, three rock slope failures in western Norway caused large displacement waves with disastrous results (Harbitz et al., 2014). These occurred in Loen (1905 and 1936) and Tafjord (1934) and lead to a total of 175 casualties (Oppikofer et al., 2016b). There are several examples of similar events, like Tjelleskredet in Romsdalen (1756), where a 15 mill m^3 rock slope failure generated a 50 m high displacement wave, resulting in 32 fatalities (Jørstad, 1956; Sandøy et al., 2017). Counties dominated by steep mountain sites combined with deep fjords, like Sogn og Fjordane, Troms and Møre og Romsdal, are the most exposed to such hazards (Blikra et al., 2006; Grøneng, 2010). However, large rock avalanche deposits have also been identified in Hordaland and Rogaland

(NGI, 2014).

Large scale rock slope failures will also occur in the future (Hermanns et al., 2013a). The fact that large rock slope failures can be extremely destructive when they eventually occur, makes them important to understand and potentially predict. Whereas several techniques for preventing quick clay instabilities, and mitigation structures for snow avalanches and rock falls have been put up the last years, it is rarely possible to mitigate for a large scale rock slope failure. As there are no physical measures that can control a large scale rock slope failure (Hermanns and Longva, 2012), it is extremely important to investigate potentially unstable slopes, and calculate the effected area.

The Geological Survey of Norway (NGU) is now in the process of mapping all potentially unstable mountain sides in Norway, financed by the Norwegian Water and Energy Directorate (NVE) (Hermanns et al., 2013b,a). More than 250 unstable slopes have been identified, whith post glacial deformation (Oppikofer et al., 2015, 2016b). This thesis is part of a sub project at NGU, where all the potentially unstable rock slopes in Rogaland county in western Norway are mapped.

Through the years, several attempts have been made to determine the deformation rate of the large joint that crosses Preikestolen. In 1930, Turistforeningen (the tourist organization) in Rogaland, put up bolts on each side of the main joint visible on the plateau. However, there is a large uncertainty about how long they continued the measurements, as there were no recordings when no movement was detected. From 1991 to 2014 the municipality of Forsand measured the joint. They measured a slight increase in the joint in 2013, but the measurements were back to normal in 2014. After the 2014 season, no further measurements were taken. Previous of this study, the consultant company SWECO investigated both the stability of smaller blocks on the plateau of Preikestolen (Rohde, 2017). The report from SWECO is based on the preliminary results from the fieldwork done in this thesis.

Due to the enormous amount of visitors each year, and the location directly above the fjord, it was decided by NGU to focus a master thesis about the stability of the rock formation. This is the background for the thesis: *Stability analysis of Preikestolen*. A throughout investigation of the stability, using modern techniques will hopefully contribute to a better understanding of the geological conditions and the stability of Preikestolen.

1.2   Aim of Study

The main goal of this study is to determine the stability of Preikestolen. The stability will be investigated through laboratory work combined with numerical modelling, in addition to a structural analysis of the discontinuities based on field data and data obtained from photogrammetry and terrestrial laser scanning (LiDAR).

LiDAR and photogrammetry from both drone and helicopter will be used to create 3D models of the rock slope. These techniques will be compared, to discuss which model that is of better quality, and therefore will work best as a standard method. Previously, the LiDAR scanner has been used as a standard method by NGU both for displacement measurements, and for structural mapping. It was therefore requested to do a comparison of the 3D-modelling tools, to consider the possibility of introducing photogrammetry to the previously standard procedure with the LiDAR scanner.

The stability analysis will be focused on a kinematic feasibility test, based on structure measurements in field in addition to those from Coltop 3D. In addition, a 2D model of the rock formation is made in the numerical analysis program RS^2. This model will be based on topography from the best Digital Elevation Model (DEM) obtained through 3D modelling, in addition to parameters from lab testing and field measurements. Further the stability of the rock formation will be discussed based on existing literature and obtained results. The remote sensing investigation techniques will be discussed and evaluated to recommend a potentially best method. Recommendations for further work and focuses will eventually be presented.

1.3 Introduction to Area

Rogaland county is located in the southwestern part of Norway (Figure 1.1), with Hordaland to the north, and Vest-Agder to the east. West of Rogaland lies the North Sea, hence the area has a coastal climate which is dominated by relatively warm winters and cool summers. The county is not associated as most exposed for rock avalanches, especially if compared to county's like Sogn og Fjordane and Møre og Romsdal. However, there are steep mountain sites and fjords especially towards the east of Rogaland.

Several pre-historical rock avalanche deposits have also been observed in Rogaland (NGI, 2014), which is a indisputable indicator that the county is prone to rock avalanches. Several rock slide dams were mapped by Jakobsen (2016) as part of a MSc project at NTNU, supporting the existence of several historical and pre-historical rock slope failures. In addition there are several identified instabilities, like the Tytefjellet rock slope, mapped by Rem (2016), this was also a MSc project at NTNU. Rogaland is described by Hermanns et al. (2013b) as a medium-high priority county when it comes to rock slope failures.

During the last glaciation, Rogaland was frequently covered by huge amounts of ice (Aarseth et al., 1997), which in combination with the holocene isostatic rebound produced deep fjords combined with steep rock walls. Norways potentially most famous rock formation, Preikestolen (also known as Pulpit Rock), is located at the northern side of the fjord, Lysefjorden, in Forsand municipality. Lysefjorden is an approximately 42 kilometer long fjord, and dominated by steep rock walls on each side. The area is popular among tourists due to the beautiful landscape, and several spectacular rock formations, like Preikestolen and Kjeragbolten. Approximately 250 thousand tourists visited the location in 2016.

1.3.1 Geological Framework

The bedrock in the area north east of Lysefjorden is described in the report from Slagstad et al. (2017), and is included in a geological map from NGU in scale 1:50 000 (Figure 1.2). The area around Lysefjorden is in general dominated by granites, and more specific the Sirdal Magmatic Belt (SMB) granite, which is a porphyritic granite dominated by larger feldspar crystals (Slagstad et al., 2013; Coint et al., 2015). The SMB granite is a Sweconorwegian igneous rock, and is in general massive, but also contains areas with signs of foliation. The other rock type present in the area is the granitic gneiss called Gyadalen paragneissess. This rock type is banded with thinner bands of amfibolite/pyribolitt , and is of Pre-Sveconorwegian age (Slagstad et al., 2013).
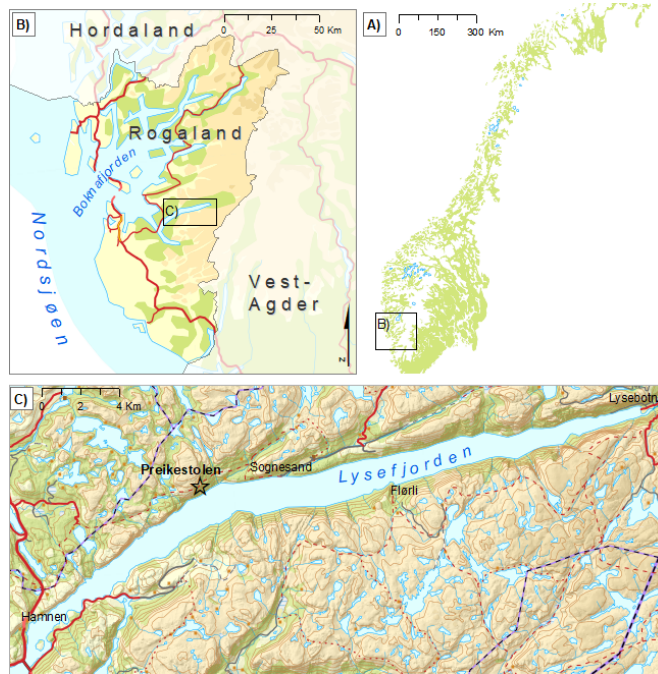
Figure 1.1: Overview map of the study area. Preikestolen is located on the northest side of Lyse-fjorden in Rogaland county, southwestern Norway.
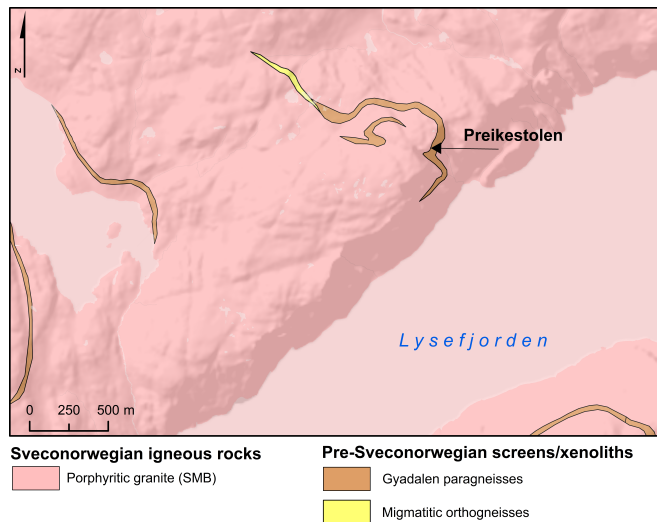
Figure 1.2: Bedrock in the area surrounding the study area is generally dominated by granite, in addition to some smaller areas with Pre-Sweconorwegian rocks. Data from NGU.

1.3.2   Available Data and Software Overview

Unfortunately, a high quality 1 m DEM is not yet available from Lysefjorden. Therefore, a 10 m DEM was used throughout this study. Otherwise, several of the used datasets were gathered in the field, which are described in chapter 3. The most important datasets used in this thesis, and their source are presented in table 1.1.

Table 1.1: The most important background data used in this thesis. The majority of the data-sets were gathered in the field by NGU, as limited data existed prior to this project.

Dataset	Use	Source
LiDAR	3D-modelling	Fieldwork with NGU
SLR Photos (from 09.00)	Photogrammetry	Fieldwork with NGU
SLR Photos (from 17.00)	Photogrammetry	Fieldwork with NGU
Drone Photos	Photogrammetry	Fieldwork with NGU
10m DEM	Background map	Available from Hoydedata.no

A large amount of software were used throughout this thesis. An overview of the software and their application, is briefly described in table 1.2. Further explanations were done of the most important software, where the understanding of the software, and the skill of the user is important in order to obtain a reliable result. Therefore, a more throughout explanation of Coltop 3D and RS^2 are included in chapter 2.3.3 and 3.5.3. In addition to the software mentioned in table 1.2, several software were used in connection to this thesis, like Litchi, which was used to define the drone route. However, these will not be mentioned further, as they were not specifically used by the author.

Table 1.2: Overview of the software used in this thesis. RS^2 and Coltop 3D are two important software, that will be further described in chapter 2.3.3 and 3.5.3.

Software	Use	Lisense from
ArcGIS	Creating maps	NTNU/NGU
DIPS 7.0	Stereonets and kinematic analysis	NTNU/NGU
RS^2	Numerical modelling	NTNU
Parser	LiDAR processing	NGU
Agisoft Photoscan	Photogrammetry processing	Free software
Polyworks V12 and V11	LiDAR processing	NGU
CloudCompare	Georeferencing and comparison of point clouds	Free software
RocData 5.0	Rock properties	NTNU
Coltop 3D	Structural measurements from point clouds	NGU

Chapter 2

Background Theory

2.1 Rock Slope Failures

Rock slope failures and instabilities are classified in several different ways, and a number of classification systems exist. The reason for the large variety of systems is a result of several disciplines being included in the study of landslides (Highland et al., 2008). The classification systems are based on factors like volume, failure mechanism or material type, dependent on the study field.

A classification system that combine the way of movement and type of material was developed by Varnes (1978). The Varnes classification system divides the movement into six groups; fall, topple, slide, spread, flow and complex slope movements, and the material into bedrock and engineering soils (Varnes, 1978). The Varnes system was updated by Hungr et al. (2014) and the upgraded version is widely used today. The classification system from Hungr et al. (2014) is rendered in table 2.1, and the typical landslide movements are shown in figure 2.1.

In Norway, the classification of failures in rock are often based on volume of the failed mass, and defines a rock avalanche (fjellskred) as a landslide containing rock with a volume exceeding 10 000 m^3 (NGI, 2014). However, NGU uses a minimum volume of 100 000 m^3 for a rock avalanche, because this definition is more in line with international standards (Devoli et al., 2011; Morken, 2017). Definitions based on volume do not include the several different types of failure mechanisms possible in large scale rock slope failures in the definition.

Due to a large variety of classification methods, it was decided to define a "rock slope failure" as described in Böhme (2014). Böhme (2014) defines a rock slope failure as *" a complete failure of a rock mass resulting in gravitational mass movements down a mountain slope"*, and rock slope instabilities as *"rock slopes that display signs of gravitational deformation and may form the sources of potential future rock slope failure"*. The definitions from Böhme (2014) will be used as a basis in this thesis, in addition to the volume characterization used by NGU.

Table 2.1: Classification system of landslides from Hungr et al. (2014) as presented in Nicolet (2017). Bold text represents failures that can reach velocities that are extremely rapid. The italic text represents words were only one of the mentioned materials should be used.

Type of movment	Rock	Soil
Fall	**1. *Rock/ice* fall**	**2. *Boulder/debris/silt* fall**
Topple	**3. Rock block topple** 4. Rock flexural topple	**5. *Gravel/sand/silt* topple**
Slide	6. Rock rotational slide **7. Rock planar slide** **8. Rock wedge slide** 9. Rock compound slide **10. Rock irregular slide**	11. *Clay/silt* rotational slide 12. *Clay/silt* planar slide **13. *Gravel/sand/debris* slide** 14. *Clay/silt* compound slide
Spread	15. Rock slope spread	**16. *Sand/silt* liquefaction spread** **17. Sensitive clay spread**
Flow	**18. *Rock/ice* avalanche**	19. *Sand/silt/debris* dry flow **20. *Sand/silt/debris* flowslide** **21. Sensitive clay flowslide** **22. Debris flow** **23. Mud flow** 24. Debris flood **25. Debris avalanche** 26. Earth flow 27. Peat flow
Slope deformation	28. Mountain slope deformation 29. Rock slope deformation	30. Soil slope deformation 31. Soil creep 32. Solifluction
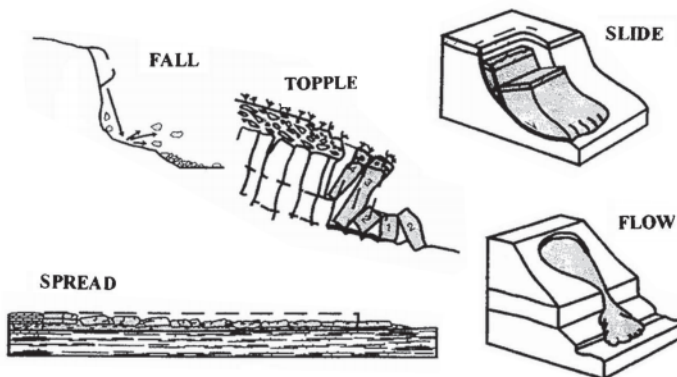
Figure 2.1: Typical landlside movements, as given in Nicolet (2017) after Cruden and Varnes (1996) and Hungr et al. (2014).

2.1.1   Stability of Rock Slopes

Several factors, both external and internal, can influence the stability of rock slopes. Internal factors like discontinuities are considered altered over time by the external factors such as earthquakes, erosion, climate among others (Böhme, 2014). Predominant structures in the rock often defines the geometry of a unstable rock slope (Kveldsvik et al., 2009). Such structures can include foliation, joints and faults among others. Saintot et al. (2011) highlights folding as a factor that will increase the likelihood of having discontinuities oriented favorable for sliding. The following list of factors that influence the slope stability, is presented by Grøneng (2010), including both external and internal factors.

- Slope topography

- Orientation of discontinuity planes and foliation

- Shear strength of discontinuities and intact rock

- Groundwater pressure

- In situ stress conditions

- Seismic activity

- Freezing/thawing effects

In which scale the different factors influence the stability are variable, but the orientation of discontinuities in addition to the groundwater conditions are considered the most important ones (Grøneng, 2010). Water can effect the slope stability in several ways, like diminishing the shear strength of the potential sliding plane by decreasing the normal stress (Wyllie and Mah, 2004). In addition to reducing the internal friction, expansion due to freezing and causing of erosion will also have negative effects on the stability (Grøneng, 2010). The destabilizing effect of groundwater is discussed in several studies of rock slope failures like Sandersen (1996) and Grøneng et al. (2011). The studies were carried out on various slopes in western Norway and both describes groundwater as an important factor for the slope stability.

When it comes to discontinuities, Wyllie and Mah (2004) describe the orientation of those as the main influencing factor. If a joint set is steeper that the friction angle of the discontinuity and daylights the slope surface it can work as a sliding plane (Hermanns et al., 2012b). But also factors like spacing and persistence of the discontinuity are important (Wyllie and Mah, 2004).

The failure of large rock slopes is often initiated by a longer phase of slow deformation, which is often interpreted as an initial stage of the slope collapse. Several creep mechanisms is described by Stead et al. (2006). These creep mechanism in generally connected to rock material with a low e-module as they can allow a large amount of deformation prior to failure.

2.1.2 Influence of Deglaciation on the Stability of Rock Slopes

Throughout the Quaternary, a number of glaciations have had a large effect on the landscape that exist in Norway today. Records show, that the highest frequency of large rock slope failures in Norway occurred after the last glaciation (Ballantyne, 2002). The deglaciation affected the rock slope stability in several ways. The following list, presented by Böhme (2014), summarize three effects that can lead to reduction of the rock slope stability.

1. **Oversteepeing of rock walls due to erosion**
   The over steepening of slopes is an effect of the glacial erosion, that shapes previous V shaped valleys to U shaped valleys. The erosion was concentrated where the ice movement was faster, which in general means that the valleys, where the ice streams were concentrated, was especially effected. This led to over-steepening of the valley sides, which changed the in-situ stress in the rock slope. An over-steepening of rock walls will lead to increased overburden shear stress within the rock and promote failure of the rock slope (Ballantyne, 2002). After the deglaciation, the altered stress conditions resulted in failure where the applied stress exceed the strength of the rock mass (Böhme, 2014). The post glacial valley shape is described as more prone to failure compared to slopes with constant inclination (Ambrosi and Crosta, 2011).

2. **Debuttressing of the valley walls**
   Removal of the support (ice) from the valley walls (debuttressing) may affect the stability of rock slopes (Ballantyne, 2002). In valleys occupied with valley glaciers, the stress level will increase both on the valley walls and the valley floor (Ballantyne, 2002; Böhme, 2014). This ice-load causes a compression of the rock that leads, when applied over a long time, to a deformation. This deformation is elastic and therefore stored in the rock as residual strain energy (Wyrwoll, 1977; Ballantyne, 2002). Following the melting of the ice is, unloading of the glacially stressed rock will release strain energy and reduce the confining pressure (Ballantyne, 2002; Böhme, 2014). The result is often areas with tensile stress behind the slope (Figure 2.2), which can create new joints or be localized in previously existing weakness zones (Böhme, 2014). One example from British Colombia is shown in figure 2.2, investigated by Bovis (1982) and Geertsema et al. (2006) where the debuttressing following the glacial melt back have lead to expansion of rock joints. This type of anti-slope scarps often appears due to post glacial deformation (Bovis, 1982).

3. **Isostatic uplift**
   During glaciations, the lithosphere in the areas covered by ice will be pushed down due to the heavy load of ice. When the ice starts retreating a lithosphere uplift will begin as a response to the removal of the loading. This isostatic uplift have had a large effect in Norway, as the marine limit can be seen above 200 m a.s.l. in the most extreme parts south-east in Norway. This uplift has been as large as 6mm/year in some parts of Norway (Vestøl, 2006; Böhme, 2014). Other than increasing the relief, no direct connection between the isostatic uplift and rock slope instabilities has yet been found (Böhme, 2014). However, the isostatic uplift was connected to the seismicity of Norway by Olesen et al. (2013). Even though the initial more

rapid uplift resulted in a period with relatively high seicsmicity, there is yet no good explanation on how the transition to todays low seismicity took place (Olesen et al., 2013). In general the remaining glacioisostatic adjustments are not considered to have a large effect on the seismicity in Norway today (Bungum et al., 2005).
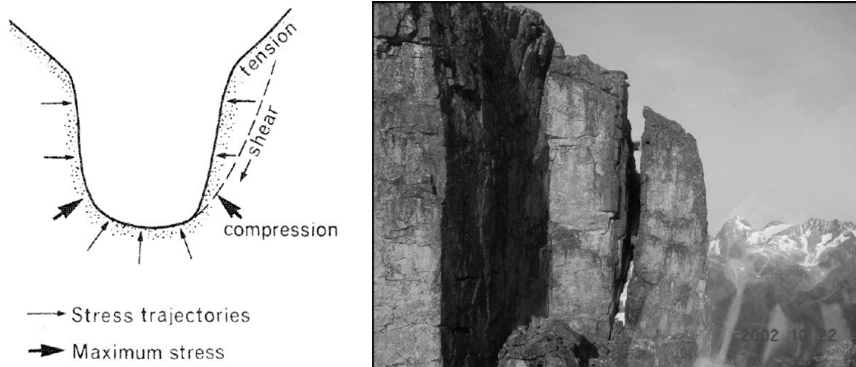
Figure 2.2: Left: The removal of ice within previously ice covered valleys can lead to tension in the upper part of the slope and shear in the valley walls. Right: Anti slope scarp in steep rock walls often appear in previously glaciated areas. Figure modified from Selby et al. (1982), Geertsema et al. (2006) and Böhme (2014).

2.1.3 Landslide Susceptibility and Hazard Assessment

NGU is currently in the process of mapping all potentially unstable rock slopes in Norway, since 2009 financed by NVE (Hermanns et al., 2014). To obtain an effective and well-organized work flow a work-chart given in Oppikofer et al. (2016a) is often used (Figure 2.3).
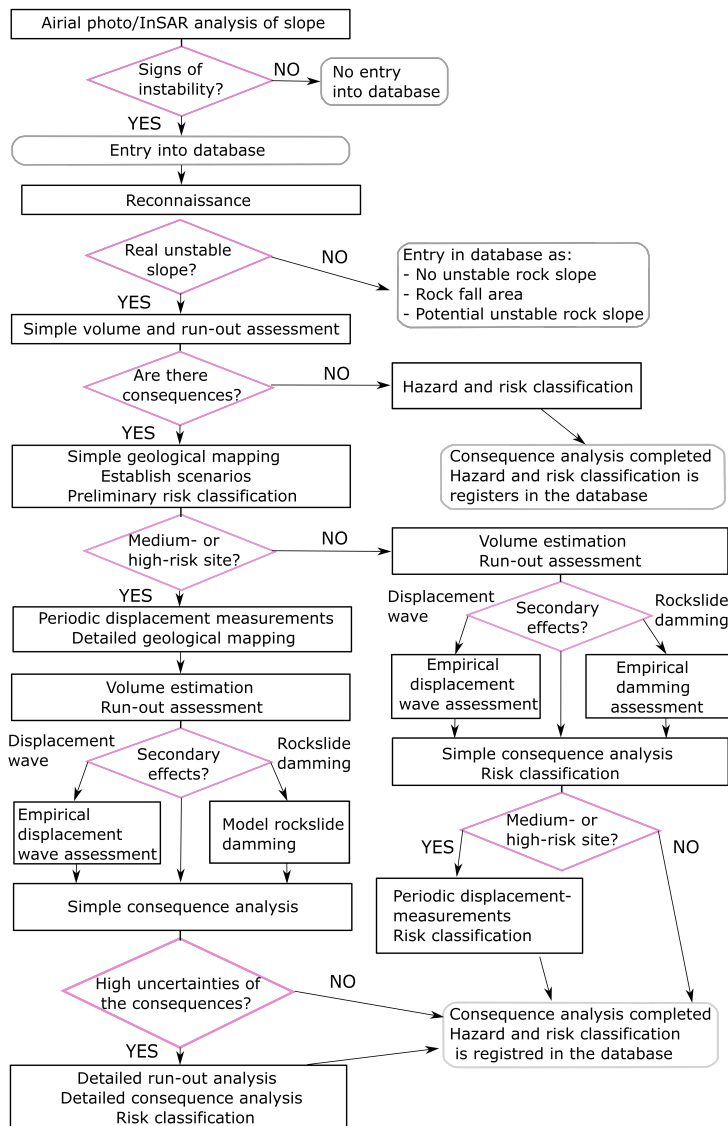
Figure 2.3: The standard work flow used by NGU for mapping unstable rock slopes. Figure modified from Oppikofer et al. (2016a) and Krogh (2017).

The first step of the investigation is studying slopes through aerial photographs and aerial LiDAR scans. In addition satellite based radar interferometry (InSAR) analysis can be used to detect movement. Furthermore, tips from locals are also taken into consideration when detecting slopes for reconnaissance (Hermanns et al., 2014). If there are no signs of instability, no further mapping of the slope is required, hence they are discarded at an early stage. If the slope shows signs of instability, the investigation continues with the following steps originally described by Hermanns et al. (2014).

1. **Reconnaissance**
   In this step, the site is investigated in the field or from helicopter. Rock slopes that are too small (rockfall problematic) or stable are included in the database as not relevant. Sites that could potentially be unstable but does not show signs of activity are registered. Such sites are later revised to make sure the conditions have not changed (Hermanns et al., 2014).

2. **Preliminary Consequence analyses**
   A relatively simple preliminary analysis of the consequences of a rock slope failure is carried out in this step. This includes volume estimations and automated run out analysis. Sites with no direct or secondary consequences are registered as low-risk sites, and are not investigated further. Unstable sites with a larger consequence will need further investigations following the chart.

3. **Simple Geological mapping**
   Simle geological mapping includes gathering information of the criteria that are necessary for the final hazard classification. The mapping consist of nine categories. Two of the categories are dependent on the structural settings, three are dependent on geomorphology and four is dependent on the deformation/activity. These categories are given points, and the result is plotted in a risk matrix.

   A preliminary hazard intard analysis is also carried out in this step, as described by Hermanns et al. (2012b, 2013a). The consequences are determined based on the potenital loss of life. The slopes that lie within the red area (Figure 2.4) will need a more throughout structural mapping, to decrease the level of uncertainty.

4. **Periodic displacement measurements and detailed geological mapping**
   In this step, it is only the medium or high risk sites that are investigated. This is generally to reduce the uncertainty in the geological conditions. One way to do this is to investigate the deformation rate. Several tools are used by NGU for this purpose, like exstensometers, dGNSS, InSAR and LiDAR amoung others (Hermanns et al., 2014).

   In the cases where deformation cannot be explained by simple geological mapping, a detailed geological mapping in the field is required. At such sited, the kinematic feasibility test will typically show that there are no signs of instability despite the ongoing deformation. Such sites generally have a rather complex geology, and can include a combination of several failure mechanisms (Hermanns et al., 2014).
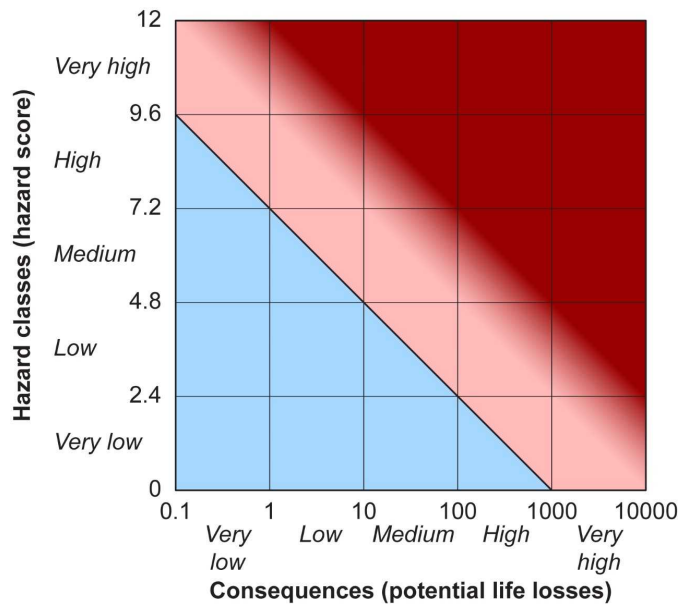
Figure 2.4: Risk matrix defining the probability and risk of rock slope failures. The hazard class defined by the structural mapping is plotted on the y-axis, while the consequence is defined in the potential life losses and is plotted on the x-axis. Figure from (Hermanns et al., 2013a).

5. **Establish scenarios and Hazard and risk classification**

   In this step, the different scenarios for the slope are defined. Such scenarios are defined based on a combination of both structural and morphological mapping, in addition to investigation of the displacement measurements. Further a run out analysis of the scenarios is carried out. This also includes simulations of the secondary effects, such as displacements waves. After the hazard and automated run out analysis, the risk classification is carried out. The classification system is scenario-based, and evaluates both the probability of a rock slope failure and the secondary effects. In cases where the uncertainties of the consequences are large, the automated runout analysis will not be sufficient, and a detailed run-out analysis will be necessary (Hermanns et al., 2014).

In this study, the focus will be on the geological mapping, and to establish scenarios. Hence no run out analysis or deformation measurements will be carried out. Thus a very preliminary hazard and risk classification will be presented in this study. This matrix will optimally be revised when data from the extensometers can be included. However, the hazard and risk classification can be used as a good basis when discussing the stability.

2.2 Rock Mechanics and Classification Systems

2.2.1 Mohr-Coulomb Failure Criterion

The Mohr Coulomb criterion is an expression of the shear strength of the rock mass on the sliding surface (Wyllie and Mah, 2004). Coulomb's law of shear strength defines rock as a coulomb material where the shear strength of a sliding surface is defined by the friction angle and the cohesion (Wyllie and Mah, 2004). Mohr-Coulomb is the most common failure criterion encountered in the field of technical engineering, and is a linear failure criterion. The direct shear formulation is given by the following equation.

$$\tau = c + \sigma_n tan\phi \qquad (2.1)$$

where τ is the shear stress along the failure plane, σ_n is the normal stress on the failure plane, c is the cohesion and ϕ is the friction angle. The relationship between the parameters is described in figure 2.5.
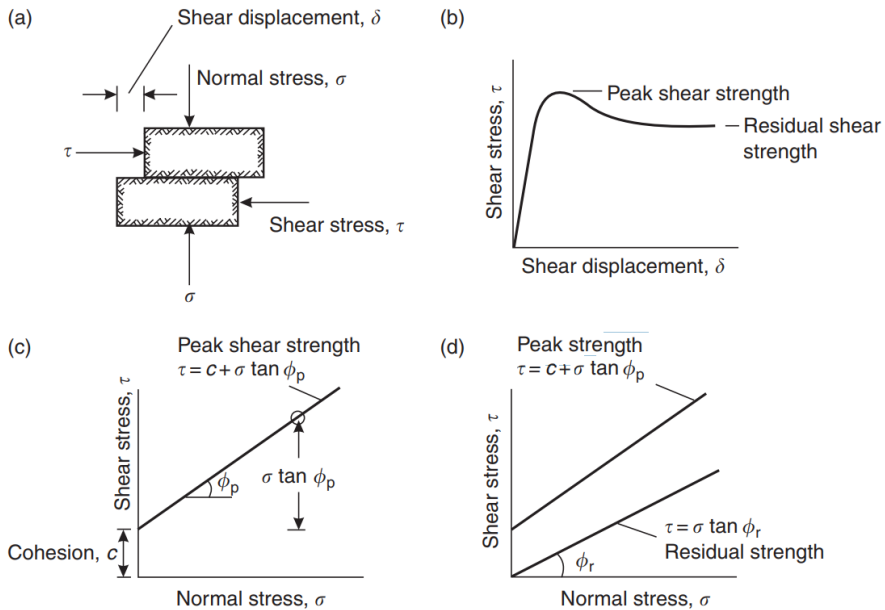
Figure 2.5: (a) Shear testing of a sample containing a discontinuity.; (b) Shear displacements plotted against the shear stress.; (c) Mohr plot with the peak shear strength of a material with cohesion, c, and basic friction which in this example is ϕ_p.; (d) Plot with both the peak strength, and the residual strength of a material. Figure from Wyllie and Mah (2004).

2.2.2 Bartons Estimate of Shear Strength

Several modifications of the Mohr-Coulomb criteria exist, like the one presented by (Patton et al., 1966) that experimented with the strength of saw-tooth specimens. Patton et al. (1966) proved that the undulations and regulations on a natural surface was important for the shear behavior, as it increases the strength of the surface which again is important for the stability. When the normal stress (σ_n) is low, Patton et al. (1966)'s equation is still valid:

$$\tau = \sigma_n tan(\phi_b + i) \tag{2.2}$$

where ϕ_b is the basic friction angle of the surface of the discontinuity and i is the inclination of the saw-tooth face.

However when the normal stress increases, the teeth will break of as the strength of the intact material is exceeded. This results in a behavior more in line with the intact strength of the material, rather than to the characteristics of the surface of the discontinuity, as mentioned in studies of nonlinear behavior by Barton (1973) and Barton (1976). In contrast to Patton et al. (1966), the investigations from Barton (1973) and Barton (1976) showed that the changes in the shear strength were gradual and not abrupt. The equation 2.2 was therefore rewritten as:

$$\tau = \sigma_n tan\left(\phi_b + JRClog_{10}\left(\frac{JCS}{\sigma_n}\right)\right) \tag{2.3}$$

where τ is the shear strength, σ_n is the normal stress, the ϕ_b is the basic friction angle, JRC is the joint roughness coefficient and JCS is the wall compressive strength. Equation 2.3 was later revised by Barton and Choubey (1977) to the following equation.

$$\tau = \sigma_n tan\left(\phi_r + JRClog_{10}\left(\frac{JCS}{\sigma_n}\right)\right) \tag{2.4}$$

where ϕ_r is the residual friction angle. Barton and Choubey (1977) suggested that the residual friction angle could be determined by the equation below, where r is the wet rebound number from a Schmidthammer test on a weathered surface, and R is the rebound number of a dry and unweathered sample:

$$\phi_r = (\phi_b - 20) + 20(r/R) \tag{2.5}$$

Equation 3.6 and 3.7 are part of the Barton-Bandis criterion (Barton and Bandis, 1991). However, for most natural unweathered surfaces both the residual and basic friction angle will be approximately equal (Bandis, 1993). The basic friction angle can be obtained through a tilt test, which will be described in chapter 3.5.2. According to Barton (1973), the residual friction angle can be assumed equal to the basic friction angle for natural joints.

Joint Roughness Coefficient (JRC)

The Joint Roughness Coefficient (JRC) value describes the roughness of the sliding plane. This empirical index can be measured several ways, like comparing the roughness profile of the surface to standard profiles or measuring the asperity amplitude in the field (Wyllie and Mah, 2004). The JRC can be determined by holding a 1 m straight ruler onto the surface of a plane and measuring the three largest amplitudes from the ruler to the rock. Further, the final JRC value is then determined from the chart shown in figure 2.6. When using the setup in figure 2.6, the scale should not be corrected for (Kveldsvik et al., 2008).
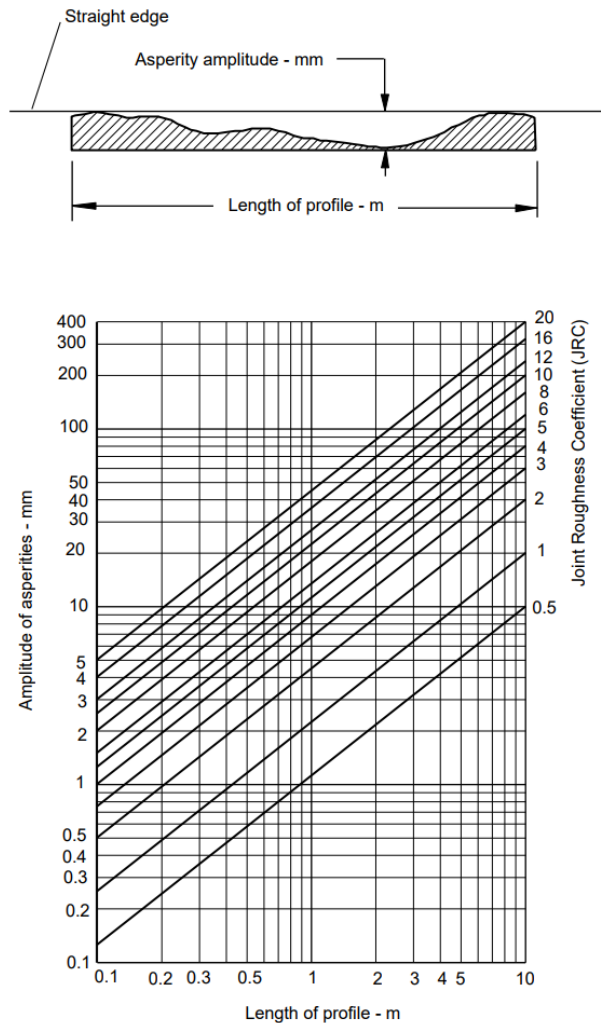
Figure 2.6: Principle of measuring the JRC based on a straight ruler. The profile length and the amplitude of the asperties are used to determine the JRC number. Figure from (Barton et al., 1978; Hoek, 2007).

Joint Compressive Strength (JCS)

The Joint Compressive Strength (JCS) is defined as the compressive strength of the rock wall, which can differ from the UCS mainly due to weathering of the surface rock. For joint surfaces that shows little degree of weathering, the UCS and the JCS can be assumed equal (Barton and Choubey, 1977). According to Wyllie and Mah (2004), an easy field estimate will often be adequate as a basis for estimating the JCS. The Schmidt hammer test is also a method of estimating the compressive strength of the surface of the discontinuity as proposed by Deere and Miller (1966).

In the case of Preikestolen, the value used as JCS was estimated to be similar to the Uniaxial Compressive Strength (UCS), as there was no possibility of collection Schmidthammer measurements in the field.

2.2.3 Generalized Hoek-Brown Criterion

The Hoek-Brown failure criterion was originally developed in 1980 by Hoek and Brown (Hoek and Brown, 1980b,a). A major revision was carried out by Hoek et al. (2002), to make the criterion more appropriate to use in numerical models. The criterion was developed to obtain a method for estimation of rock mass strength based on the geological conditions present (Eberhardt, 2012). The failure criterion is based on an empirical relationship and is used to describe the non-linear increasing strength of the rock when the confining stress is increased (Eberhardt, 2012). Included in the criterion are procedures for estimating rock mass strength from laboratory testing and observations in the field (Eberhardt, 2012). To use the Generalized Hoek-Brown criterion, the σ_{ci}, m_i and GSI (Chapter 2.2.4) must be known.

The Generalized Hoek-Brown failure criterion for jointed rock masses is defined in the following formula from Hoek (2007):

$$\sigma_1' = \sigma_3' + \sigma_{ci}\left(m_b \frac{\sigma_3'}{\sigma_{ci}'} + s\right)^a \tag{2.6}$$

Where σ_1' and σ_3' represent maximum and minimum effective principal stresses at failure. The uniaxial compressive strength (σ_c) can be obtained by setting $\sigma_3' = 0$ (Wyllie and Mah, 2004). In formula 2.6, m_b is a reduced value of the material constant (m_i) and dependent on rock mass. Different values for m_i are defined from a standard table from Wyllie and Mah (2004) based in the rock type and texture. m_i is also explained as a curve fitting parameter by Eberhardt (2012) which is found through triaxial testing of intact rock samples. m_b is defined by the following equation 2.7 from Hoek et al. (2002). The uniaxial compressive strength of the intact rock is included as σ_{ci} (Hoek, 2007). The constants s (a measure of how fractured the rock is) and a are dependent on the rock mass characteristics. For intact rock, s=1. The constants s and a are given by the equations 2.8 and 2.9 defined in Hoek et al. (2002).

$$m_b = m_i exp\left(\frac{GSI - 100}{28 - 14D}\right) \tag{2.7}$$

$$s = e^{\left(\frac{GSI-100}{28-14D}\right)} \tag{2.8}$$

$$a = \frac{1}{2} + \frac{1}{6}\left(e^{\frac{-GSI}{15}} - e^{\frac{-20}{3}}\right) \tag{2.9}$$

Where GSI is the Geological Strength Index, D is the disturbance factor, which depends on the degree of blast damage on the rock. The disturbance factor varies from 0 for undisturbed rock mass, to a maximum value of 1 for rock masses that are disturbed to a large degree (Wyllie and Mah, 2004). In the Hoek-Brown criterion, the constant, a, is replaced by the value 0.5.

The Hoek-Brown failure criterion differs from the Mohr-Coulomb linear failure as the Hoek-Brown criterion is non-linear (Figure 2.7). The non linear behaviour of the Hoek-Brown criterion agrees with the behaviour of rock tests in triaxial testing over a large range of confining stresses (Eberhardt, 2012). In addition to this advantage and the fact there is almost three decades of work, experience and data with the Hoek-Brown criterion, it also provides a relatively simple and empirical way to estimate the rock mass properties (Eberhardt, 2012).

However there are some limitations. As the Hoek-Brown failure criterion assumes that the rock is isotropic and behaves isotropic, the criterion should not be used if the block size is in approximately the same order as the structures (Hoek, 2007). Also it will be inappropriate to use the Hoek-Brown criterion when the investigated rock mass where there is a clearly defined orientation of a main structure. However the criteria must be used with care if the dominant discontinuity dips into the slope and the failure is through the rock mass (Marinos et al., 2007).
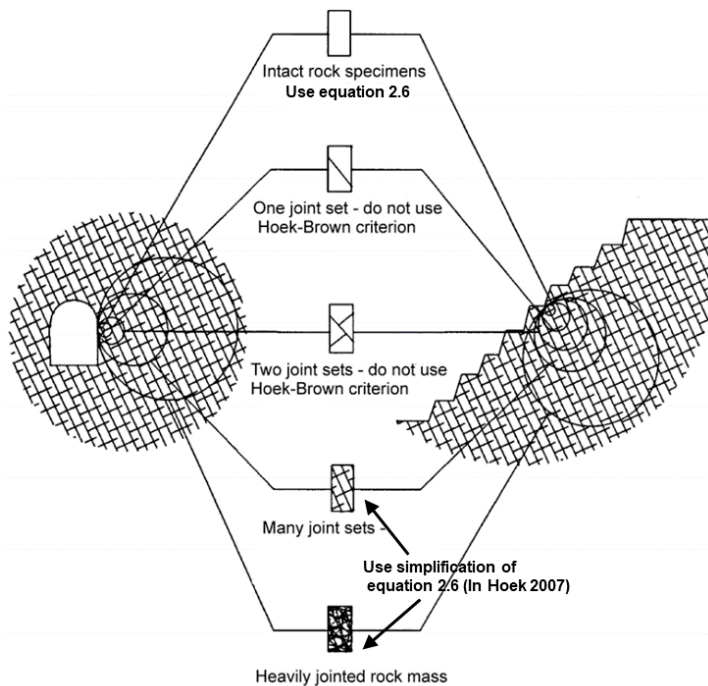
Figure 2.7: Diagram with an overview of the rock quality from intact rock specimens to heavily jointed rock mass. The samples are increasing in size, and shows which situation the criterion is appropriate. Figure modified from (Hoek, 2007).

2.2.4 Geological Strength Index (GSI)

The Geological Strength Index (GSI) described by Hoek (1994), Hoek et al. (2000), Marinos et al. (2005), Marinos et al. (2007) among others, is a system for characterization of rock mass. The system was originally developed in the rock mechanics field to meet the need for a reliable input for numerical analysis (Marinos et al., 2007). The GSI is an important input parameter when using the Hoek-Brown criterion (Marinos et al., 2007). The system presented in figure 2.8 applies for blocky rock masses (Hoek, 2007), and is used to define the GSI based on field observations. In cases where discontinuity spacing are large compared to the dimension of the slope, the GSI and Hoek-Brown criterion should not be used.
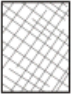
Figure 2.8: Basic table for determination of the GSI. The chart combines the blocky-ness of the rock and the surface quality of the discontinuity to estimate the GSI. Figure from Marinos et al. (2007).

2.3 Structural Geology

2.3.1 Stereo-graphic Projection

Stereo-graphic projection is a useful tool to present structural data in a way that it can easily be interpreted. At Preikestolen, the discontinuities were registered with dip and dip-direction measurements. The dip is defined as maximum inclination of the structure to the horizontal and the dip direction as the direction of the horizontal line in direction of the dip (Wyllie and Mah, 2004). The stereographic projection is used to interpret three dimensional data in a two dimensional stereonet, as the planes can be represented as points or great circles. The basic principle of stereographic projection is presented in figure 2.9.

There are several different software available, but in this case, DIPS 7.0 from the Rocscience package is used. DIPS is a stereographic projection program, designed for analysis of orientation based on geological data. DIPS will be used to display the structural information data gathered in the field, and through structural measurements gathered through the 3D model and the use of Coltop 3D. Also the kinematic feasibility test will be carried out in DIPS.
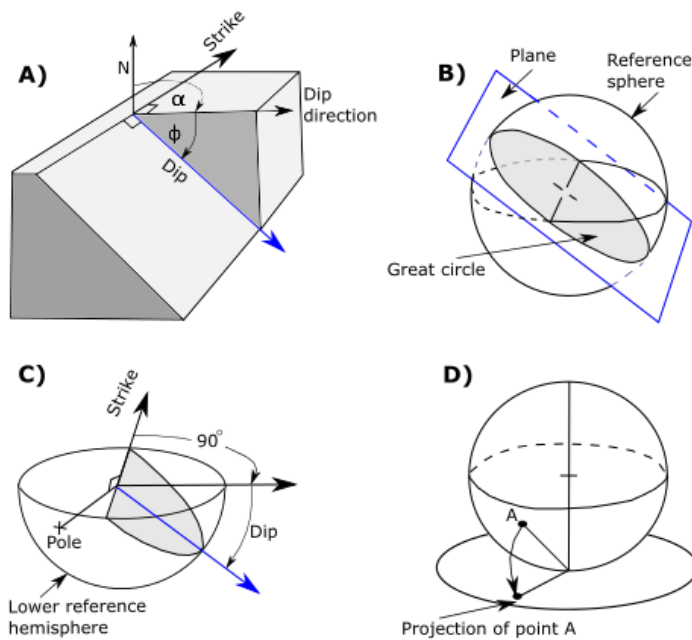
Figure 2.9: Principle of stereographic projection, modified after (Hoek and Bray, 1981a). (a) Isometric view of a plane with dip and dip direction.; (b) Great circle as a representation of the plane in the reference sphere.; (c) The pole is reflected onto the lower hemisphere, with a 90 °angle to the plane.; (d) The pole is projected onto the 2D-stereonet, with a unique position that contains information on both the dip, and dip direction.

2.3.2 Kinematic Feasibility Test

Kinematic feasibility testing is a relatively simple test, described in Hermanns et al. (2012b), Wyllie and Mah (2004), Richards et al. (1978) and Hoek and Bray (1981a) among others. The kinematic feasibility test assesses the failure mechanisms possible, depending on the existing discontinuities and their orientation in respect to the slope face (Hermanns et al., 2012b). Such discontinuities include joints, fractures, faults, foliation and can effect the stability of the slope (Oppikofer, 2009). Which structural patterns that allow for structurally controlled failures are presented in figure 2.10. It is important to be able to distinguish between the different slope failure modes, as there is a different stability analysis for each of them (Wyllie and Mah, 2004). The analysis will also show which direction the investigated block will slide and hence give an indication of the stability (Wyllie and Mah, 2004). The criterion for the kinematic feasibility test for the various failure mechanisms are presented in the following list.

- **Planar failure**

  For plane failures, the slope must contain a sliding plane with a dip that daylights the slope. Hence, the discontinuity needs to dip in the same direction as the topography. The tolerance angle of the dip of the discontinuity is smaller than the slope angle (in order to daylight) and steeper than the friction angle along the discontinuity (Wyllie and Mah, 2004; Hermanns et al., 2012b). In a stereonet, this signifies that the pole concentration must fall inside the daylight envelope, and simultaneously lie outside the friction cone, which represents the friction angle (Wyllie and Mah, 2004; Hermanns et al., 2012b). The friction angle is set based on the conditions of the rock mass in the area. Otherwise a friction angle of 20°is seen as a rather conservative value (Wyllie and Mah, 2004).

  The lateral tolerance between the discontinuity and the slope aspect is often set to +/- 20°(Hoek and Bray, 1981a; Wyllie and Mah, 2004). However, in studies with large rock volumes, this limitation can be considered to small and not suitable (Hermanns et al., 2012b). Hermanns et al. (2012b) describes this lateral tolerance as possible if the difference between the sliding plane (or intersection line) is smaller than 30°and partly possible if the difference is larger than 30°. To be more conservative, this restriction can be ignored. For large slope instabilities where the slope involves complex structures, this limitation is considered not suitable (Oppikofer, 2009; Böhme et al., 2013).

- **Wedge failure**

  The kinematic analysis of a wedge failure is somewhat similar to the one for a planar failure, as the same criteria apply for sliding mechanisms where the sliding plane is formed by the intersection of two discontinuities (Markland, 1973; Hoek and Bray, 1981a; Wyllie and Mah, 2004; Hermanns et al., 2012b). The difference is, that in wedge failures, the line of intersection of the two discontinuities is used, rather than the poles (Wyllie and Mah, 2004). The intersection line between the two discontinuities must daylight the slope and at the same time be steeper than the friction angle (Hermanns et al., 2012b). Generally, the same limitations for the lateral tolerance are applied also for wedge failure, unless the conditions suggest that the limitations are not suitable.

- **Toppling failure**

  Structures required for toppling failure are discontinuities dipping into the slope face with an angle within 10°on the slope face, so that the "slabs" or blocks are formed parallel to the slope (Wyllie and Mah, 2004). Toppling of rock occurs only in minor rock volumes, but flexural toppling can effect larger rock slopes (Hermanns et al., 2012b). However for flexural toppling to occur a large amount of internal pre-failure deformation is required (El Bedoui et al., 2009; Hermanns et al., 2012b).
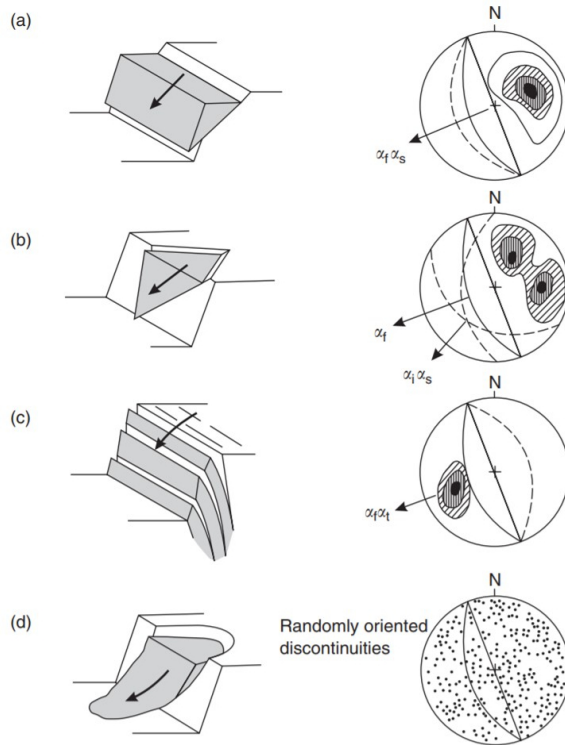
Figure 2.10: Four types of failure and the corresponding stereoplots: (a) Plane failure in rock. The parallel sliding plane is dipping out of the slope, but is less steep than the slope.; (b) Two discontinuities were the intersection line is dipping out of the slope and daylights.; (c) Toppling failure where the discontinuities are dipping towards the slope in a steep angle.; (d) Randomly oriented discontinuities and no pole concentration on the stereonet, resulting in a circular failure in the rock mass. Figure modified from (Wyllie and Mah, 2004).

2.3.3 Coltop 3D

Coltop 3D is a software designed for structural geological analysis of 3D point clouds. The software can be used in combination with a high resolution DEM to create a shaded relief in order to investigate the orientation of structural features. Each of the orientations is given a unique color. This colour is defined by the dip and dip direction of each cell which is again defined by the pole of the plane (Jaboyedoff et al., 2009). The orientation of the surface is defined by four nearest neighbor points in a squere, corresponding to a line passing through the middle of the cell linking these 4 grid points (Jaboyedoff et al., 2007) (Figure 2.11).

Coltop 3D represents the point clouds topograpy with a color for each specific orientation which is assigned dependent on the azimuth and slope gradient of the features (Jaboyedoff et al., 2007; Penna et al., 2016). Measurements of the structures can be collected and exported to excel, as this will include measurements from areas not reachable in the field. In this study, a detailed structural investigation was conducted by use of the software, Coltop 3D. For a more throughout explanation of the principles of the software Coltop 3D the article from Jaboyedoff et al. (2007) is recommended.
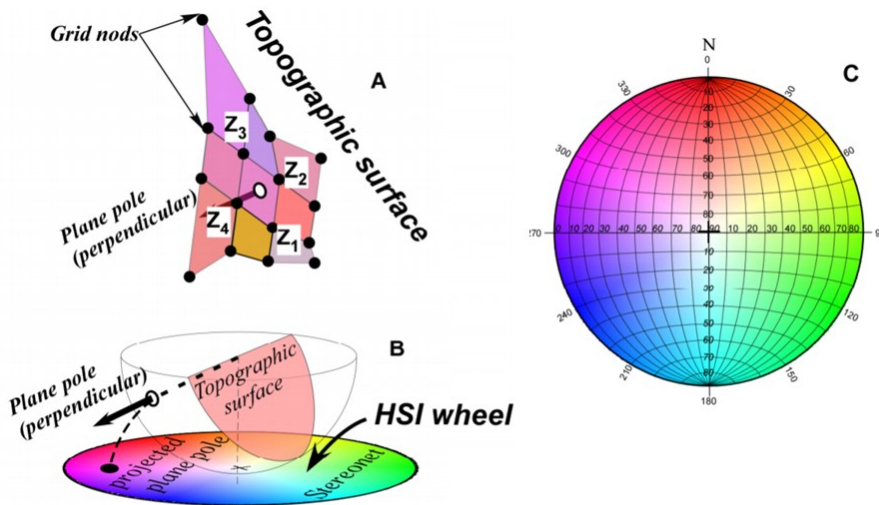
Figure 2.11: Basic principles of Coltop 3D. (a) Each of the structure orientations are defined by a unique color, representing the dip and dip direction.; (b) Example of the color coding, which fills the stereo-net following the Intensity-Hue-Saturation system. The topographic surface is colored based on the pole location in the colored stereo net.; (c) The Intensity-Hue-Saturation color system in a equal area stereonet. Figure modified from Jaboyedoff et al. (2007).

Chapter 3

Methods

3.1 Fieldwork

The fieldwork for this thesis was carried out one week in September 2017, and included LiDAR scanning of the slope, photos taken with drone and a Single Lens Reflex camera from helicopter, in addition to traditional structural mapping. LiDAR scanning was done from four different locations to capture structures from all possible viewpoints of Preikestolen. All sites were also captured during the photogrammetry models, with more than 1500 pictures from the drone and two SLR models. Further data preparations of the remote sensing techniques will be explained in chapter 3.2 and 3.3.

The structural mapping included measuring of joint sets and foliation, where dip and dip direction were recorded. During the fieldwork, more than 500 structural measurements were recorded with a Freiberg geological compass. The positions where the measurements were taken, was recorded with a hand held GPS (Garmin eTrex 20), which has an error of a few meters (in open terrain approximately 3-6 m). The measurements were spread over the area around Preikestolen. In total, 13 locations were used to gather structural measurements, and approximately 40 measurements were recorded from each location. Later, the structures measured in the field will be combined with structures gathered with the 3D models (through Coltop 3D), and used in a kinematic feasibility test.

The rock types in the area were observed during the week and compared to the existing bedrock map from NGU (scale 1:50 000) during the fieldwork, which shows a combination of two different lithologies. Four rock samples from the two different lithologies were collected. The purpose of gathering these blocks was to get a better understanding of the mechanical properties by laboratory investigations. The blocks were brought to the rock mechanics lab at the Norwegian University of Science and Technology for preparation and testing (uniaxial compressive test and tilt test), further described in chapter 3.4.

3.2 Remote Sensing

Remote sensing is a general term used for techniques that gather information about an object from a distance, and without physical contact (Longley et al., 2015). Two types of sensors are used in remote sensing techniques; active and passive sensors. Passive sensors use the radiation from the sun that is emitted from the observed object. This applies for techniques such as aerial photographs. Active sensors, which is used in for example laser scanning, generate its own source of electromagnetic radiation. Remote sensing techniques can be used from ground based sensors, aerial sensors and satellite sensors.

3.2.1 Light Detection and Ranging (LiDAR)

LiDAR is a relatively new active remote sensing instrument. The scanner transmits a laser pulse and measures the radiation that is scattered back to the receiver from the scanned object (Jaboyedoff et al., 2012). The wavelengths of the electromagnetic radiation that is transmitted is often near infrared (Hodgetts, 2013). LiDAR scanners can be airborne-based (ALS) or ground-based (TLS) (Figure 3.1). While the airborne scanner can cover a large area in a shorter time, the terrestrial laser scanner is often more accurate. The reason for this is that the TLS has a better point accuracy due to its fixed position (Oppikofer, 2009). The data is collected as a point cloud, which is a collection of 3D coordinates of single points (x, y and z).

Due to laser scanner technology, gathering large amounts of 3D data in a short time with an excellent accuracy, is possible (Shan and Toth, 2008). After initial data capture, extensive processing is usually required to remove tree canopies, buildings and other un-wanted features and to correct errors in order to provide a "bare earth" point data-set.

The points in a LiDAR data-set are often rasterized to create a DEM that can be used in a Geographic Information (GI) software. The creation of a DEM is an important part of the data that can be gathered with the laser scanner, but it also has other important implications in the landslide field. The high resolution data from both TLS and ALS can be used to gather structural data from rock slopes, hence it could be included in a structural analysis (Oppikofer et al., 2012). To gather structural data, the point cloud or the DEM can be imported to a software like Coltop 3D, which can then be used to measure the plains and to gather data from the structures (Jaboyedoff et al., 2007; Oppikofer et al., 2012; Jaboyedoff et al., 2012).
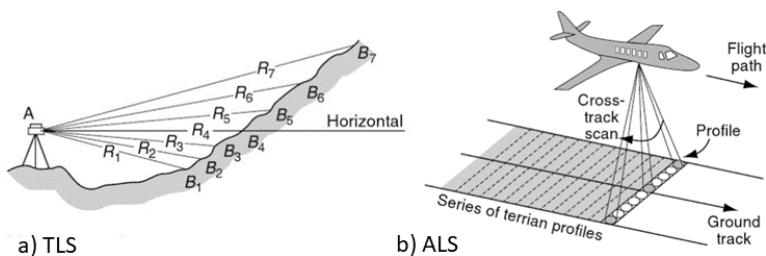
Figure 3.1: Terrestrial Laser Scanning (TLS) and Aerial Laser Scanning (ALS) follow the same basic prinsiples. Figure modified from (Shan and Toth, 2008).

3.2.2 LiDAR in the Field

The LiDAR scans were taken from four positions. One from the opposite side of the fjord, one from above the plateau, and one from each side of Preikestolen (Figure 3.2). For a structural analysis based on LiDAR measurements, several scans can minimize the risk of having occlusions and orientation biases in the data sets (Sturzenegger et al., 2007; Sturzenegger and Stead, 2009; Oppikofer, 2009). The LiDAR scanner used by NGU is the Optech ILRIS-3D LR (Figure 3.3) which uses infrared light and has a theoretical range of 3000 m with a reflectively of 80% (Optech, 2018).

However, when the LiDAR scanner is used for structural mapping, a large scan-distance is generally not recommended for mapping of structures. In the study from Sturzenegger et al. (2007), a practical limit of 800 m for scanning rock slopes was found, with a scanner with 1500 m maximum range. It is important that the scanning distance is not too large, as the spacing between the points potentially can exceed important structures.

The mean distance from the scanner to the scanned area in this project varied from 40 m to approximately 2000 m (Table 3.1). It was however decided that the scan from 2000 m distance was acceptable, to use as a background scan to reference the more detailed ones.

Table 3.1: The six scans were taken over two days during the fieldwork. Three positions (scan 1,2 and 4) required more than one scanning window to capture the whole surface of interest.

Scan	Points	Mean distance	Beam width	Spacing
1	8.0 million	1979 m	348.4 mm	197 mm
1 (2)	7.0 million	1819 m	321.2 mm	182 mm
2	8.6 million	115 m	31.6 mm	25.3 mm
2 (2)	6.0 million	105 m	29.9 mm	23.1 mm
3	7.0 million	40 m	11 mm	16 mm
4	7.9 million	203 m	46.5 mm	28.4 mm
4 (2)	7.8 million	186 m	43.5 mm	29.8 mm

Several steps were needed to process the raw data from the LiDAR scanner, to a finished georeferenced point cloud (Figure 3.4). The files were then exported to Pifedit which is a part of the Polyworks-V12 software. Pifedit was used to delete excessive points, like vegetation and out-lier points, in addition to the not so insignificant number of tourists. This was done to get a better match between the scans. Further the point cloud was exported to Imalign (Polyworks), to align the scans from different positions.

The alignment consisted of two step. Firstly the clouds were aligned using recognizable common features, followed by an optimization of the alignment with the Interactive Closest Points (ICP) (Chen and Medioni, 1991; Besl and McKay, 1992; Jaboyedoff et al., 2012). The finished point cloud was eventually georeferenced to the drone model, which is described in chapter 3.2.3. In other cases, georeferencing to an existing DEM is usual. However, at Preikestolen, no better DEM than the national 10 m DEM was available, making the georeferencing challenging.
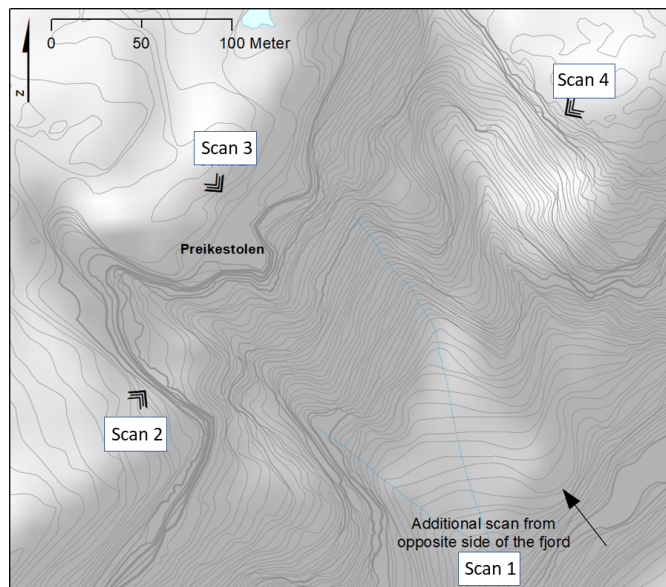
Figure 3.2: The Optech ILRIS-3D LR was used to scan Preikestolen from four different positions to capture the structures visible from all angles. The distance from the scanner to Preikestolen varied from 40 m (photo) to 2000 m at the opposite side of the fjord.

Figure 3.3: The Optech ILRIS-3D LR during the closes scan (scan 3) with a mean distance of 40 m.
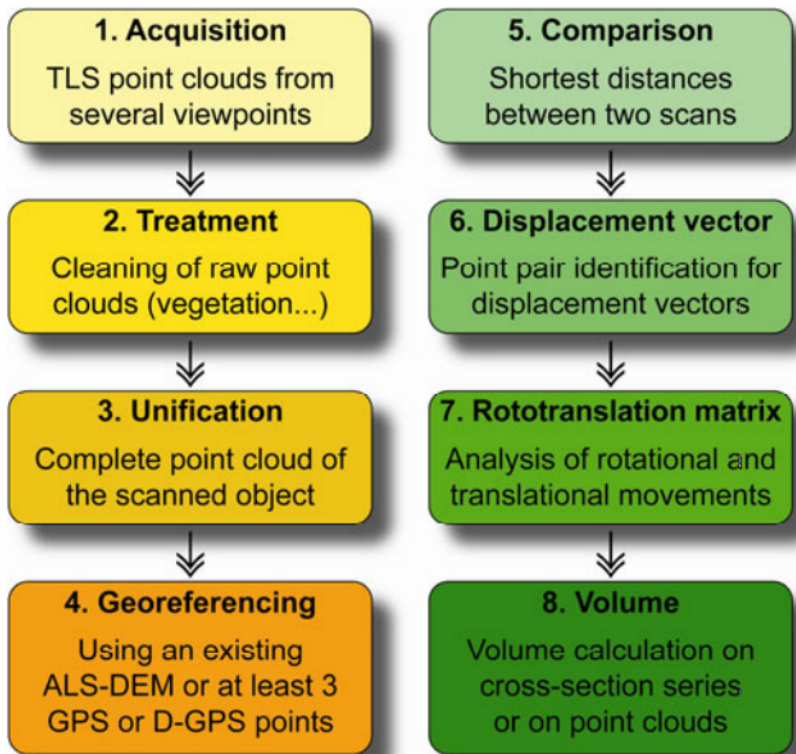
Figure 3.4: The general work flow for processing of laser data. The left column is for single scans, while the right one concern several scans and can be used for monitoring purposes. In this project, the laser data will not be used to measure displacements, as only one series was scanned. The volume will be calculated based on the interpretations of structures in the rock mass. Figure from (Oppikofer, 2009).

3.2.3 Photogrammetry

Photogrammetry has existed for many years in geoscience, but in the earlier years this was often with stereo aerial photographs (Birdseye, 1940; Eardley et al., 1942; Bemis et al., 2014). The basics of photogrammetry are the reconstruction of objects from pictures. This is done through overlapping of photos taken from different angles and positions. In general the photos can be taken by a normal digital camera, but the quality of the final model, will however be dependent on the quality of the input photos. This makes the method relatively cheap, compared to other 3D modelling techniques like LiDAR.

A relatively new method called Structure from Motion (SfM) was originally developed for three dimensional surveys of buildings (Fonstad et al., 2013). This method is purely image based and in the area of automated image matching. The method uses complex algorithms which finds matching image points, and uses this to match the images. This means that unlike traditional photogrammetry, there is no need for ground control points. Software used to perform SfM analysis is also freely available. For more detailed information and descriptions about the complex algorithms used in SfM techniques, the articles from Snavely et al. (2006, 2008) and Snavely (2009) are recommended.

It is however important that the overlap between the images is sufficient. While stereoscopic images often require an overlap of 50-60 % (Kraus and Waldhäusl, 1993; Abdullah et al., 2013), the automated SfM reconstruction is more dependent of angular change between the images (Bemis et al., 2014). According to Moreels and Perona (2007), viewpoint changes exceeding 25-30 ° is unfortunate. This is supported by Bemis et al. (2014) which claims that the maximum angle in overlapping images should not be more than 10-20°. In addition to the angular change, it is important that the reconstructed surface is covered by a minimum of two pictures from different positions (Figure 3.5) .

Some software use an arbitrary coordinate system, and need reference points to be adjusted to real word coordinates (Bemis et al., 2014). Photographs taken with special cameras make the processing simple due to complex mathematical algorithms and modern software (Kraus, 2007). The result can be exported as a point cloud with points containing 3D information. This is because of the possibility to calculate unique three dimensional location of points shared, relative to the cameras position.

portion of surface resolvable by photo-based reconstructions
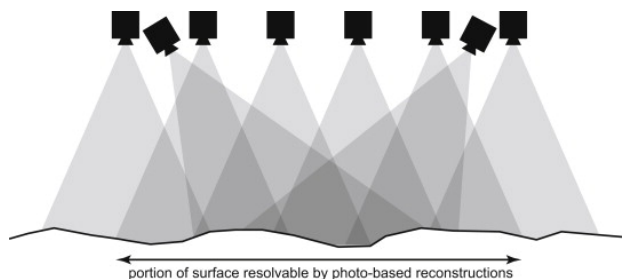
Figure 3.5: Basics of photogrammetry work flow is overlapping images taken from different positions and angles. Figure from Bemis et al. (2014).

3.2.4 Photogrammetry at Preikestolen

At Preikestolen, three 3D-models were made by using photogrammetry. Two models were made from a Single-Lence Reflex camera (SLR), and the last model from a DJI Phantom 4 drone.

The use of photogrammetry is expected to be well suited for the situation at Preikestolen, as the vegetation in the area is sparse. However, according to Nicolet (2017), when using the SfM techniques even sparse vegetation can cause problems.

The light conditions were also expected to cause problems at Preikestolen, as the flight time was limited to the gap between 5 p.m. and 9 a.m. The light condition is presented by Nicolet (2017), as a potential drawback when using the SfM method, as the intensity is not uni-vocal and will be dependent on the light conditions.

Helicopter

The reason for creating two models from helicopter, was due to the light conditions. Due to the strict limitations for flying helicopter in the area, photographing during the most optimal light conditions was not possible. It was therefore decided to create one model with photographs from early in the morning, and one based on photos from the evening.

The Nikon D 800, a SLR camera with a resolution of about 40 megapixels, was used for the photogrammetry models from the helicopter. These photos have a higher quality than the photos taken from the drone, but do not capture as many details as the drone, as it can't come as close up to the slope. For the first model, a total of 403 photos were taken. For the second model, 418 photos were taken. The photos from the field were imported to Agisoft Photoscan at NGU. The finished point clouds were imported to CloudCompare, for the georeferencing.

Drone

As the unmanned aerial vehicles (UAV's/drones) are improving, this type of mapping has become of huge interest among researches and in the industries (Shahbazi et al., 2015). Drones are also a rather inexpensive method for creating 3D models, and this was one of the reasons for comparing it to the more expensive photogrammetry from helicopter. However, the photo quality from the drone are not as high quality as the ones from a good SLR camera.

Prior to the fieldwork the fly route was defined and the drone followed coordinates when taking photos. The drone that was used was a regular DJI Phantom 4. A total of 317 photos were taken. Since the coordinates of the pictures were known, the finished 3D model was georeferenced after the processing. Hence, less processing was required for this model.

3.3 Rock properties and classification

3.3.1 Lab

To get a better understanding of the rock properties and to make a realistic numerical model, the strength and elasticity of the rocks have to be tested. Useful information can be obtained through lab tests such as the Uniaxial Compressive Test (UCS) and tilt test. Through these tests the Uniaxial Compressive Strength (σ_c), Youngs-modulus and basic friction angle can be determined. The samples collected in the field consisted of four blocks. One large block of granitic gneiss (sample 1), and three smaller blocks of porphyritic granite (sample 2). For each of the lithologies five cores were drilled out for the uniaxial compression test, while three samples were planned for the tilt test. An overview of the total number of samples can be seen in table 3.2.

All the samples were drilled out following the same work flow. First the core diameter was picked based on the optimal diameter. For the tilt test samples the diameter of the bore head was 32 mm, while for the UCS planned cores, a diameter of 54 mm and 40 mm were used. The drilling of the cores was carried out in the rock mechanic lab at NTNU with help from SINTEF. The samples had a different behavior when the cores were drilled out, as the granitic gneiss were much harder than the porphyritic granite to cut. After the cores were drilled out, the ends were generally covered with weathered rock. The weathered ends were cut off to obtain an optimal length, and to get rid of the weathered parts.

Table 3.2: Overview of the cores that were drilled out from the samples from Preikestolen. The porphyritic granite (sample 2) block was to small to drill out 54 mm diameters for testing the σ_c, therefore it was decided to use a 40 mm corer for sample 2.

Sample	Test	Length	Diameter	Weight	Comment
1-1	UCS	138.90 mm	54.20 mm	950.37 g	No visible weaknesses
1-2	UCS	138.91 mm	54.20 mm	947.30 g	Small and weathered joint
1-3	UCS	139.68 mm	54.20 mm	961.46 g	Small vertical joint
1-4	UCS	139.70 mm	54.21 mm	953.64 g	Weathered joint
1-5	UCS	139.82 mm	54.20 mm	958.08 g	No visible weaknesses
1-6	Tilt	89.0 mm	32.2 mm	-	No visible weaknesses
1-7	Tilt	87.5 mm	32.5 mm	-	No visible weaknesses
1-8	Tilt	87.3 mm	32.4 mm	-	No visible weaknesses
2-1	UCS	102.03 mm	40.02 mm	339.71 g	No visible weaknesses
2-2	UCS	101.77 mm	40.03 mm	335.67 g	No visible weaknesses
2-3	UCS	99.85 mm	40.04 mm	333.75 g	No visible weaknesses
2-4	UCS	101.77 mm	40.05 mm	340.30 g	No visible weaknesses
2-5	UCS	101.81 mm	40.05 mm	339.15 g	No visible weaknesses
2-6	Tilt	80.1 mm	33.3 mm	-	No visible weaknesses
2-7	Tilt	83.2 mm	33 mm	-	No visible weaknesses
2-8	Tilt	80.0 mm	32.1 mm	-	No visible weaknesses

3.3.2 Uniaxial Compressive Test

In general, five rock specimens are required to determine the σ_c of a rock type through an uni-axial compressive test. The test is carried out through applying the stress on the top surface of the sample, without any confining pressure. In other words the only load that is applied is in the sigma 1 direction, while sigma 2 and sigma 3 is zero (Figure 3.6). The machine used for the compressive tests, was the GCTS RTR - 4000, at the rock mechanics lab at NTNU which has a 4000 ton loading capacity. Before testing, a plastic membrane is applied to the sample, to avoid the samples from falling apart after testing. Generally, the average result from five test samples is used. However samples with visible weakness zones, or samples behaving differently and abnormally, are often excluded from the test results.

The test requires a cylindrical sample with a diameter of approximately 54 mm and a length of a 2.5 - 3 times the diameter. The ratio between the length and diameter of the sample is especially important, and the sample ends should be totally smooth to get a good result.

The cores from the granitic gneiss (sample 1) were all drilled with a core diameter of 54 mm. The diameter of the porphyritic granite cores was reduced to 40 mm, due to lack of rock sample with proper quality. Preferably, the porphyritic granite should also have been 54 mm in diameter, especially due to the large clasts of feldspar present in the sample. The length/diameter ratio used was 2.5, which is standard for a uni-axial compression test. During the uniaxial compressive test, the radial strain rock mechanics are displayed as negative on the x axis, while the axial strain (compression) will be displayed as positive. The strain is measured by a radial extensometer surrounding the rock sample, and two axial extensometers (Figure 3.7).
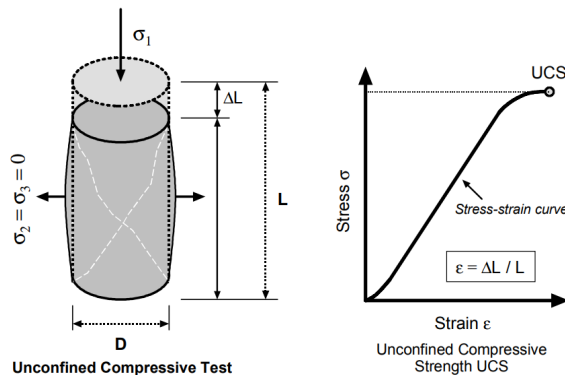
Figure 3.6: Basic principles of the uniaxial compressive test. As the samples are only tested in one direction, the σ_1 is applied, while $\sigma_2 = \sigma_3 = 0$. The axial deformation (compression), is plotted against the stress applied in a stress strain curve. Figure from Thuro et al. (2001).

In cases where the rock sample can withstand more than 200 MPa, the test is generally stopped, and the measuring equipment is removed. As the values like Young's modulus and Poissons ratio can be calculated from the $\sigma_{c(50\%)}$ value, no important information is

lost. The test was stopped prior to failure in four cases for sample 1. The porphyritic granite were however measured until failure occurred, due to a lower σ_c. During the test the loading rate changed from the original 0.8 MPa/s, depending on the strain rate, called strain control. This was to capture data from the post failure behaviour of the rock.

The UCS is the maximum stress applied prior to failure. Young's modulus (E) is defined as a rocks ability to withstand failure despite deformation. Poisson's ratio (ν) is the ratio of transverse strain to axial strain. Young's modulus and Poisson's ratio were calculated automatically by the computer during the test, based on the following formulas. These values give important information about the rocks behavior and are critical to reproduce a realistic numerical model of the rock type.

$$E = \frac{\Delta\sigma_{a,50\%}}{\Delta\epsilon_{a,50\%}} \tag{3.1}$$

$$v = \frac{\Delta\epsilon_{r,50\%}}{\Delta\epsilon_{a,50\%}} \tag{3.2}$$
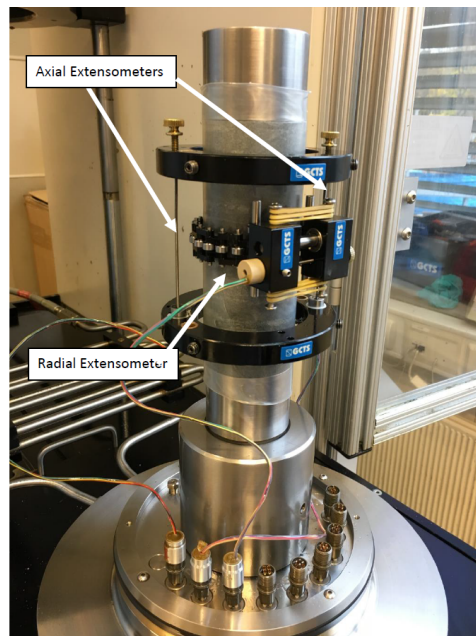
Figure 3.7: Setup prior to the uniaxial compressive test. The samples were covered with a thin plastic film, to avoid that the samples were falling apart after testing. This film does not effect the test result. During the test, extensometers register the axial compression (positive) and radial deformation (negative).

Influence of sample size

How the sample size influences the strength of the rock is widely discussed in the field of geotechniques (Hoek, 2007). The following equation was published by Hoek and Brown (1980b), to calculate the uniaxial compressive strength σ_{cd} for a core with diameter d. This was compared to a rock specimen of 50 mm diameter, and the uniaxial compressive strength σ_{c50}.

$$\sigma_{cd} = \sigma_{c50} \left(\frac{50}{d} \right)^{0.18} \tag{3.3}$$

According to this equation, the rock strength is decreasing with a higher sample diameter. As Hoek (2007) explains, this is due to a greater opportunity of failure trough and around the grains in the sample. When a significant number of grains are included in the sample, the shear strength will remain constant. However, several studies like Hawkins (1998) study of sedimentary rocks, it was shown that this equation did not apply for small diameters (less than 54), as it was in fact reversed (Figure 3.8) (Masoumi et al., 2012). The study from Thuro et al. (2001) however, found no scale effect in the testing samples with a diameter of 45 mm to 80 mm.
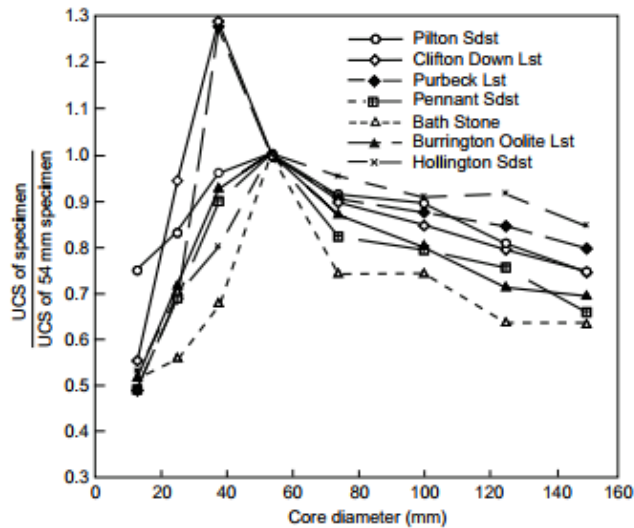
Figure 3.8: Unlike the theory from Hoek (2007), Hawkins (1998) experienced a different behavior when testing samples with various diameter in the uniaxial compressive test, as the smaller samples showed a decreased strength compared to the larger samples. Figure from Hawkins (1998).

3.4   Laboratory Measurements

3.4.1   Uniaxial Compressive Test

Five cores from each of the rock samples were tested in the uniaxial compressive test, as required in the standards from ISRM (1981). The results from the uniaxial compressive test (Table 3.3 and 3.4) show a different result for the two different rock samples. In general the porphyritic granite allowed for more deformation prior to failure, while the granitic gneiss did not allow for deformation.

Sample 1

The high Youngs-modulus of the granitic gneiss, made the failure rather brutal, with low deformation prior to the sudden and uncontrollable failure. Due to the high σ_c it was decided to run the test only to 200 MPa. The extensometers were then removed (to avoid that the brutal failure would destroy them) and the test was started again and then run until failure. However, quite unexpected, core 2 failed brutally at 198.6 MPa, destroying one of the extensometers. After this, it was decided only to run the test until 150 MPa before removing the extensometers, since the rock samples were so uncontrollable. All important parameters would still be calculated, as they are calculated from the $\sigma_{c50\%}$ value and $\varepsilon_{c50\%}$ which is the stress and strain at 50% of the peak strength (σ_c).

Of the five rock specimens that were tested in the uniaxial compressive test, three of them are evaluated as reliable results. This is due to weathered zones in the rock specimen number 2 and 4. In these tests, the failure occurred along a clearly visible joint, with visible weathering along the failure surface. Core nr. 5 also contained a weaker plane, however since the behavior otherwise was very similar to the intact cores, it was decided to include it as a valid test result. The σ_c of core 5 is however interpreted to be slightly underestimated, as the core did fail along the weak plane. The results are presented in table 3.3. For an overview of the graphs from the UCS, see figure 3.10.

After the brutal failure, the cores were removed from the plastic membrane. The results from the samples were variable from sample to sample. Those cores that contained a weakness plane, had all of them failed along the weak plane. The cores without weakness planes were split into several smaller pieces (Figure 3.9a), and no failure angle could be determined. The average uniaxial compressive strength for the valid cores is set to 227 MPa.

Table 3.3: Core 2 and 4 showed an abnormal behavior while testing, in addition to UCS values that were significantly lower than for the other cores.

Core	σ_c(MPa)	E(GPa)	ν	Fracture angle (°)	γ (kN/m^3)
1	270	85.11	0.26	not determined	29.7
2	~~198.6~~	~~74.63~~	~~0.75~~	~~not determined~~	29.6
3	219	88.41	0.28	not determined	29.8
4	~~153~~	~~76.46~~	~~0.57~~	~~not determined~~	29.6
5	193	91.34	0.26	not determined	29.7

Sample 2

Sample 2 was more uniform than sample 1 in the way it reacted in the UCS test. There were no visible weaknesses in any of the cores, and they all behaved in a relatively similar manner. However, as can be seen from the overview of all the test graphs in figure 3.11, core nr 4 had an abnormal behaviour during testing. Therefore, it will not be included in the further usage of the test results shown in table 3.4. All of the samples were tested until failure, with the extensometers on. The failure was more controllable than for the first rock type, and the results were more like the behavior expected for a granite where the rock is more slowly "crumbling" along the large grains during the failure. After the testing was done, the cores were also very different from the sample 1 cores. Sample 2 showed no clear rupture surface (Figure 3.9), but for some of the samples, the fracture angle could be determined. The average σ_c for the valid cores is 141 MPa.

Table 3.4: All the cores behaved in a relatively similar way. However, core 4 was evaluated as not reliable, and is therefore not included in the calculation of the average values.

Core	σ_c(MPa)	E(GPa)	ν	Fracture angle ($^\circ$)	γ (kN/m^3)
1	140.4	40.07	0.29	not determined	26.5
2	124.8	48.48	0.38	30	26.2
3	151.1	45.65	0.32	25	26.5
4	~~128.6~~	~~41.73~~	~~0.28~~	~~not determined~~	26.5
5	149.1	48.56	0.33	27	26.4

Figure 3.9: The behavior of sample 1 and sample 2 was different, both prior to and during failure. a) Sample 1 broke into several small pieces with no clear rupture angle.; b) Sample 2 behaved like a typical granite, and the fracture angle could be determined from some of the cores.
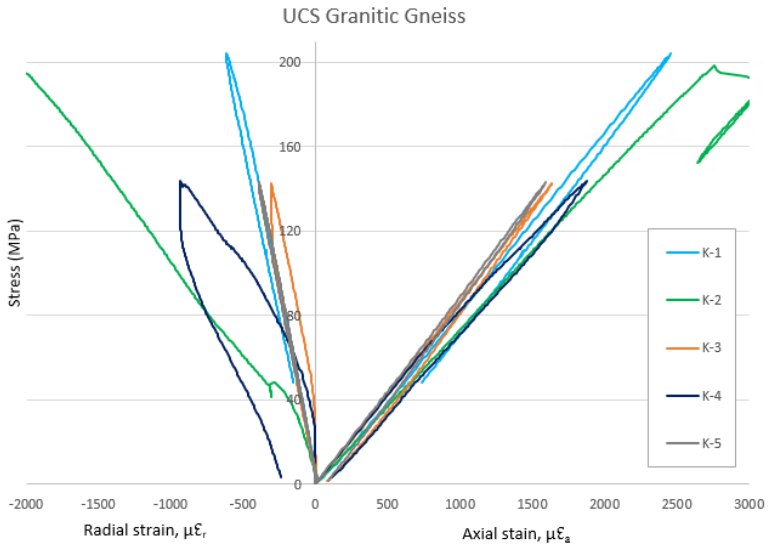
Figure 3.10: Overview of the results from the uniaxial compressive test for sample 1. The tests were originally stopped at 200 MPa, but due to the brutal failure during testing of K-2 (at approximately 200 MPa) it was decided to stop the test at 150 MPa to remove the extensometers.
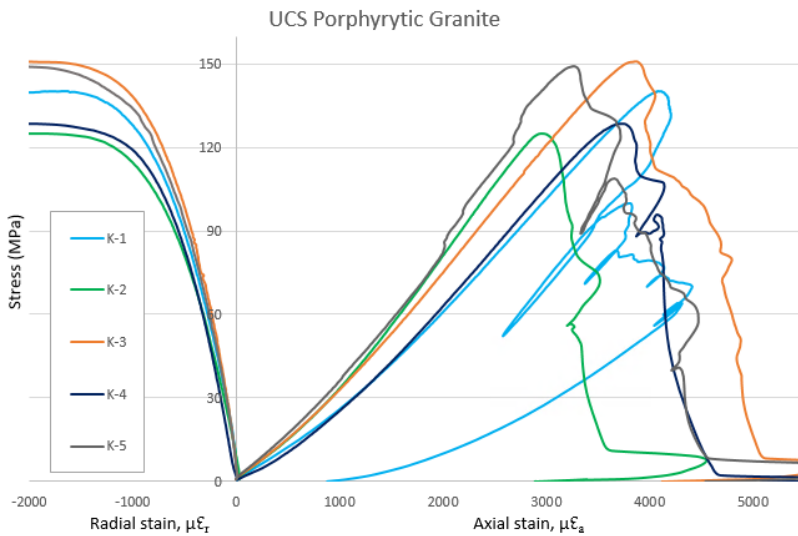
Figure 3.11: Overview of the results from the uniaxial compressive test for sample 2. All cores in sample 2 were run until failure with the extensometers attached.

3.4.2 Tilt Test

The tilt tests were done following the standards in Li et al. (2017), using three cores with a diameter of 32 mm and a length of 2.5 times the diameter to determine the basic friction angle. The test is carried out with two cores fastened to a tilt-table, with a third core resting upon the two others (Figure 3.12). The tilt table is then lifted up at a constant speed until sliding occurs. Before lifting the board, it should be ensured, that the top rock sample were free to move, and not fastened by any kind of discontinuities. A total of 15 measurements were taken with each rock type. For each fifth measurements, the position of the rock samples was changed. The standards from Li et al. (2017) recommends a total of 10 to 20 measurements for each sample to obtain a reliable result.

Three samples with a diameter of 32 mm were drilled out from both rock samples. The length varied from 80.0 mm to 89.0 mm. The porphyritic granite had some weathered zones, making it difficult to obtain the correct length on all the samples. The shorter samples did not fulfill the correct length/diameter ratio required in the test standards.

Figure 3.12: The basic principles of the three core tilt test following the standards from Li et al. (2017). The core was lifted at a constant speed until the upper core started sliding.

To adapt the results from the results to the standards in the saw cut test (described in Grøneng and Nilsen (2008)), some steps have to be taken. As the surface obtained by the core drilling is slightly rougher than the one measured from the saw-cut method , the basic friction angle measured with the three core method has to be decreased by $2°$(Li et al., 2017).

Results from the tilt test were carried out according to the standards in Li et al. (2017), and later converted to the basic friction angle obtained from a saw-cut tilt test. The conversion is carried out by adding two degrees to the result from the three core tilt test, as described in Li et al. (2017). The converted results from the tilt test are shown in figure 3.13 and figure 3.14. The general tendency shows a larger friction angle for the second sample which consisted of the porphyritic granite. This was also expected, as the number of large clasts in the porphyritic granite are interpreted to increase the friction angle of

the sample. The basic friction angle of sample 1 was generally about 3.7 degrees lower than the angle obtained from sample 2. The average basic friction angle was determined to 33.73° for sample 1, and 37.47° for sample 2.
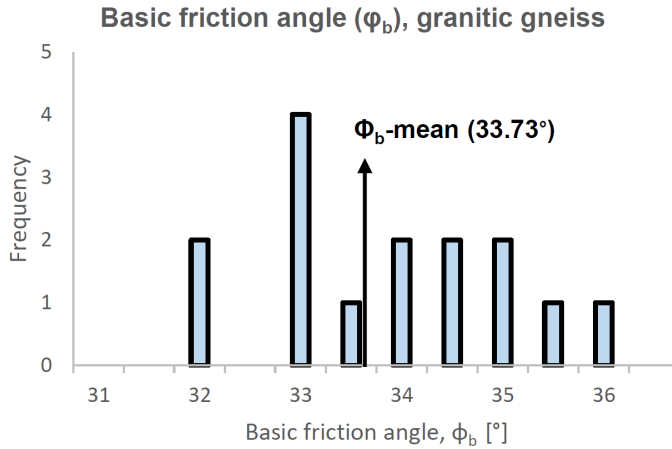
Figure 3.13: Histogram showing the basic friction angle, based on the values converted from the tilt test, to the standard basic friction value. The mean basic friction value was 33.73°.
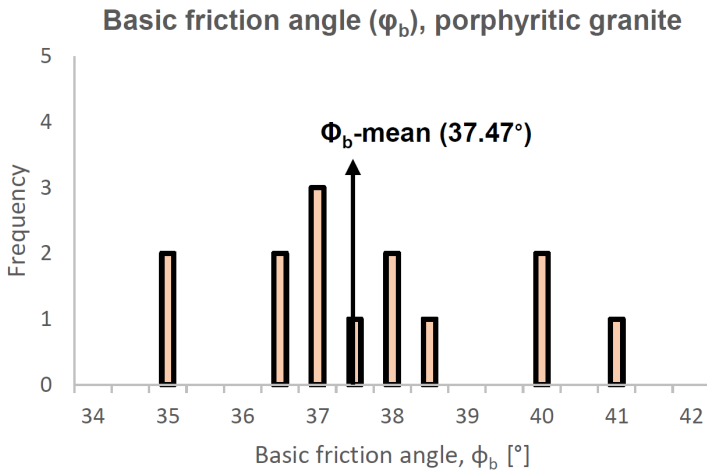
Figure 3.14: Histogram showing the basic friction angle, based on the values converted from the tilt test, to the standard basic friction value. The mean basic friction value was 37.47°.

3.5 Numerical Analysis

The use of numerical modelling in slope stability analysis is a relatively recent development (Grøneng, 2010). Basic kinematic methods are simple in their application, but will only suggest the potential for failure and do not provide slope stability condition in quantitative terms (Raghuvanshi, 2017; Alzoubi, 2016). In cases with complex rock slope deformation, the basic kinematic analysis is often considered too simple (Stead et al., 2006; Böhme et al., 2013). In such cases, the numerical modelling techniques can contribute to understanding the failure mechanisms of complex rock deformations (Böhme et al., 2013).

A number of different methods for numerical analysis exist (Figure 3.15). Which model that is used is generally based on the conditions at the study site, and what is appropriate for the analysis. One way to explain the principle of a numerical model, is to describe the material as divided into zones, whereas each zone is assigned a material mode and various properties. Discontinuous models (block models) are split by discontinuities, whereas in the continuous models the rock mass will be connected. A combination between the two different models is hybrid modelling. Discontinuous methods can also be explained as a method that treats the rock mass as a number of interacting blocks separated by discontinuities, and the individual blocks are therefore interacting along the boundaries. In general the discontinuous models are recommended for slope stability investigations where the stability seems governed primary by deformation along joints, or in cases concerning intact rock.

Continuum modelling treats the rock slope as a continuous mass build up by a number of elements that are connected. The two continuum methods that are used frequently in geotechnical engineering differentiate in the method of solution of the differential equations systems (Alzoubi, 2016). For example RS^2 uses a finite element code developed by Rocscience, and will be used as the numerical simulation tool at Preikestolen. The RS^2 software is freely available for NTNU students. An advantage in using a finite element model is also that the mesh generation is more flexible compared to the finite differentiate method (Alzoubi, 2016).
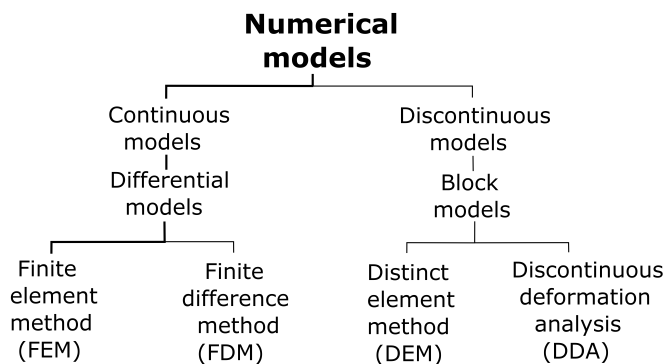
Figure 3.15: The various numerical models available. In this thesis the focus will be on Phase 2, which is a finite element, continuous model. Figure modified from (Grøneng, 2010).

3.5.1 Finite Element Method (FEM)

The basic principle of the finite element method is the division of the body into an assembly of smaller "elements" of various shapes (Grøneng, 2010). The elements are free to move or rotate, and can also be completely detached from the rock body at failure (Alzoubi, 2016). The displacements within the elements are related to the displacement at the nodes through so-called shape functions (Grøneng, 2010). The stresses are calculated at one or more points inside each of the elements (Grøneng, 2010). Transmission of internal forces between the edges of adjacent elements are represented by interactions at the nodes of the elements (Grøneng, 2010). The FEM is perhaps the most widely used method in numerical analysis. Hammah et al. (2007) mentions several advantages that has contributed to the popularity, such as the ability to model complex boundary and the possibility to include several materials in one model. For a throughout explanation of the finite element method, the article by Brady and Brown (2013) is recommended.

3.5.2 Shear Strength Reduction (SSR)

Shear Strength Reduction can be used to calculate the factor of safety in slope stability problems. The calculated factor of safety is the ratio of the actual shear strength of the rock to the minimum strength that will prevent failure (Wyllie and Mah, 2004). With a finite element program this is done by decreasing the strength of the material, until a Critical Strength Reduction Factor (CSRF) is reached, and a collapse will occur (Wyllie and Mah, 2004). The SSR factor method is explained by Hammah et al. (2007) for a slope material of Mohr-Coulomb strength as in equation 3.4 and 3.5.

$$\tau = c + \sigma_n tan\phi \tag{3.4}$$

where τ is the shear stress, σ_n the normal stress along the failure plane. c is the cohesion of the material, and the friction angle is represented by ϕ.

$$\frac{\tau}{F} = c^* + tan\phi^* \tag{3.5}$$

where F is the reduction factor, c* = c/F, where c is the Mohr-Coulomb cohesion. ϕ^* is ϕ/F which is the factored Mohr-Coulomb friction.

Even though the finite element shear strength reduction method is based on the principles from continuum modelling, the studies from Hammah et al. (2007) show that it is a good alternative to the distinct element modelling, also for blocky rock masses. The ability to include special elements, such as joints, in the continuum model has made it possible to represent the discontinuous behaviour of the joints between the blocks in the material (Hammah et al., 2007).

3.5.3 RS^2

RS^2 (previously Phase^2) stands for Rock and Soil 2-dimensional analysis program, and is a powerful 2D finite element program (Rocscience, 2018). The program was developed by Rocscience, and is widely used for different engineering purposes. RS^2 also offers a finite element (FEM) slope stability analysis. Some of the material models available in RS^2 are presented in figure 3.16.

The use of 2D numerical modelling in slope stability problems, have been done in several studies, like Böhme et al. (2013) where Phase^2, previous version of RS^2, was used to investigate the complex rock slope Stampa in Flåm. Another example is the study from Panthi and Nilsen (2006) where Phase^2 was used to model the Heggura slope in Tafjord. However, as described in Wyllie and Mah (2004), 2D models are not always appropriate. The following list was presented by Wyllie and Mah (2004) for situations where a three dimensional analysis are preferred.

- The strike of principal geological structures differences with more than 20-30 ° of the strike of the slope.

- The axis of foliation or other material anisitropy does not strike within 20-30 ° of the slope.

- The directions of the principal in-situ stresses are not parallel or perpendicular to the slope.

- The geo-mechanical units varies in distribution parallel to the strike of the slope.

- The slope geometry in plan cannot be represented by two-dimensional analysis, which assumes axis-symmetric or plain strain.

In the finite element slope stability analysis in RS^2 the method Shear Strength Reduction (SSR) is used either with the Mohr-Coulomb or Hoek-Brown strength parameters (Grøneng, 2010). In this project, a 2D model of the Preikestolen rock formation will be used to examine the stability of the rock slope by use of a finite element shear strength reduction analysis.

Constitutive models in RS²

Elastic models	Plastic models	Joint models
1) Isotropic	1) Drucker-Prager	1) Mohr-Coulomb
2) Orthotropic	2) Mohr-Coulomb	2) Barton-Bandis
3) Transversely Isotropic	3) Hoek-Brown	3) Geosynthetic Hyperbolic
4) Duncan-Chang Hyperbolic	4) Generalized Hoek-Brown	
	5) Cam-Clay	
	6) Modified Cam-Clay	
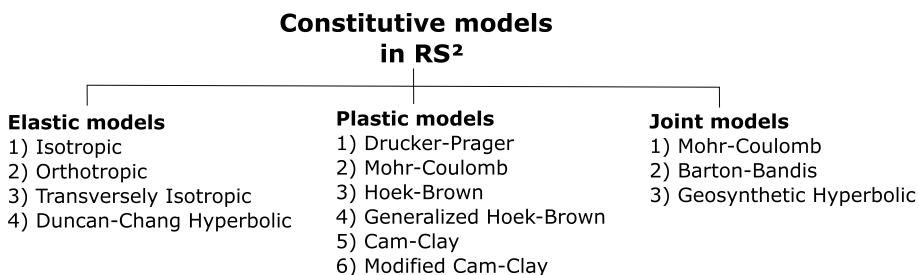
Figure 3.16: Some of the possible applications of the RS^2 program. Modified from Grøneng (2010).

3.5.4 Methodology for the RS^2 Models

The 2D profile used to create the RS^2 model was obtained by combining the drone model to the freely available 10 m DEM. A raster was created from the drone point cloud and combined with the 10 m DEM in ArcMap using the mosaic tool. This resulted in a combined digital elevation model which is detailed in the area around Preikestolen, and less detailed towards the edges. A profile was drawn through parts of Preikestolen, and this has been the basis for geometry of the RS^2 model (Figure 3.17). However, the profile had to be further adjusted in RS^2, and compared to profiles created in CloudCompare, as the steep area was poorly exported from the DEM.

Figure 3.17: Illustration of the position of the profile exported from ArcMap to RS^2. The profile was based on the high quality point cloud obtained from the drone model.

Boundary Conditions

The boundaries used in numerical modelling are either artificial or real (Wyllie and Mah, 2004). While the real boundaries exist, and represent the natural surfaces, the artificial boundaries do not exist in the real world. The artificial boundaries can be created to shrink the modelled area, only to include the area of interest. For the analysis to be meaningful, the model has to extend past the location of the instability (Chugh, 2003). Recommendations from Wyllie and Mah (2004) on slope stability modelling is shown in figure 3.18. Wyllie and Mah (2004) also highlights the general notion that the far-field boundaries position should not effect the result.

    The boundary conditions might effect the analysis in several ways. As fixed boundary conditions might cause underestimation of stress and/or displacement, a boundary with applied stress can have the opposite effect (Wyllie and Mah, 2004). The available boundary restraints in the RS^2 software is: Restrain X, Restrain Y, Restrain XY or Free. The Restrain X will allow for zero displacement in the X direction. The nodes are however free to move in the Y direction. For the restrain Y tool, the case is the opposite as for the Restrain X, as

Y will be zero, and X is free to move. However, in the XY boundary conditions, the nodes will not be free to move in either X or Y direction. The option is therefore used to apply pinned boundary conditions.

Free boundary conditions will allow the nodes to move in any directions. According to Rocscience (2018), this tool is useful when modelling surface excavations. Chugh (2003) mentions the restrain x (only allow for displacement in the y direction) as the most widely used for 2D model boundary conditions. The restrictions used in this case, are presented in table 3.5.

Table 3.5: Overview of the boundary conditions used in the RS^2 model of Preikestolen.

Boundary	Boundary type	Boundary condition	Description	Reference
Surface	Real	Free	Free to move in all directions	Rocscience (2018)
Sides	Artificial	Restrain X	locked in one direction	Chugh (2003)
Lower	Artificial	Restrain Y	locked in one direction	Sandøy (2012)
Corners (lower)	Artificial	Restrain X,Y	locked in all directions	Chugh (2003)
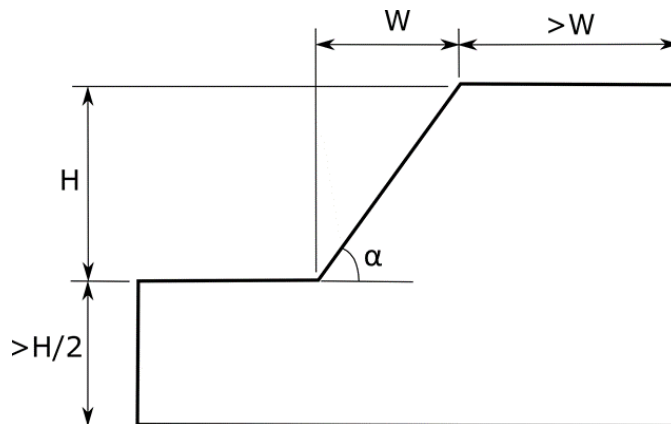
Figure 3.18: Recommended dimension of the far-field boundary setup within a slope stability problem. Figure modified from Wyllie and Mah (2004).

Mesh

After defining the external boundaries, the mesh was created using the discretization and meshing function. The discretize process subdivides the boundary line segments into discretizations. This will form a framework of the finite elements mesh. Further, the finite element mesh is generated based on the earlier discretization. The six-noded triangle mesh was used with the default number of nodes. According to the study by Hammah et al. (2005), the number of elements had very little effect on the calculated factor of safety. However, elements with poor quality should be avoided. The following mesh was used in the modelling:

- Mesh Type = Graded

- Element Type = 6 Noded Triangles

- Gradation Factor = 0.1

- Default Number of Nodes on External = 90

The density of the mesh was increased in the area around the potential sliding surface (advanced mesh), as it will produce a better model concerning the area of interest without significantly increasing the computation time.

Material settings

The program RS^2 can be run both in elastic or plastic analysis. The peak strength parameter describes failure in elastic rock mass, and residual values within plastic. In some rock masses, the shear stress will fall to a residual value that will stay constant (Hoek, 2007). This is the case for plastic rock, where the shear stress will reach a residual value after the peak value is obtained (Figure 3.19). The residual value will then stay constant as the displacement continues (Wyllie and Mah, 2004).

For the Preikestolen model, the plastic strain softening model is used. The strain softening analysis is carried out with residual values being 2/3 of the peak value. This applies for both the cohesion and the friction angle (Figure 3.20). Such strain softening models are considered very useful as they can simulate the strength loss that can occur after the peak strength is reached (Sjöberg, 1999).

Failure criterion

Several failure criterion can be used to model slope stability problems in RS^2. The most used failure criterion in rock mass modelling is the Mohr-Coulomb Hoek (2007), described in chapter 3.5.4. Otherwise, the Hoek-Brown criterion (Chapter 3.5.7) is also frequently used, as it is better suited in stability analyses of rock masses when compared to the Mohr-Coulomb (Hammah et al., 2004). The Hoek-Brown criteria treats the rock mass as an isotropic rock mass. However, if one of the discontinuity sets is significantly weaker than the other, or if few discontinuities dominate the rock mass, the Hoek-Brown criterion is not suitable (Hoek, 2007). The numerical simulation at Preikestolen included two simulations with the Mohr-Coulomb criterion, and one with the Hoek-Brown criterion.
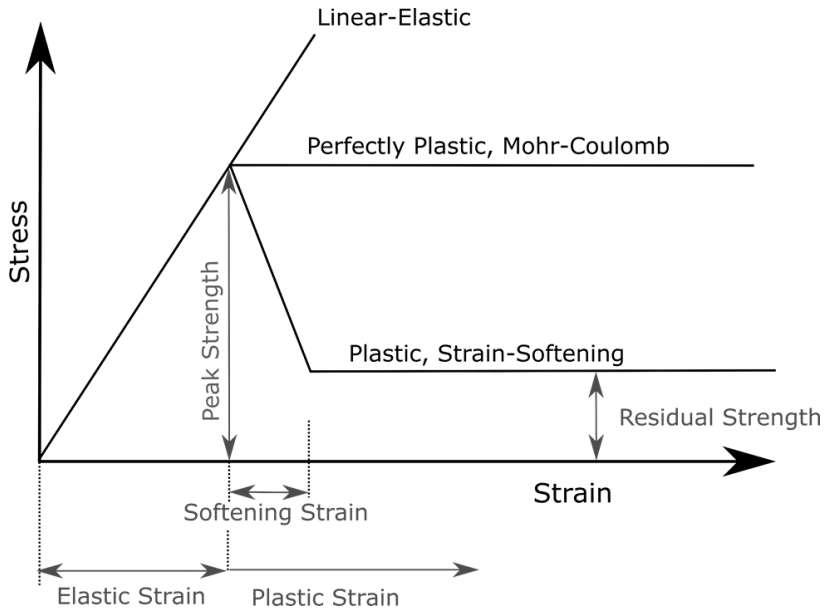
Figure 3.19: Stress-strain relationships in plastic, elastic rocks. The plastic and elastic rock behave differently when stress is applied, where the residual strength represents the plastic strain-softening model. Figure modified from Sjöberg (1999).
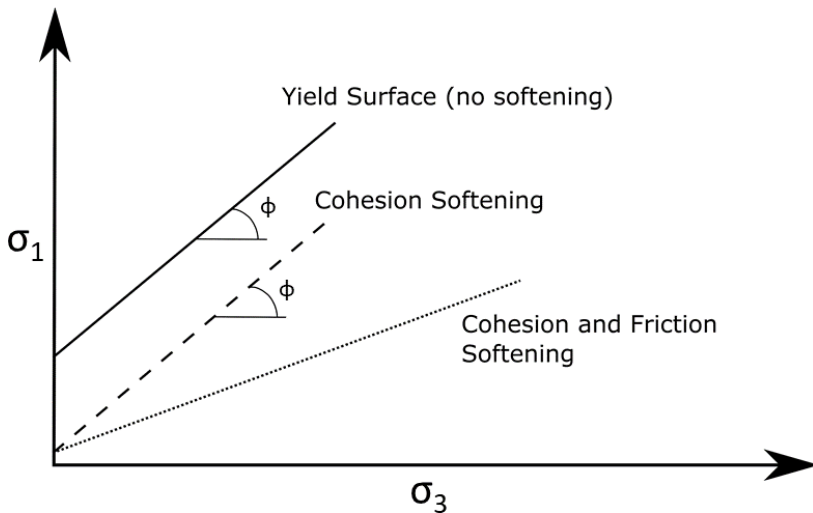
Figure 3.20: Strain softening of parameters. At Preikestolen, both the residual cohesion and friction angle of the rock mass are reduced to 2/3 of the peak value. Figure modified from Sjöberg (1999).

3.5.5 Rock Mass Input Parameters

The rock mass properties of the granitic gneiss (GG) and the porphyritic granite (PG) is given in table 3.6. These values were either found during testing in the laboratory or from field-estimations. How these values were obtained is explained in detail in chapter 3.5.

Table 3.6: The values calculated from the lab tests are used as input parameters for the rock mass.

Description	Symbol	Unit	GG	PG
Basic friction angle	ϕ_b	°	33.73	37.47
Uniaxial compressive strength	σ_{ci}	MPa	227	141
E-modulus (intact)	E_i	MPa	88.3	45.7
GSI	-	-	80	90
Unit weight	γ	kN/m^3	29.7	26.4

Coversion from Hoek-Brown to Mohr-Coulomb Criterion using RocData 5.0

Since the two joint sets J3 and J2 are interpreted to be important for the stability, the Mohr-Coulomb criterion is preferred at Preikestolen. Therefore, the parameters from the field and laboratory work had to be converted from Generalized Hoek-Brown parameters to Mohr-Coulomb parameters.

This conversion can be done using the software RocData 5.0, where the equivalent cohesion and friction angle are determined. These values are then included in the SSR analysis. However, there are some problems, concerning the determination of the friction angle and the cohesion (Sandøy, 2012). This is manly due to the active friction angle, which is included as a constant, but is in fact highly variable and dependent on the normal stress level (Nilsen, 2000).

The relationship between shear strength and and normal stress is not linear. Therefore, as explained by Nilsen et al. (2011) it is important to calculate the normal stress prior to the determination of the cohesion and friction angle. However, this is taken into consideration with the tool Instantaneous Mohr-Coulomb tool available in RocData, as the peak strength is estimated based on the normal stress in the situation. The calculation of the mean normal stress (σ_n) is calculated from the unit weight of the rock mass (γ) and overburden to basal surface (z) shown in equation 3.6.

$$\sigma_n = \gamma * z \tag{3.6}$$

For Preikestolen, the mean normal stress at the interpreted sliding plane 133 meters (overlain by 95 meters of porphyritic granite and 38 meters of granitic gneiss) down from the top plateau was used to calculate the mean normal stress. This resulted in the calculation in equation 3.7 and gave a normal stress of 3.63 MPa.

$$\sigma_n = (95m * 26.40kN/m^3) + (38m * 29.70kN/m^3) = 3.63MPa \tag{3.7}$$

This value was further used with the instantaneous Mohr-Coulomb sampler in RocData (Appendix 1). This was done according to the basic principles in figure 3.21, sampling the instantaneous values at approximately $\sigma_n = 3.63$.

The input parameters were determined in the lab, in RocData, while the GSI was determined in the field. It was decided to use a disturbance factor of 0 in the analysis. As the residual friction angle, residual cohesion and residual tensile strength is also included in to RS^2 softwares, the residual values were set to 2/3 of the peak value.

Table 3.7: Parameters from the field, lab, and from RocData for the granitic gneiss.

Description	Symbol	Unit	Value	Reference
Uniaxial compressice strength	σ_c	MPa	227	Lab
E-module	E	GPa	88.3	Lab
Poisson's ratio	v	-	0.266	Lab
Unit weight	γ	kN/m^3	29.7	Lab
Estimateds for rock mass based on Hoek-Brown failuire criterion				
Geological strength index	GSI	-	80	Field estimates
Disturbance factor	D	-	0	Estimate
s (constant)	s	-	0.069	RocData
a (constant)	a	-	0.501	RocData
m$_i$, material constant	m$_i$	-	33	RocData (empirical)
Equivalent Mohr Coulomb parameters obtained in RocLab (for σ_n = 3.528)				
Peak cohesion	c$_p$	MPa	7.691	Inst MC sampler
Residual cohesion	c$_r$	MPa	5.127	2/3 of peak value
Peak friction angle	ϕ_p	°	66.78	Inst MC sampler
Residual friction angle	ϕ_r	°	44.53	2/3 of peak value
Deformation modulus	E$_m$	MPa	77734	RocData
Peak tensile strength	σ_t	MPa	-1.523	RocData
Residual tensile strength	σ_{tr}	MPa	-1.015	2/3 of peak value
Dilation angle	-	-	0	No dilatancy assumed

Table 3.8: Parameters from the field, lab and from RocData for the porphyritic granite.

Description	Symbol	Unit	Value	Reference
Lab-results				
Uniaxial compressice strength	σ_c	MPa	141	Lab
E-module	E	GPa	45.7	Lab
Poisson's ratio	v	-	0.32	Lab
Unit weight	γ	kN/m^3	26.4	Lab
Estimateds for rock mass based on Hoek-Brown failuire criterion				
Geological strength index	GSI	-	90	Field estimates
Disturbance factor	D	-	0	Estimation
s (constant)	s	-	0.264	RocData
a (constant)	a	-	0.5	RocData
m_i, material constant	m_i	-	28	RocData (empirical)
Equivalent Mohr Coulomb parameters obtained in RocLab (for σ_n = 3.528)				
Peak cohesion	c_p	MPa	9.26	Inst MC sampler
Residual cohesion	c_r	MPa	6.173	2/3 of peak value
Peak friction angle	ϕ_p	°	64.23	Inst MC sampler
Residual friction angle	ϕ_r	°	42.82	2/3 of peak value
Deformation modulus	E_m	MPa	43808	RocData
Peak tensile strength	σ_t	MPa	-2.369	RocData
Residual tensile strength	σ_{tr}	MPa	-1.579	2/3 of peak value
Dilation angle	-	-	0	No dilatancy assumed
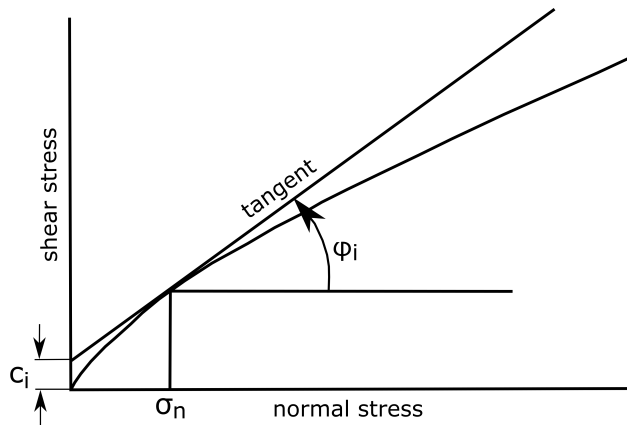
Figure 3.21: Basic principle used in RocData when applying the Instantaneous Mohr-Coloumb sampling tool. The instantaneous cohesion and friction angle was sampled at σ_n = 3.522. Figure modified from Hoek et al. (2000).

3.5.6 Input Parameters for Discontinuities

The calculated values in table 3.9 are based on the Barton-Bandis criteria, obtained as described in section 3.5.5. According to Barton (1973), the basic friction angle tested in the tilt test, can be assumed to be approximately the same value as the residual friction angle concerning natural joints. Therefore, the laboratory tested $\phi_r = \phi_b$ in this case for both the joints. The values for JRC was determined by measuring the three largest amplitude of the asperties between a 1 m ruler and the joint surface. The measured amplitudes were further converted to the JRC as explained in chapter 2.2.2. The JCS was set equal to the σ_c as there was a limited degree of weathering along the joint surfaces in the field. Due to the orientation of the joints, joint sets J2 and J3 is included.

Table 3.9: Parameters determined through fieldwork and laboratory tests. Two different values are used for each joint, as the values are slightly different dependent on the rock type.

Description	Symbol	Unit	J2	J3	Remark
Granitic gneiss					
Joint roughness coefficient	JRC	MPa	16	10	Based on field estimation
Joint compressive strength	JCS	MPa	227	227	Same as UCS
Residual friction angle	ϕ_r	°	33.73	33.73	Same as ϕ_b
Porphyritic granite					
Joint roughness coefficient	JRC	MPa	16	10	Based on field estimation
Joint compressive strength	JCS	MPa	141	141	Same as UCS
Residual friction angle	ϕ_r	°	37.47	37.47	Same as ϕ_b

Conversion from Barton-Bandis to Mohr-Coulomb parameters

In order to use the shear strength reduction method in RS^2 the parameters determined through the Barton-Bandis criterion needs to be converted to the equivalent Mohr-Coulomb parameters, which includes the instantaneous friction angle (ϕ_i), and the instantaneous cohesion (c_i) (Table 3.10). This conversion was carried out in RocData using the Instantaneous Mohr-Coulomb sampler, which is based on formulas from Hoek (2007). The same principles applies for the Instantaneous Mohr-Coulomb sampler tool used for conversion of the rock mass parameters, as the joint parameters were also sampled at $\sigma_n = 3.522$ MPa.

Table 3.10: Table with the converted values for the Mohr-Coulomb criterion. All the values are included in the model with joints in RS^2.

Description	Symbol	Unit	J2	J3	Remarks
Granitic gneiss					
Cohesion	c_i	-	2.025	0.698	RocData
Friction angle	ϕ_i	°	53.68	47.04	RocData
Porphyritic granite					
Cohesion	c_i	-	2.086	0.753	RocData
Friction angle	ϕ_i	°	54.07	48.68	RocData

Joint stiffness

Joint stiffness is defined by normal stiffness (K_n) and shears stiffness (K_s). These stiffness properties describes the stress-deformation response prior to sliding (Rosso, 1976). Calculation of the normal stiffness (K_n) is given in equation 3.8 and shear stiffness (K_s) in equation 3.9. The calculations are done for the joint sets J3 and J2. For both joints, the parameters for both the porphyritic granite, and the granitic is calculated.

$$K_n = \frac{E * E_m}{L(E - E_m)} \quad (3.8)$$

$$K_s = \frac{G_i G_m}{L(G_i - G_m)} \quad (3.9)$$

Where E is the intact rock modulus, and the E_m is the rock mass modulus. L is the joint spacing in meters, estimated through field observations. G_i is the intact rock shear modulus, and G_m is the rock mass shear modulus. They are calculated by equation 3.10 and 3.11, where ν is Poisson's ratio determined from the laboratory work. All input and calculated values are given in table 3.11.

$$G_i = \frac{E}{2(1 + \nu)} \quad (3.10)$$

$$G_m = \frac{E_m}{2(1 + \nu)} \quad (3.11)$$

Table 3.11: Input and result of the calculation of the joint stiffness parameters based on the formulas above. K_n and K_s are used as direct input in RS^2.

Parameter	J2		J3	
Input	Granitic gneiss	Porphyritic granite	Granitic gneiss	Porphyritic granite
E_i	88300 MPa	45700 MPa	88300 MPa	45700 MPa
E_m	77734 MPa	43808 MPa	77734 MPa	43808 MPa
L	10 m	10 m	15 m	15 m
ν	0.26	0.32	0.26	0.32
Calculated based on the values above				
G_i	35039	17310	35039	17310
G_m	30846	16593	30846	16593
K_n	64962 MPa/m	105815 MPa/m	43308 MPa/m	70543 MPa/m
K_s	25776 MPa/m	40059 MPa/m	17184 MPa/m	26706 MPa/m

3.5.7 Stresses

Historically the in-situ stresses, and its importance has often been ignored during analysis of slope stability Wyllie and Mah (2004). One of the reasons for this, is that stress in rock masses are not measured routinely for rock slopes. Also, as the major part of rock slides are driven by gravity, the in-situ stresses are interpreted to be minimal (Wyllie and Mah, 2004; Sandøy, 2012). Studies from Lorig (1999) did however show that the in-situ stresses had a large effect on the in-situ stresses during a SRF study of slope stability (Sandøy, 2012). This because materials that are weakened by internal deformation, can be effected to a large degree by the in-situ stresses. Therefore the in-situ stresses will play an important factor in the strength reduction and hence effect the stability (Hoek et al., 2000). Hence it is important to include stress measurements, as accurate as possible.

At Preikestolen, no measurements of the in-situ stress are available. Therefore, the values from the inner part of Lysefjorden, given in Hanssen (1998), was used as input data in the numerical analysis. However these measurements are taken approximately 25 km from the location of Preikestolen (Figure 3.22). Change in topography will effect the stress conditions, and vary from location to location (Nilsen and Broch, 2011; Krogh, 2017). The measurements from Hanssen (1998) are therefore not interpreted to be exact values for Preikestolen. The location of the stress measurements are from a slope with a different aspect and at an other elevation than Preikestolen. These factors apply a large uncertainty in the models, especially as the stress measurements was performed at a location with 650 m rock overburden. The data from Hanssen (1998) is given in table 3.12, and the fixed parameters fitted to the setup in RS^2 is shown in table 3.13.
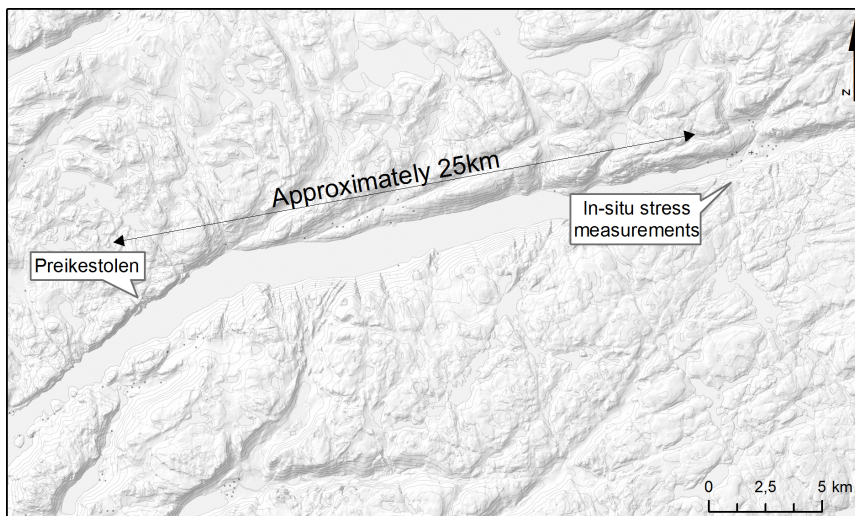
Figure 3.22: Location of the stress measurements registered in Hanssen (1998) relative to Preikestolen. An approximate distance of 25 km separates the two locations.

Table 3.12: In-situ stress measurements from Lysebotn (Lysefjorden01/Tjodan in Hanssen (1998)). These parameters are used as the basis for the stress input in the RS^2 model.

Background data					
Overburden (650m)	σ_v (MPa)	σ_H (MPa)	σ_H (°)	σ_h (MPa)	σ_h (°)
Borehole (Lysebotn)	21.6	6.4	98	6.1	8

Table 3.13: Input values and calculations of the stress based on the borehole measurements form Lysebotn. The parameters are used as the basis for the input of stress in the RS^2 model.

Input	Calculation	Value	Explamaition/reference
Use actual ground surface	γ*z	Will vary with depth	Uses the actual ground surface in the model to calculate the σ_v. The value will be based on the unit weight of both the granitic gneiss and the porphyritic granite.
Total stress ratio (horiz/vert in plane)	σ_H/σ_v	0.296	Since the slope is trending towards 140, σ_H is the closest to in plane stress.
Total stress ratio (horiz/vert out-of-plane)	σ_h/σ_v	0.282	Since the slope is trending towards 140, σ_h is the closest to out of plane stress.
Locked-in horizontal stress (in plane)	-	0	Not included
Locked-in horizontal stress (out-of-plane)	-	0	Not included

Chapter 4

Results

4.1 Field Observations and Measurements

The geometry of Preikestolen is made up by steep rock walls on each side and on the front plateau going almost directly into the fjord. One very distinct joint, which is easily recognized in the field is crossing the plateau, approximately 20 m from the front edge (Figure 4.1). This joint is fully developed across the plateau, with an opening of approximately 1 m. Another less visible joint is also crossing the plateau, however, this is not yet fully developed. The latter joint is easily recognized from the SW side of the rock formation, but can not be identified from the NE side.

Observations from the helicopter and from field photos (drone and from helicopter) shows that the rock formation consists of two different rock types. Preikestolen itself consists of both granitic gneiss, and porphyritic granite. The lower and the upper part of the rock formation consists of porphyritic granite with large feldspar crystals. The middle section of Preikestolen, approximately 30 m down from the top edge, consists of a band with granitic gneiss (Figure 4.2). The granitic gneiss is very fine grained, and the foliation is dipping with a shallow dip angle into the rock slope (approximately towards NW).

4.1.1 Structural Geology

During the fieldwork, the area was divided into three domains based on the structural geology. It was decided to divide the area, mainly due to a noticeable change in orientation of the joint sets. The three domains can possibly be seen in connection with the two weaker zones represented in the terrain as depressions, visible on the topographic map. This is based upon the slight change in the discontinuities on each side of these features (Figure 4.3).

The orientation of the structures are recorded as dip direction/ dip angle measured in degrees, and presented in an equal area, lower hemisphere stereonet (Figure 4.4). Included in the stereonet is the variability cone, that is calculated for one standard deviation (1σ). The variability is given as the radius of the variability cone of the specific joint set (in degrees) and the variation applies for both the dip angle and the dip direction.

Figure 4.1: Overview pictures of Preikestolen taken in the field. The rock formation is characterized by a flat top plateau, with steep rock walls on three sides. One joint is crossing the plateau, approximately 20 m from the front edge, and can be seen from all sides. The joint dividing the rock formation from the shallower slope behind, is only visible when seen from SW of Preikestolen.

Joint with a relatively wide opening on the SW side. Covered with sediments and loose rocks, and is less visible in the field.

Joint which can be seen from both sides of Preikestolen, but is less evident from the NE side.

Area with massive porphyritic granite. No visible foliation

Lithological boundary

Area with foliated granitic gneiss. Foliation dipping with a shallow angle into the slope.

Lithological boundary

Area with massive porphyritic granite. No visible foliation

Figure 4.2: Geological model of Preikestolen based on observations from helicopter, photos, 3D models and from fieldwork. Preikestolen is built up by two lithologies. The upper part consist of porphyritic granite with large feldspar crystals. This rock type is also present at the lower part of Preikestolen. The middle section consist of granitic gneiss.
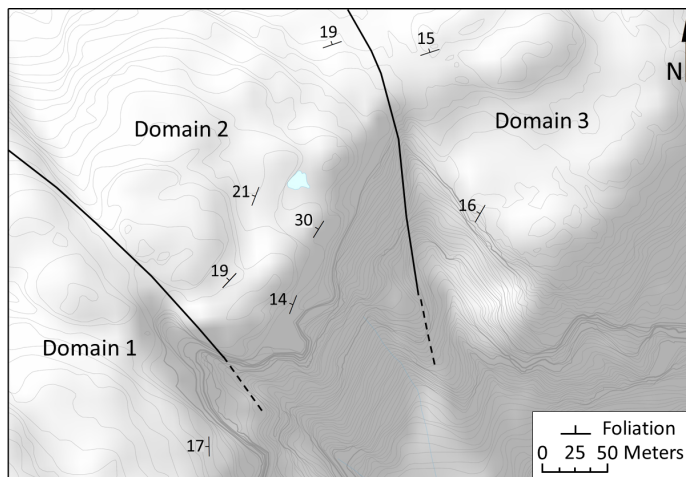
Figure 4.3: The area was divided into three domains based on the field data. Domain 2 is the domain that includes Preikestolen. The foliation is relatively consistent throughout all the domains. The background map is based on 10 m contours from an existing DEM.

4.1.2   Domain 1

The area west of Preikstolen was named domain 1. Only 86 measurements were gathered in this area, as it is quite distant from the main focus which was closer to Preikestolen. Four structures were recognized both in the field and in the stereo-graphic projection of the data.

Two of the join sets (J1 and J2) are very steep (mean dip angle of 84° and 83°), meanwhile joint set J3 has a shallower dip angle (73°). In this area, the foliation was hard to measure, as it was only sparsely present in a few of the measured locations. At the few locations the foliation was recognized, the dip was shallow (21°) and the dip-direction towards W/NW.

4.1.3   Domain 2

Preikestolen and the surrounding area were named domain 2, due to the similar orientations of the structures within this area. This domain contains the highest amount of structural measurements, as a consequence of it being the main focus in the field.

Three joint sets were recognized in the field and in the stereographic representation of the results (Figure 4.4). The two steep joint sets (J1 and J2) that were found in domain 1, are also present in domain 2. However, J2 has a dip oriented NW/SE in domain 2, rather than NNW/SSE that was measured in domain 1. The mean dip angle of J2 is also steeper (87°) in domain 2 than domain 1. The joint set J3 had the largest change in orientation from domain 1 to domain 2. In domain 2, J3 is shallower (52°) than in domain 1.

The foliation measured in domain 2 is oriented in a very similar manner as domain 1, dipping approximately 18 degrees towards the NW. Some measurements in domain 2 also showed a dip towards the west. However, due to the lack of a specific concentration, this was not defined as a joint set. Since domain 2 is the domain which will be the main focus, a more precise description of the join sets are included in the following pages.

4.1.4   Domain 3

Domain 3 is the area to the east of Preikestolen. Only 84 measurements were gathered in this area, as it was (like domain 1) not the main focus during the fieldwork. In domain 3, five distinct structures were defined based on the field data. The structures included four joint sets in addition to the foliation.

In this area, the measurements dipping approximately 74° to the west were defined as a individual joint set (J4). The joint set J4, is relatively similar to the joint set J2 from domain 2, however it was decided to separate this concentration as an individual joint set. Otherwise, the orientation of the joint set J3 and the foliation are relatively similar as in domain 2. The joint set J1 in domain 3, is almost identical to J1 from domain 2. However, in domain 3, J1 is dipping more towards the north than in the previous domains.
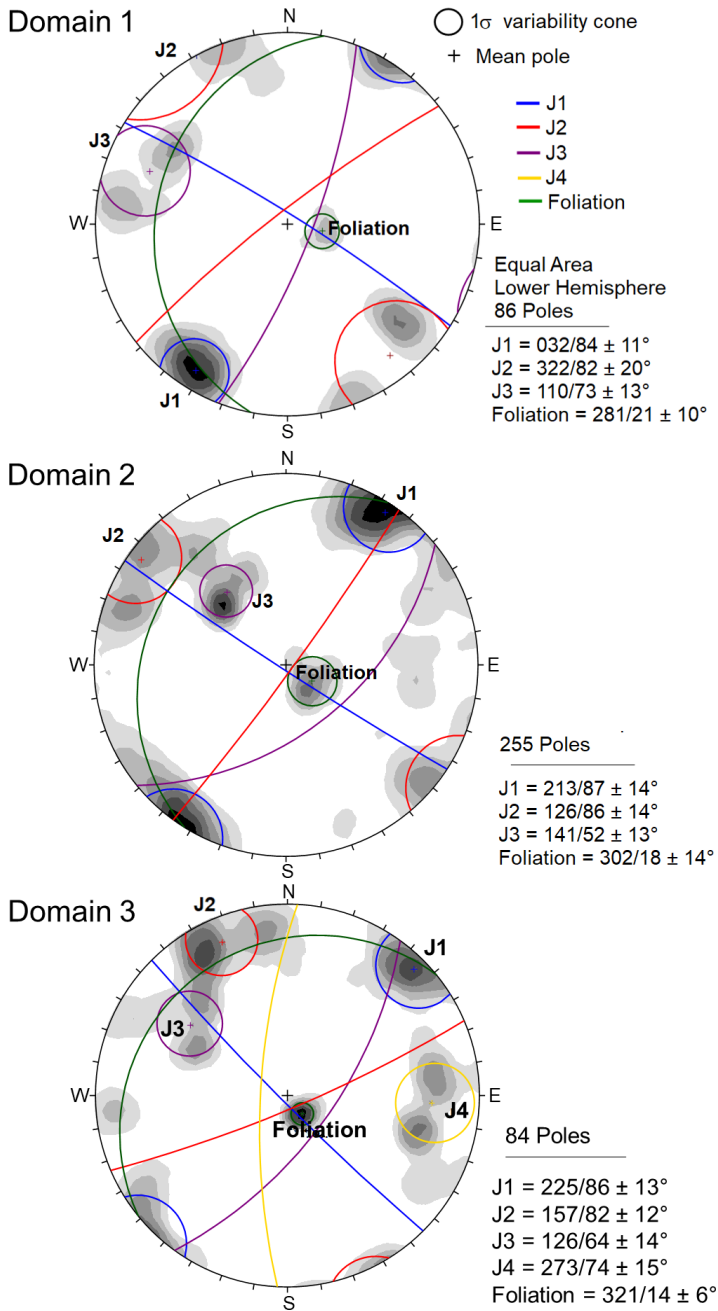
Figure 4.4: Stereographic presentation of the three domains. The joint sets are oriented relativley similar in all the domains. However, there are some noticable changes. Joint set 4 was separated out as an individual joint set in domain 3.

The following descriptions of the joint sets are based on the data from domain 2, as this is the domain of Preikestolen and hence will be the focus in this thesis. An overview of how the discontinuities appear in the field is shown in figure 4.5.

- **J1**

  Joint set 1 has an average dip of 87 ° and a dip direction of 213. This joint set is interpreted as the joint set than has formed the lateral limits of Preikestolen at the north-eastern and the south-western side (Figure 4.5). The dip direction that was recorded showed dipdirections both towards north-east and south-west, as was expected due to the very steep dip.

- **J2**

  Joint set 2 has an average dip of 86 ° and a dip direction of 126. The dip direction of the joint set was recorded both towards north-west, and south-east. This joint set is interpreted as the one that forms the steep front of Preikestolen, with an almost vertical drop into the fjord.

- **J3**

  Joint set 3 has an average dip of 52 ° and a dip direction of 141. This joint set is dipping approximately towards the same direction as J2, however J3 has a significantly shallower dip. This joint set is visible in the overview photos from Preikestolen as the relatively shallow joint set dipping out towards the fjord.

- **Foliation**

  In the granitic gneiss, the foliation was clearly more visible than in the porphyritic granite. However, the porphyritic granite also shows a slight deformation which is mainly visible on the rock samples investigated in the lab. During the field work, no foliation measurements were done in the areas containing porphyritic granite. In general, the foliation dips towards the north-west direction in the whole area surrounding Preikestolen. The dip is relatively shallow, with an average dip of 14 ° and oriented with a dip direction towards 302.

The joint crossing the plateau approximately 20 m from the front edge, is oriented in a similar direction as J2. Furthermore, the not fully developed joint at the transition between the plateau and more shallow plane, is build up by a combination of both joint set J3 and J2. The latter back scarp starts relatively shallow, but is steeper further down.
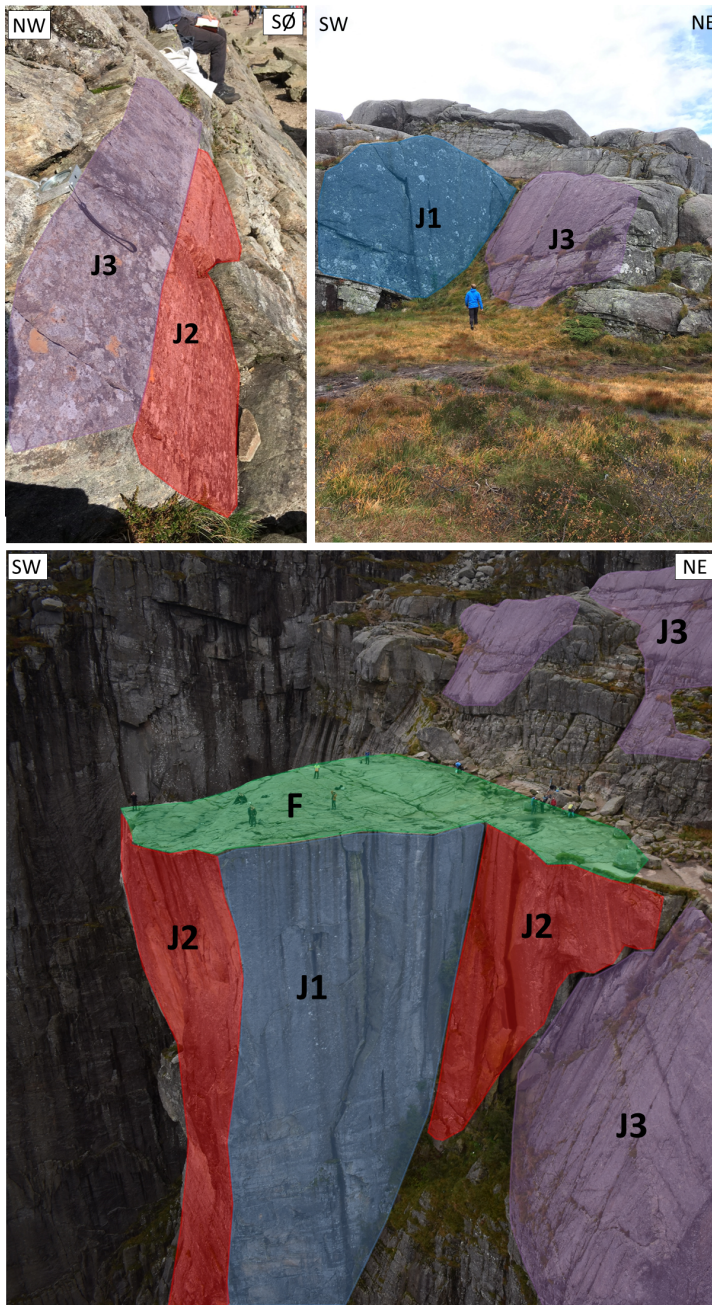
Figure 4.5: The joint sets observed in domain 2 shown in pictures from the field and helicopter. The domain consist of three joint sets, in addition to the shallow dipping foliation.

4.2   3D Models

All the four 3D models that were produced during this study, are based on data collected in the field in September 2017. The main tool used to process and put together the photogrammetry models, was Agisoft Photoscan. The photogrammetry models were edited by Pierrick Nicolet at NGU, due to the large amount of data, requiring a very large data capacity and a extensive processing time. The quality of the photos was evaluated as good both for the drone and SLR 1 photos. However, the photos used to create the SLR-2 model, had a poorer quality. The processing of the photos generally consisted in deleting the photos that were "blurry" and had a large error number, in addition to deleting obviously miss-placed points in the point cloud. The miss-placed points were for example due to humans on the plateau of Preikestolen.

The LiDAR scans were put together by the author, using the Pifedit tool in Polyworks. In Pifedit, excessive points due to for example vegetation and humans were deleted. The scans were matched using the Imalign part of the Polyworks package. The scan from the opposite side of Preikestolen was used as a basis for referencing the other clouds, as it covered a very large area. However, there was a poor overlap between some of the scans, which made the task of combining them challenging. This problem especially occurred when matching the scan covering the top plateau. Despite the challenges due to the poor overlap, the quality of the matched scans were evaluated as relatively good.

SLR 1

The first SLR model (Figure 4.6 a) was at the first impression considered a relatively good model. Several important features, like the joint crossing the plateau and the joint at the back of the plateau were visible. During the editing of the photos for this model, relatively few photos were removed. The coverage of terrain is also good for this model, as for both the models based on the SLR photos. The point density in the model measured with the point to point distance tool in CloudCompare, proved that the SLR 1 is very consistent. The point density was measured at five spots in the model (Figure 4.7) resulting in a point spacing of approximately 4 cm throughout the model (Table 4.2).

SLR 2

The second SLR model (Figure 4.6 b) was by the first look considered to be of relatively poor quality. As the light conditions were not as god at 5 p.m. as it was at 9 a.m., the quality of the photos were poorer, and hence the quality of the model itself. Additionally, the settings of the camera were not correct, as the exposure time was too low. As the helicopter was moving during the whole photographing sequence, the wrong settings did also drastically reduce the quality of the photos. Despite the lower quality, several of the important features (like joints) are visible, and the coverage of the model is good. The point density was, as in the first SLR model, consistent. However, the point density was slightly lower, and varied from 6 cm to 7 cm.

Drone

The drone model (Figure 4.6 c) was from before connected to the coordinates as the route, photo location and angle of the camera was planned on forehand by NGU (in ArcGIS and Litchi). This is an advantage when modelling with drones, as there were a very low amount of poor quality photographs taken by the drone. The model had a relatively good cover. However, the point density was somewhat more variable than for the SLR models. Around the top of the Preikestolen formation, the point spacing was approximately 5 cm. At the lower part of Preikestolen, on the other hand, the point spacing was approximately 10 cm, and even decreasing further down from the measured point.

LiDAR

The seven different scans were put together in Polyworks/Imalign, to create the LiDAR model (Figure 4.6 d). The quality was at first impression considered to be relatively good. However, a small gap between the two scans can be seen in the model between the top plateau and the steep front and sides. The gap probably appears due to the poor overlap between the scans. Other than this, a large amount of features such as joints are visible. Due to the various distances between the scanner and the scanned surface, the point density is also variable. The point spacing varied from 2 cm at the top plateau to 20 cm at the lower part of the slope. The closest point spacing was obtained where the scanner was at its closest position to Preikestolen. The largest point spacing was found where the data were acquired from across Lysefjorden (approximately 2000 m apart).
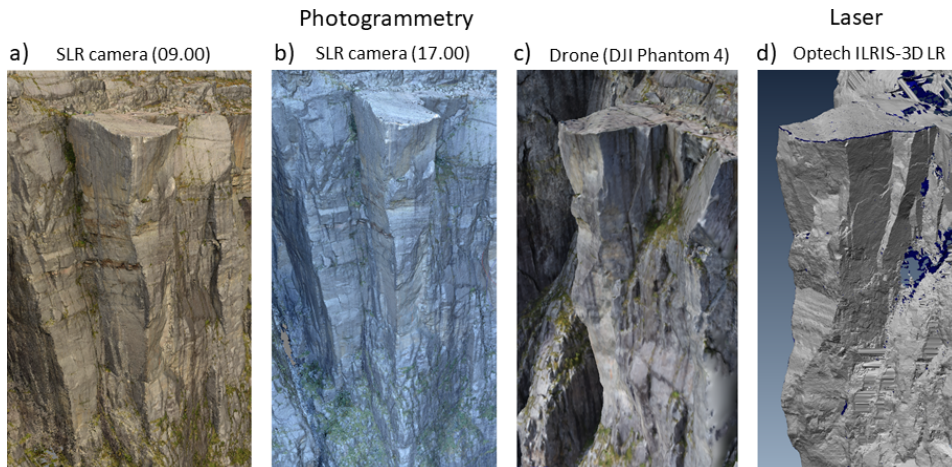
Figure 4.6: Figure showing the four 3D-models displayed in CloudCompare (a,b, and c) and Polyworks (d). a) The model based on the pictures taken from helicopter the 16th of September (9 a.m.).; b) The model based on the photos from helicopter taken the 18th of September (5 p.m.).; c) The model based on drone photos.; d) The model based on the LiDAR scans.
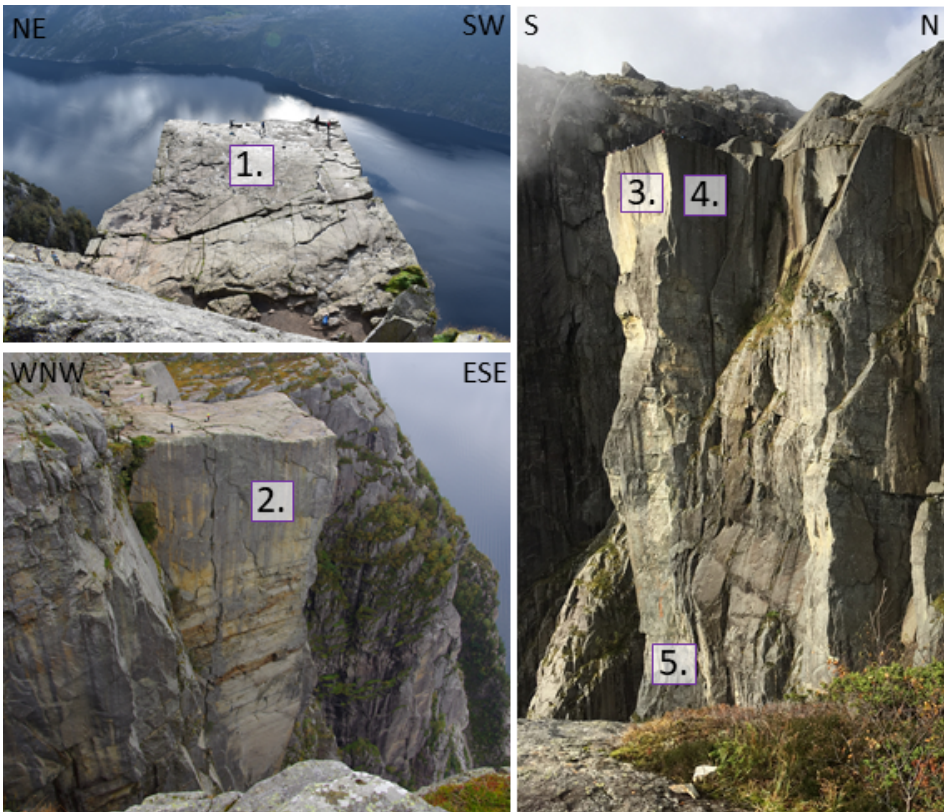
Figure 4.7: Five locations at Preikestolen were used to measure the point density of the point clouds. The point distance was measured for all the point clouds, using the point to point tool in CloudCompare. The locations were chosen to get a relatively even distribution of the measurements, with the main focus of the top plateau and lateral surfaces of Preikestolen.

Table 4.1: The measured point distances in the four point clouds, based on the locations in figure 4.7. The SLR models (especially SLR 1) have a relatively even point distance throughout the model, while the LiDAR model was less consistent due to the variation in distance between the scanner and the slope side.

Location (in figure 4.7)	LiDAR	Drone	SLR 1	SLR 2
1.	2 cm	5 cm	4 cm	6 cm
2.	2.5 cm	5 cm	4 cm	7 cm
3.	4 cm	5 cm	4 cm	6 cm
4.	3 cm	5 cm	4 cm	6 cm
5.	20 cm	10 cm	4 cm	6 cm

4.2.1 Evaluation of the Georeferencing

All the models were georeferenced to the drone model. This was done during the step wise work-flow as suggested by CloudCompare (CloudCompare, 2018), which is rendered in the following list.

- **Match bounding-box centers**
  This is done to match the two boxes that are surrounding each model, so that the center is shared. It makes the georeferencing slightly faster, as the two models are in the approximately same area.

- **Interactive transformation tool**
  This is done to manually move and rotate the model that is georeferenced closer to the reference model.

- **Align (point pairs picking) tool**
  Several points are picked that can be recognized in the two models. In some cases this is accepted as the final georeferencing. However, in this case the two additional steps are included, as the precision of the georeferencing is important.

- **Segmentation tool**
  This tool was used to cut off some parts of the larger model, to make the georeferencing faster and more precise, in addition to shortening the computation time of the comparison of the models.

- **Fine registration (ICP) tool**
  With this tool, the final and most precise georeferencing is done. This can only be done when the two clouds are roughly referenced from before.

After the georeferencing was carried out, the point clouds were compared, as the cloud to cloud distances were computed. Both the drone and the LiDAR data were used as a reference for the comparison of the models. The comparisons were done for the following point clouds:

1. Drone compared to SLR 1

2. Drone compared to SLR 2

3. LiDAR compared to drone

4. LiDAR compared to SLR 1

5. LiDAR compared to SLR 2

The reason for using the LiDAR and the drone model as the basis for the comparison, is that the drone was already georeferenced, and that the LiDAR was the expected best quality data set prior to fieldwork. After the georeferencing, the LiDAR data was compared to the drone and the helicopter models. The comparisons were done by measuring the cloud to cloud distances.

SLR 1 compared to drone

A comparison of the cloud to cloud distance between the SLR 1 and the drone point cloud is shown in figure 4.8. In this comparison, the areas where the point spacing between the two models is less than 1 m are included. From what could be seen in this comparison, the georeferencing was very good close to Preikestolen, and at the plateau at the top of Preikestolen. These areas are almost entirely covered in dark blue, representing a short distance between the two point clouds.

The quality however was decreasing towards the lower part of the comparison. This might be due to the lack of data from the drone, as this was manoeuvred from the top of the plateau. Thus important data from the lower part of the rock slope were not included, as it was not evaluated as proper to fly the drone too far down. Another explanation can be connected to the focus on Preikestolen itself during the photography from the helicopter. However, as presented earlier, the drone model had a poorer point spacing within the model towards the lower part of the slope, while the SLR 1 model, had a very consistent point spacing. Taking even photos with the SLR camera was also a high priority during the fieldwork, supporting that the main issue lies in the drone model.
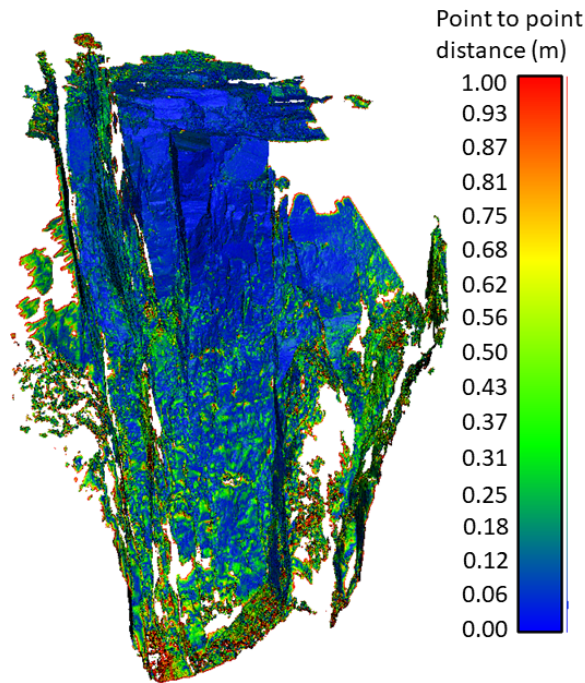
Figure 4.8: The difference between the drone model and the SLR 1 model. The colors represent the cloud to cloud distance. The scale bar is from 1 to 0 meters, and all distances that exceed 1 meter are deleted from the comparison.

SLR 2 compared to drone

The same tool as for the previous comparison was used to compare the SLR 2 and the drone point cloud, and the cloud to cloud distance is presented in figure 4.9. The comparison of these models showed that the difference between the models is relatively large. There was an overall large difference between the areas, even though the area to the right of Preikestolen, is covered in dark blue, and thus has a good match between the two point cloud sets.

Despite the area which shows a section with closely spaced point clouds, the slope face at Preikestolen itself shows approximately 0.5 m spacing. Towards the left side of Preikestolen, the distance between the point clouds is increasing. These results was somewhat unexpected, as the SLR 2 has an even point spacing throughout the model. In addition to this large error connected to the SLR 2 model, the large point cloud spacing towards the bottom of the comparison is expected to come from the poor quality of the drone model towards the bottom of the slope.
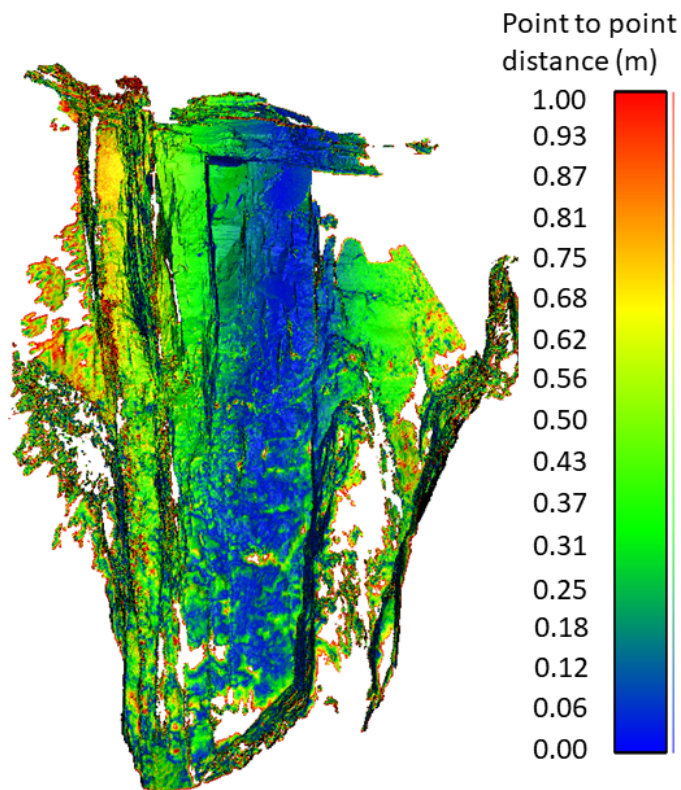
Figure 4.9: The difference between the drone model and the SLR 2 model. The colors represent the cloud to cloud distance. The scale bar is from 1 to 0 meters, all distances of more than 1 meter is deleted from the model.

LiDAR compared to drone

The difference in the cloud to cloud distance for the LiDAR and the Drone point cloud is presented in figure 4.10. The figure shows a similar error towards the lower part, as the two previous comparisons, hence this can also be explained by the poor drone quality in this area. However, the point spacing in the LiDAR model was also poorer in this area (approx 20 cm), which might also contribute to the poor overlap.

The sides of Preikestolen, on the other hand, are covered in dark blue, and the cloud to cloud distance is low. However, the top plateau of Preikestolen, which has a good point spacing in both the models, shows areas with an error of up to 0.5 meters. This can be connected to the poor overlap between the scans. As there were few reference points during the fitting of the various scans. However, the sides that had a good overlap between the scans, show a good correlation between the two point clouds.
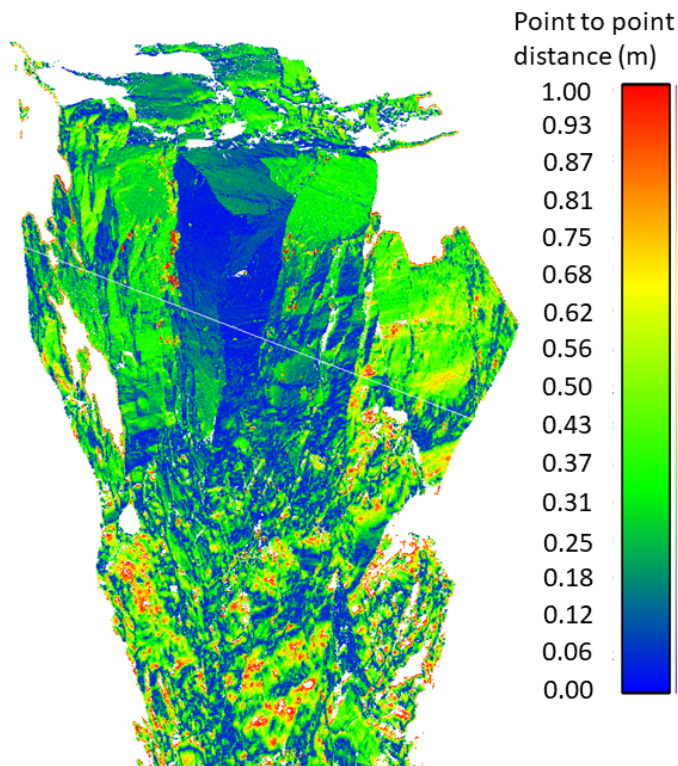
Figure 4.10: The difference between the LiDAR model and the drone model is very low around the area of Preikestolen. However, towards the lower part of the model, the difference between the two models is increasing. The scale bar is from 1 to 0 meters and all areas with a difference of more than 1 meter are deleted from the model.

LiDAR compared to SLR 1

Figure 4.11 shows the distance between the LiDAR point cloud and the SLR 1 point cloud. The result is relatively similar as for the comparison between the LiDAR and the drone model. This was expected since the comparison between the SLR 1 and drone model, was very good. However, in this case, the areas above the plateau shows a good match, while the steep sides at Preikestolen has a larger difference. This can be caused by the error in the LiDAR scans, as the orientation of the planes are correct while the distance between the scan is different.

Towards the lower part of the model, the number of holes is significantly lower than for the drone and LiDAR comparison. However, there are still a poorer match in this area between the LiDAR and the SLR 1, than for the rest of the model. This is interpreted to have been effected by the large point spacing between the points in the LiDAR cloud, as it was large (approximately 20 cm) in this area. Another explanation can be vegetation, as the lower area was more vegetated, than the top block.
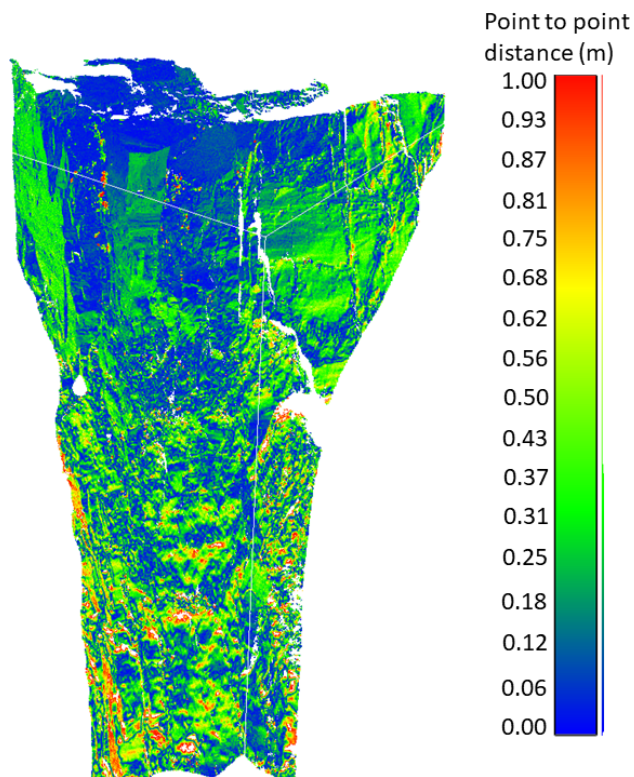
Figure 4.11: The difference between the LiDAR and the SLR 1 point cloud is very low around the area of Preikestolen. However, towards the bottom om the model, the difference between the two models is increasing. The scale bar is from 1 to 0 meters and all distances of more than 1 meter are deleted from the model.

LiDAR compared to SLR 2

When comparing the LiDAR model to the SLR 2 model, it was no doubt that the result was very poor. This is shown in figure 4.12, where the area that was closer than 1 meter was small. The area covered in grey, represents distances of more than 1 meter, and is dominating the comparison. Due to the poor result, it was decided not to use the SLR 2 model further. This was also supported by the previous observations from comparing the SLR 2 model to the Drone model. Thus this comparison only strengthened the previously evaluation of the model based on the photos taken by SLR camera at 5 p.m.

The poor overlap between the two models could however also be connected to the point cloud from the LiDAR scans, as it has a large variety in the point density throughout the model. However, since the overlap between the LiDAR and the other SLR model is much better, the poor overlap is interpreted to be mainly connected to the errors in the SLR 2 point cloud.
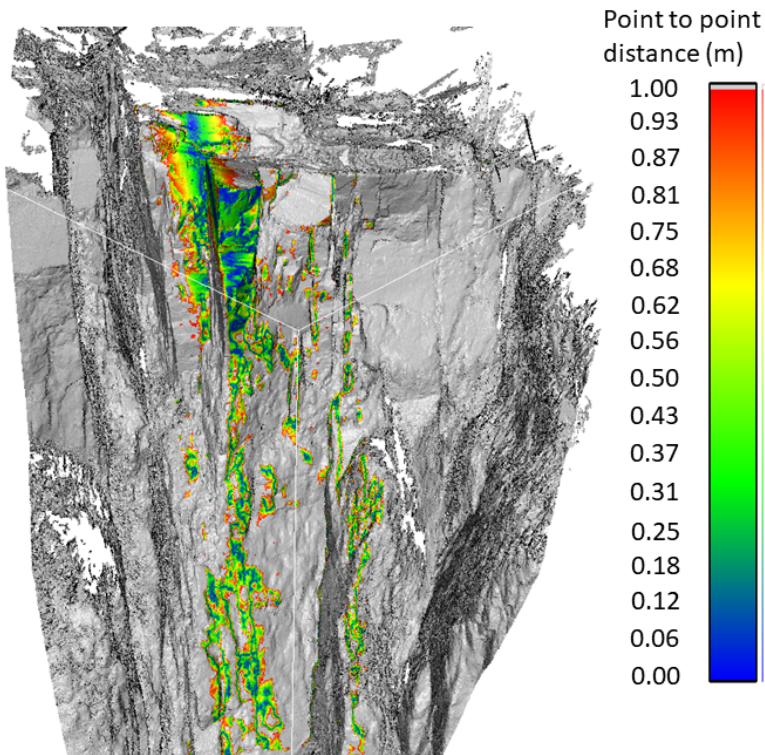
Figure 4.12: The difference between the LiDAR model and the SLR 2 is higher than 1 m for large parts of the comparison (>1 is grey). The scale bar is from 1 to 0 meters.

4.2.2 Volume Estimation

To calculate the volume, the drone point cloud was imported to CloudCompare. The model was cut along the existing joints visible in the model, and the tool Poisson's surface reconstruction was used to make a closed mesh which could further be used to estimate the volume. Two scenarios were cut out of the drone model. One based on the large joint at the back of Preikestolen, while the other one at the fracture crossing the plateau further out. Further, the tools "Mesh" and "2.5 Volume" were used, to get an estimate of the volume.

The first and largest scenario (scenario A), based upon the open joint covered with sediments and blocks in the field, had an estimated volume of approximately 120 000 m^3. The scenario also included the smaller block located at the right (east) side of Preikestolen. The smaller scenario (scenario B) based on the visible joint crossing the plateau was cut along the joint, as far as it could be detected. The calculation for scenario B resulted in a volume of approximately 55 700 m^3, which is approximately half the volume calculated for scenario A. However, this calculation is only a rough estimate of the volume. There was a large uncertainty of the lower part of both the scenarios, as none of the joints daylights the slope. Therefore the lower part of the volume calculation is not very precise. Even though it is not an exact calculation, the volume estimations are good indicators of the possible sliding volume.
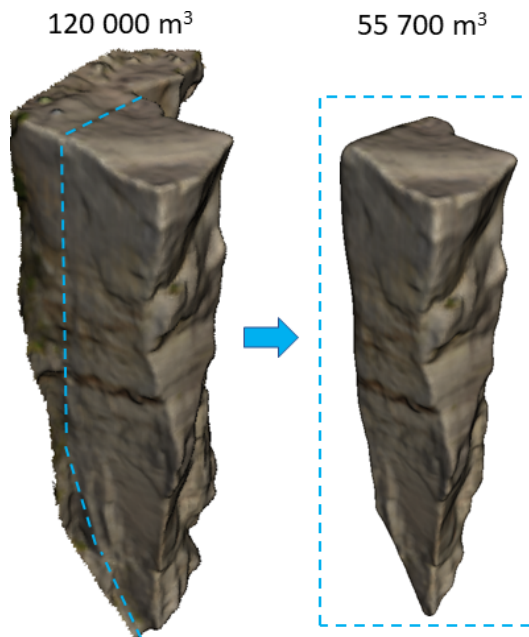
Figure 4.13: The volume of the two possible scenarios was calculated in CloudCompare. The outer boundaries of the scenarios are based on observations done in the field and on the 3D models. The simple calculation in CloudCompare show that the volume in scenario A is approximately twice as large as in scenario B.

4.3 Coltop 3D

Based on the results from the comparisons, it was decided to use both the LiDAR and the SLR 1 model to gather the structural measurements. The SLR model imported to Coltop 3D is shown in figure 4.14, and shows two distinct steep joint sets. The steep joint set J1, can be recognized from the colors green/turquoise and pink, while the other steep set, J2, is shown in blue and yellow. The somewhat shallower joint set J3 is colored in orange. The top plateau of Preikestolen can be recognized as white, and is thus very shallow dipping. The results from the LiDAR model was very similar to the SLR model. However, as previously mentioned, the coverage of the LiDAR model (with high point density) was poorer than for the SLR model. The quality of both the models does however seem to be good, as they are very similar in appearance.
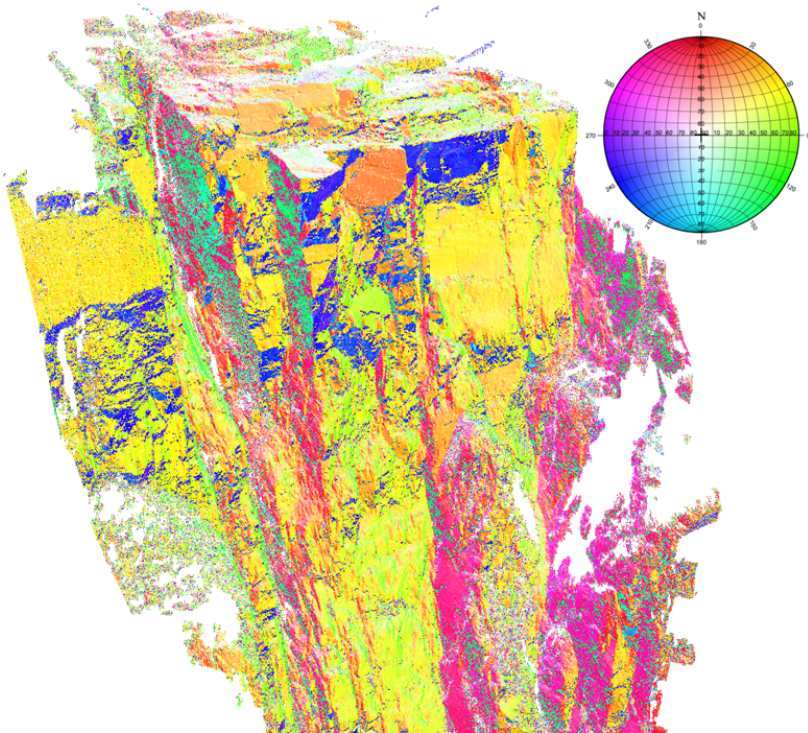
Figure 4.14: The SLR 1 point cloud imported to Coltop 3D, where each orientation is colored in a unique color. All structures that were mapped in the field, were also recognized in the Coltop 3D model.

For both models, measurements were taken from all the distinct colors to include all the important structures. The data was then exported to DIPS via Excel, to be presented in stereonets. The measurements from the SLR 1 model and the LiDAR model are also compared to the field data presented i figure 4.15. Only the field data from Domain 2 were used in the comparison, as explained in chapter 4.1. The mean orientation of the various joint sets is presented in table 4.2 for an easy comparison.

The measurements show that the structures gathered in the field are relatively similar to the once collected from the 3D point cloud. This is especially when it comes to joint set J2 and joint set J1, as the orientation is almost identical in all the stereonets. These sets were easy to measure in the field, and are also visible in all photos from Preikestolen, as they are the once that define the steep edges of the rock formation. Joint set J3 is also similar in all of the stereonets. However, the dip angle is slightly steeper in the data from the SLR 1 model. The variation is yet very small, thus it is still considered acceptable.

The foliation on the other hand, did vary to a relatively large extent compared to the other structures. In the field, the average dip-direction and dip angle were measured to 302/52, indicating a dip towards the NW. The data from the LiDAR model show foliation with a dip angle of 5 ° towards the E/NE. On the stereoplot based on the SLR 1 point cloud, the foliation dips towards NE with a dip of 9 .

One explanation for the variation in the direction of the dip, can be due to the very shallow dip. However, the main reason is probably that the measurements gathered from Coltop 3D only included the area on the top plateau. The plateau has a relatively undulating surface, probably accounting for the large variation in the orientation. An overview of the various orientation of the structures based on the source is presented in table 4.2.

Table 4.2: Mean orientation of the various discontinuities mapped in the field and gathered from Coltop 3D. The orientation is shown in dip direction and dip angle, with one standard deviation. The largest change in orientation is seen in the foliation measurements.

Joint set	Fieldwork	SLR-1	LiDAR
J1	213/87 ± 14°	209/89 ± 12°	211/89 ± 11°
J2	126/86 ± 14°	122/82 ± 17°	124/79 ± 17°
J3	141/52 ± 13°	151/58 ± 12°	144/54 ± 07°
Foliation	302/18 ± 14°	034/09 ± 05°	077/05 ± 10°
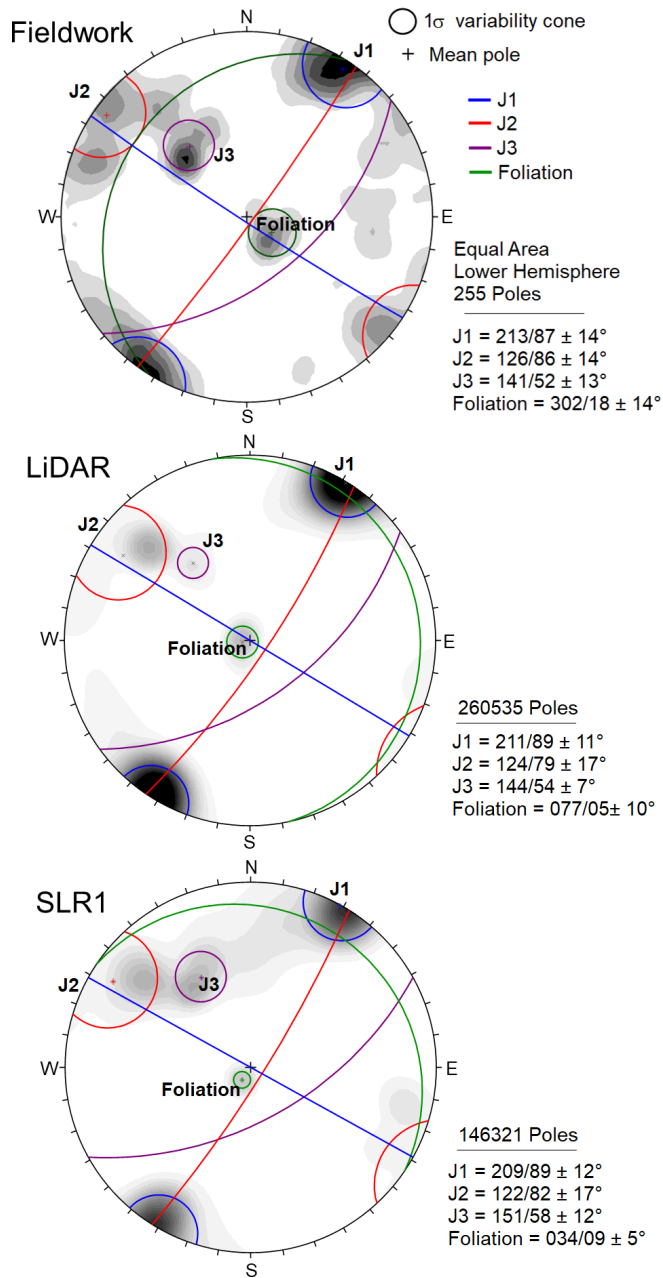
Figure 4.15: Stereographic presentation of the data from the field, compared to the data gathered in Coltop 3D. All the joint sets are oriented relatively similar in all stereonets. However, the orientation of the foliation is different in the data from both the SLR 1 and LiDAR, compared to the field measurements.

4.4   Kinematic Analysis

Since all the measurements show a relatively similar result, it was decided to carry out the kinematic analysis on the field measurements, and compare it to the data from Coltop 3D. As all the measurements were relatively similar, the kinematics are also expected to be similar. This is mainly because none of the smaller changes is considered to have an effect on the stability.

However, the case at Preikestolen is relatively complicated, as there is no lateral limits for the sliding direction. Therefore, the recommended standards of using a 30° lateral tolerance from Hermanns et al. (2012b), are not used in this analysis. In theory, sliding could occur in both NE, SW and SE direction (Figure 4.16). Because this study is focusing on the large rock formation, and not smaller blocks on the plateau, failure towards SE is the main focus. It could however not be excluded, that smaller blocks can fail in NE and SW direction even though they are not seen in the kinematic analysis.

The measurements from the field show a kinematic feasibility that is feasible for all the failure mechanisms (Figure 4.17). Planar failure is possible along the joint sets J3 and J2, as both sets are oriented with a dip towards the SE with a steeper angle than both friction cones. The friction cones that represents the basic friction angle for granitic gneiss (33.73°) and porphyritic granite (37.47°). Both joint sets are also within the daylight envelope (J2 only partly). Wedge failure is possible due to the intersection between J1 and J3. Toppling is possible due to the steep joint set J2 and J1, as they are both partly within the critical area of toppling failure. The slip limit is based on slope angle and friction angle (slope angle - friction angle).

The kinematic feasibility test from the measurements done with Coltop 3D based on the 3D models from both SLR, drone and LiDAR, show that the data gathered in the field are also representative for the area further down on Preikestolen. Due to the extremely large amount of measurements from the Coltop 3D model, the stereonets were only compared to the kinematic feasibility test. Including the measurements from Coltop 3D, would entirely outnumber the field measurements if combined.
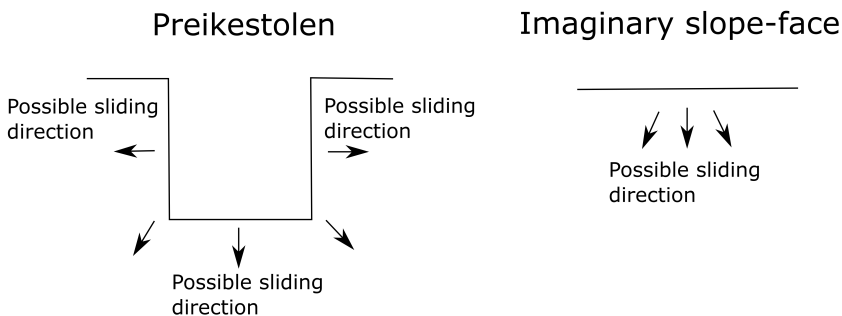
Figure 4.16: Sketch (from above), showing why no lateral limits are included in the kinematic analysis of Preikestolen. Sliding is theoretically possible in several directions. Dimensions and orientation of the slope are not correct in the sketch.
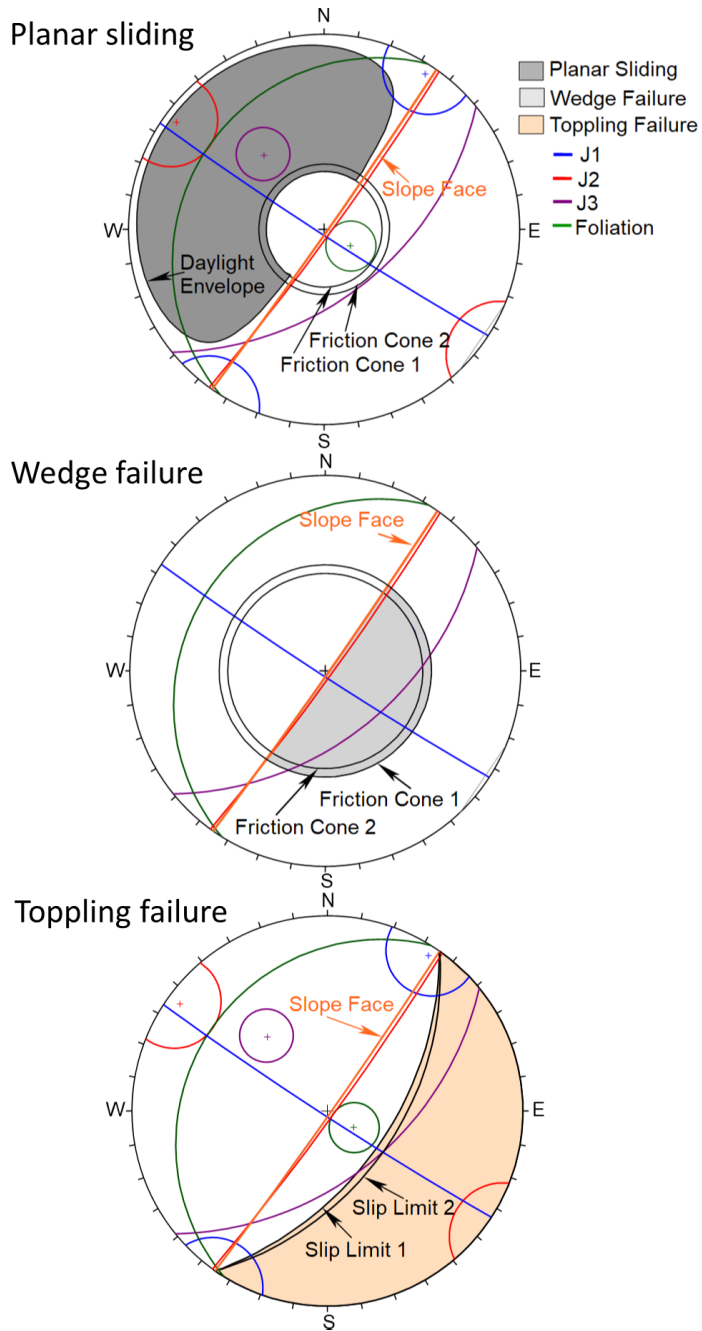
Figure 4.17: The kinematic analysis based on the field measurements show that all kinematic failure mechanisms are possible.

4.5 Numerical Analysis

4.5.1 Final Setup of the Models

Based on the previously mentioned settings and input, two models of Preikestolen was created. Model 1 is shown in figure 4.18, and does not contain any joints. The reason for this was to investigate the stability entirely based on the geometry of the rock formation, and to calculate the critical SSR for a rock slope with no joints. The lithological boundaries between the porphyritic granite and the granitic gneiss is based on interpretations from photos and from the 3D models. The area included in the SSR analysis is marked with a dashed gray line. No groundwater table is included in the model. The reason for excluding water is due to possibility of building of a high water pressure at Preikestolen is low. The joints is very open, and the water can easily escape through the sides.
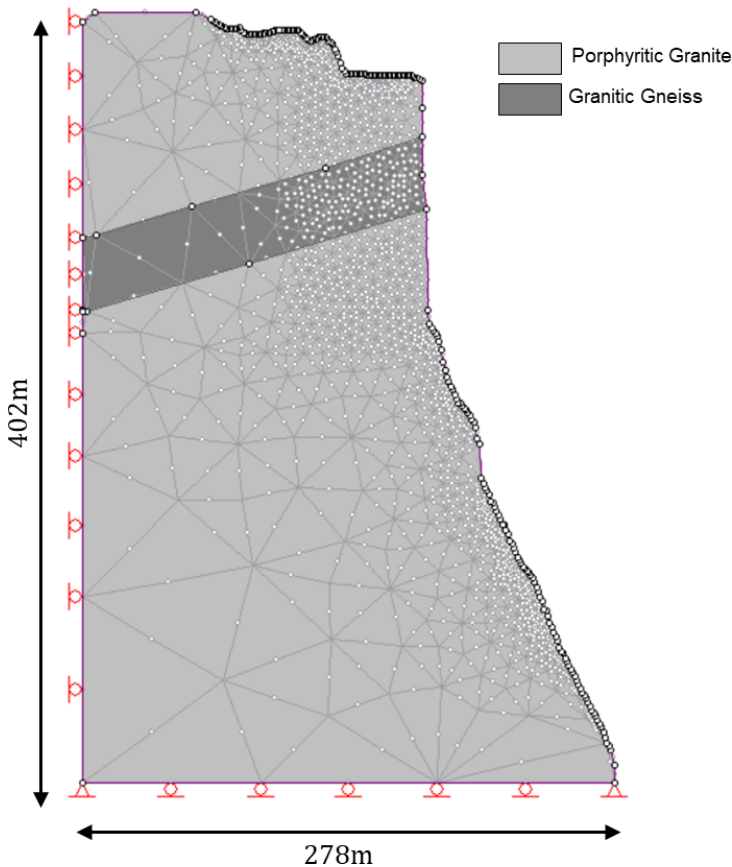
Figure 4.18: The basic numerical model without joints created in RS^2. The main part of the model consist of porphyritic granite, with a middle section of granitic gneiss.

In Model 2 (Figure 4.19), the two joints registered in the field is included. The orientation and extension of the joints is based on field photos, in addition to the LiDAR and photogrammetry models. The area included in the SSR analysis is the same as for the first model. However, the SSR is also applied for the joints. The input values for the joints varied both from J2 to J3, and from rock type to rock type. Hence both joint sets has two different sets of input parameters based on which rock type the joint intersects. As for the first model, no groundwater is included in Model 2.
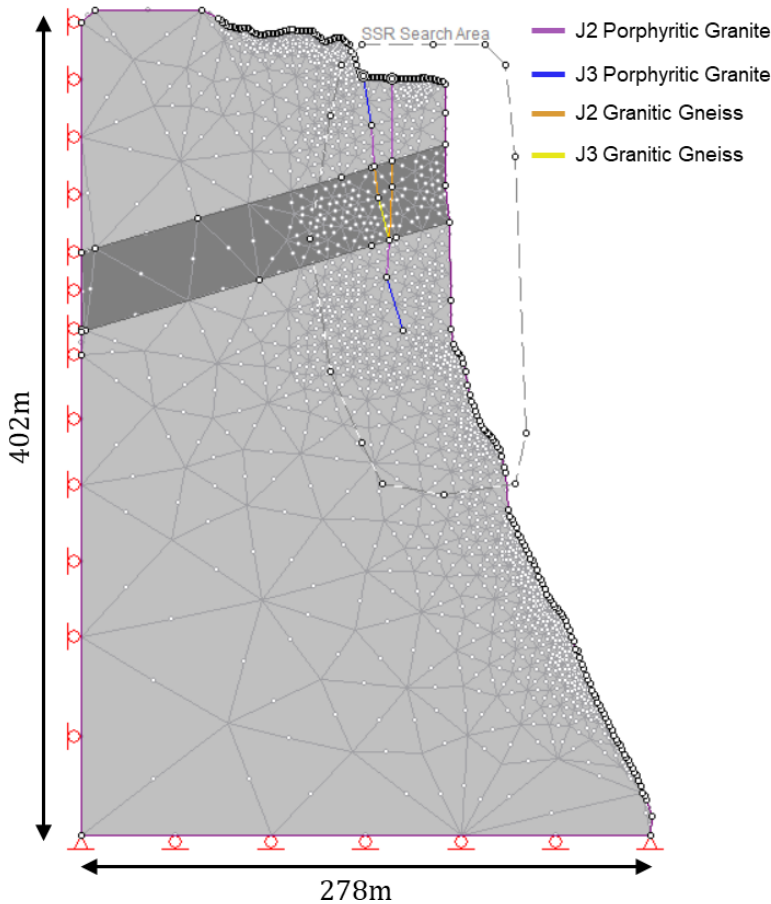
Figure 4.19: The geometry of the numerical model in RS^2 with joints included. Both joint sets converge at the lower part of the granitic gneiss. Parameters used for the joints varied based on which rock type the joint intersects.

In addition to the previously presented models, a modified version of model 2 was created with an extended joint. The joint was extended with a lower dip that observed in the field in order to daylight the slope. The extension of the joint is given the same joint-properties as J3, as this is the one closest to the orientation of the continuation. Otherwise, all the joints have the same properties as in model 2. Model 2a is presented in figure 4.20.
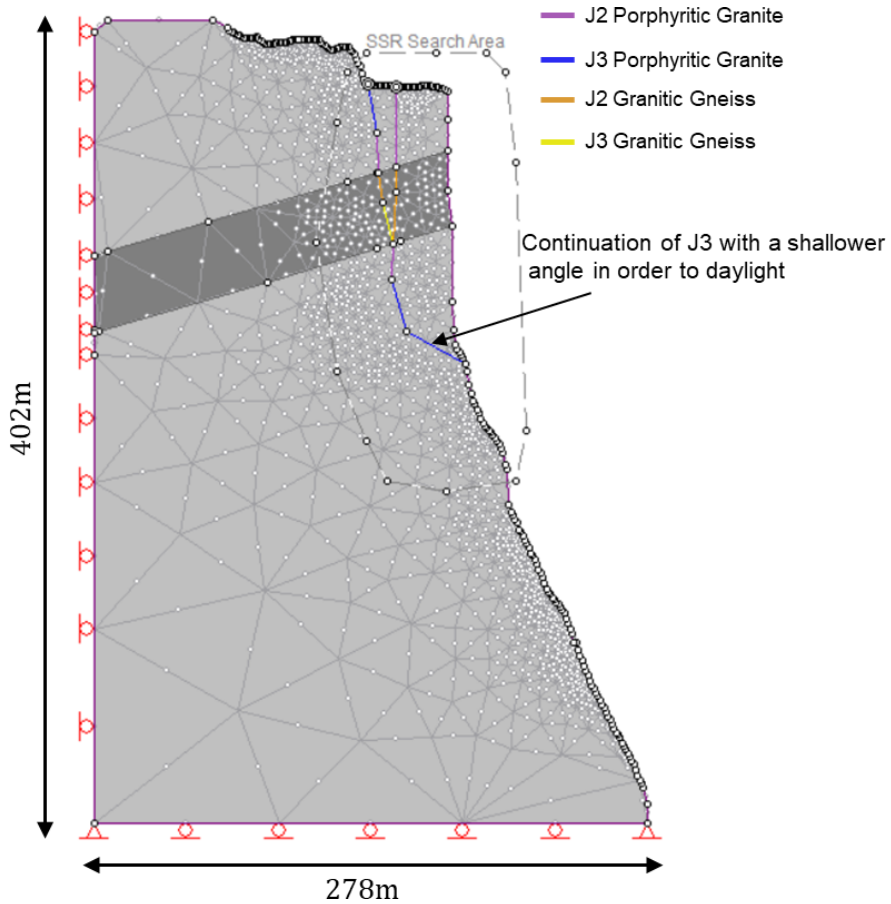
Figure 4.20: The geometry of the model 2a is very similar to model 2. The difference is that the joint set J3 is extended in order to daylight the slope.

4.5.2 Results of the Simulations

The simulation was run for all models presented in the method chapter. Model 1 (figure 4.18) was run as an elastic material with the Hoek-Brown failure criterion, while model 2 (Figure 4.19) and model 2a (Figure 4.20) were run as plastic materials with the Mohr-Coulomb criterion. The only difference between model 2 and 2a is that in model 2a the joint is extended with a shallower degree in order to daylight the slope. The sensitivity of the parameters that were expected to be most important for the stability was investigated in a parameter study.

4.5.3 Stress Anisotropy

The first model was simulated with the Hoek-Brown failure criterion, using an elastic material, as the main goal was to investigate the stress distribution along the slope. The SSR-analysis was not applied to this model. Figure 4.21, displays the differential stress of Model 1 which is the ratio between the major (σ_1) and minor (σ_3) principle stress.
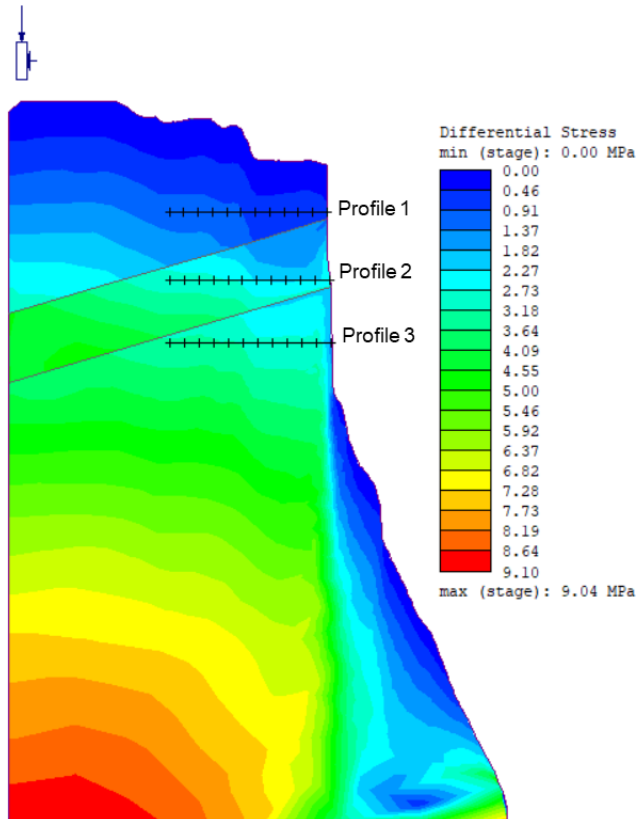
Figure 4.21: Model 1 (elastic material) with contours representing the differential stress (σ_1) / (σ_3). Three profiles are drawn in the model and will be investigated further in figure 4.22.

The model show a increase in differential stress from the top to the lower part of the model. The horizontal stress divided on the vertical stress is approximately 0.3 for both the horizontal stresses. Due to this the anisotropy is expected to increase towards the lower part of the model, as the vertical stress increases, and therefor also the stress anisotropy. However, the increase towards the lower part is not the main focus, as it is not the most important change in stress anisotropy. What is more interesting with the model is the change that occurs along a horizontal profile, as larger changes here are the once that potentially can create tension cracks.

Three profiles were drawn through model 1 as seen in figure 4.21. This was done to get a better visualization of the stress anisotropy in the horizontal direction. The stress ratio along profile 1 to 3, is presented in figure 4.22. All the profiles shows a relatively even ratio, however an abrupt change occurs approximately 55 meters away from the slope face. At this point, the differential stress jumps by a relatively even value, increasing with approximately 0.3. The change is therefor relatively independently on the relative placing of the profile in the vertical direction.

Model 1 has a slight decrease towards 50 meter from the surface, then the ratio increases by 0.32 between approximately 50 and 60 meter from the surface. After this sudden increase, the value continues with a slower increase towards 110 meters from the surface. This pattern is relatively similar for profile 2 and 3 as well. However the decrease from the surface towards 50 meters is less visible in profile 2.
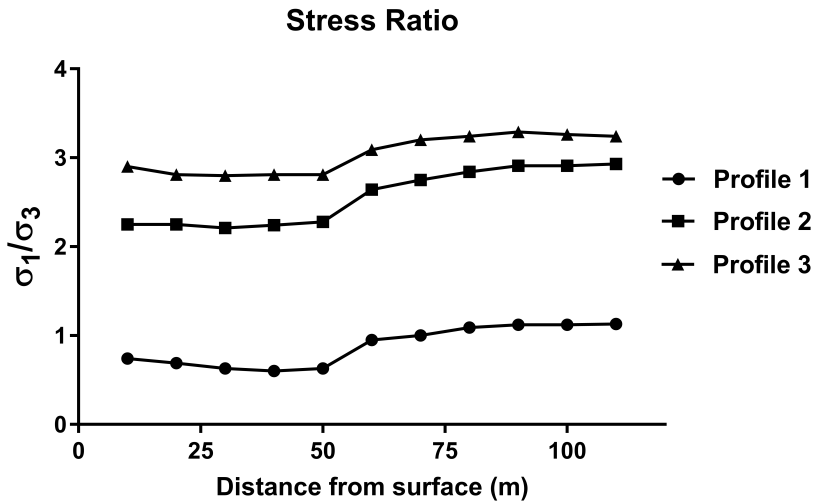
Figure 4.22: The graph based on the profiles in figure 4.21 show how the stress ratio (σ_1/σ_3) change as the distance from the surface increases. At approximately 55 m from the surface, all the graphs show a sudden change in the differential stress.

4.5.4 Maximum Shear Strain

Model 2 was run with the Mohr-Coulomb failure criterion applied, and with a plastic rock material. In this model the SSR-analysis is applied, shown by the dashed grey line. In figure 4.23, the simulation result from model 2 is shown with the maximum shear strain as contour value. The maximum shear strain can give a good indication of the most likely location of the failure plane, hence this contour option was considered useful for the further interpretation.

Two strain concentrations are present at the Critical Stress Reduction Factor (CSRF). One is located along the SSR-boundary, while the other is located below the included joints and is closer to the surface. The CSRF is the maximum value of the SRF whereas the model remains stable Rocscience (2018). The CSRF is therefore similar to the factor of safety (FS). In this case the CSRF is relatively high, with a value of 6.14.

The concentration of the maximum shear strain located furthest into the model 2 is a lot deeper than the joints observed in the field. The failure plane indicated by the concentration below the included joint is seen as a more likely location of a failure plane.
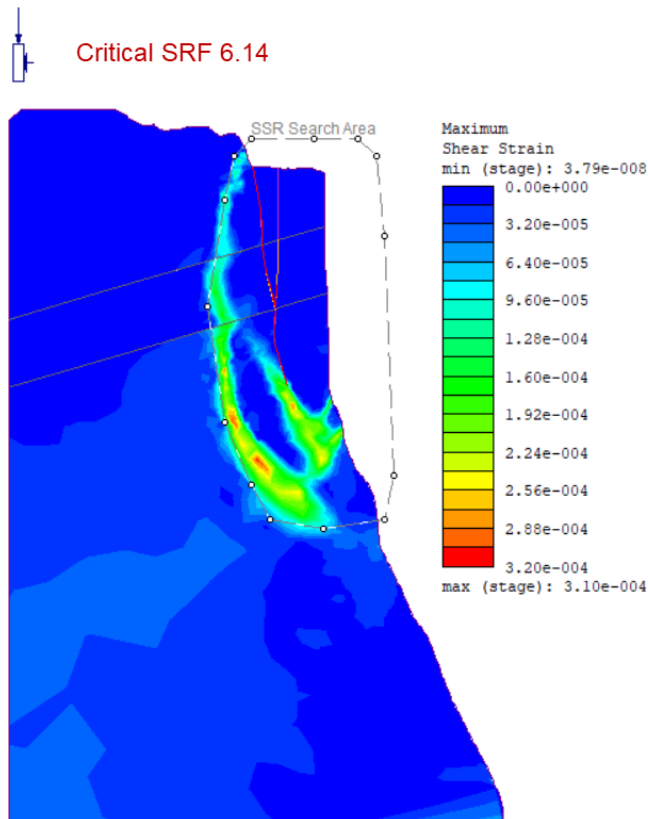
Figure 4.23: Maximum shear strain for model 2 (plastic material), shows two stress concentrations. One is located along the SSR search area, while the other appears below the lowest part of the joint.

Model 2a was run with the same settings as model 2. Figure 4.24 show the result of the simulation with the maximum shear strain as contour value.

The CSRF in model 2a is 4.17, which is a relatively large decrease from 6.14 which is the calculated CSRF in model 2. This reduction is an effect of extending the joint, as all other parameters remained similar for both models. However, even though the joint daylights the slope, a FS of 4.17 is still relatively high, and indicated a stable situation.

When the failure plane is already defined through the extension of the joint, the stress concentration that appeared at the back of the plateau is no longer present. However, a small stress concentration appears beneath the location where the joint daylights the slope. Model 2a indicated that a continuation of the joint will lead to the strain being concentrated along the joint.
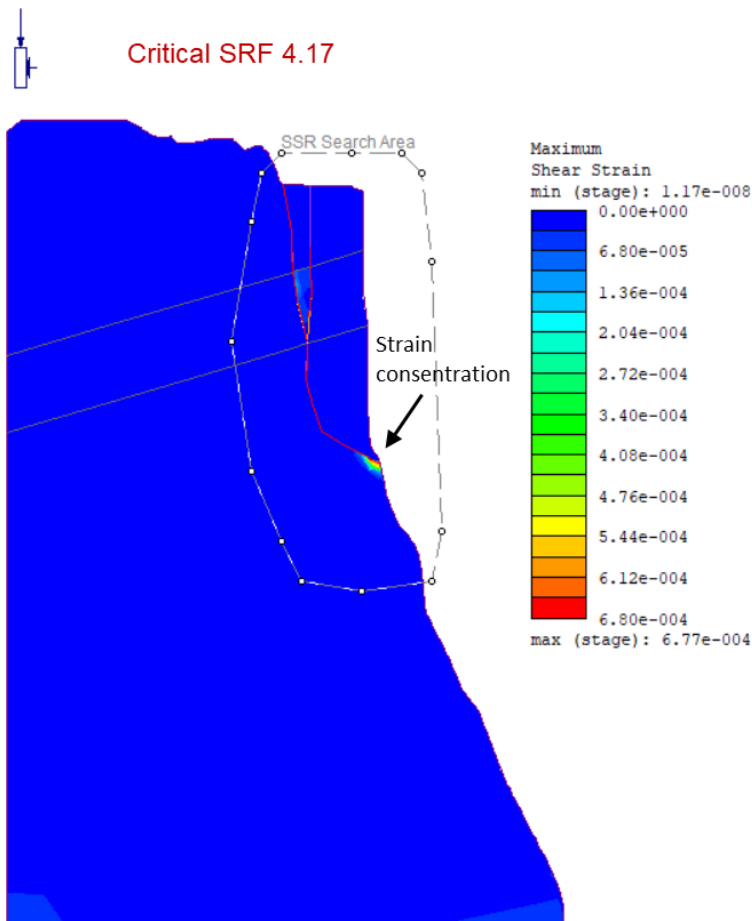
Figure 4.24: Maximum shear strain for model 2a (plastic material) show a very different result than for model 2. In model 2a, the strain concentration was found beneath the joint that daylights the slope.

4.5.5 Total Displacement

In figure 4.25, the total displacement in model 2 is presented. A Concentration of the displacement is seen in the area between the lowest part of the joint, and the slope surface. This area is similar to the potential sliding plane, which was investigated in figure 4.23 The largest displacement recorded is 0.996 cm.

However, the displacement is also relatively high in almost the entire area included in the SSR-analysis. The displacement in the surrounding rock mass outside the SSR search area is low.
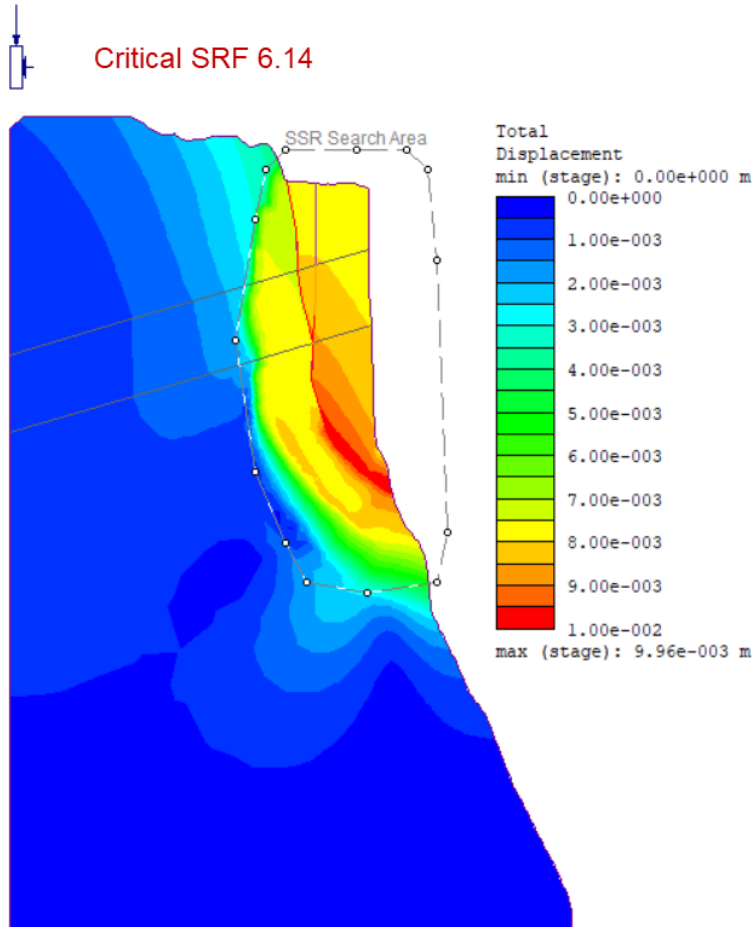
Figure 4.25: The total displacement for model 2 (plastic material) shows displacement both in the block partly detached from the slope, with highest displacement at the foot. There is however also a relatively high displacement in the surrounding rock that is included in the SSR Search Area.

In model 2a the total displacement is almost entirely concentrated in the block that is detached from the slope (Figure 4.26). This was indicated by the analysis of the maximum shear strain in figure 4.24, as the failure plane is now defined prior to the simulation. As no intact rock has to fail prior to sliding, the CSRF is lower, and the displacement is concentrated on the block.

The highest displacement found is along the shallow joint extension, with a maximum value of 6 millimeters. The total deformation then decreases towards the top of the detached block. For the surrounding rock mass outside the joint, the total displacement is minimal.
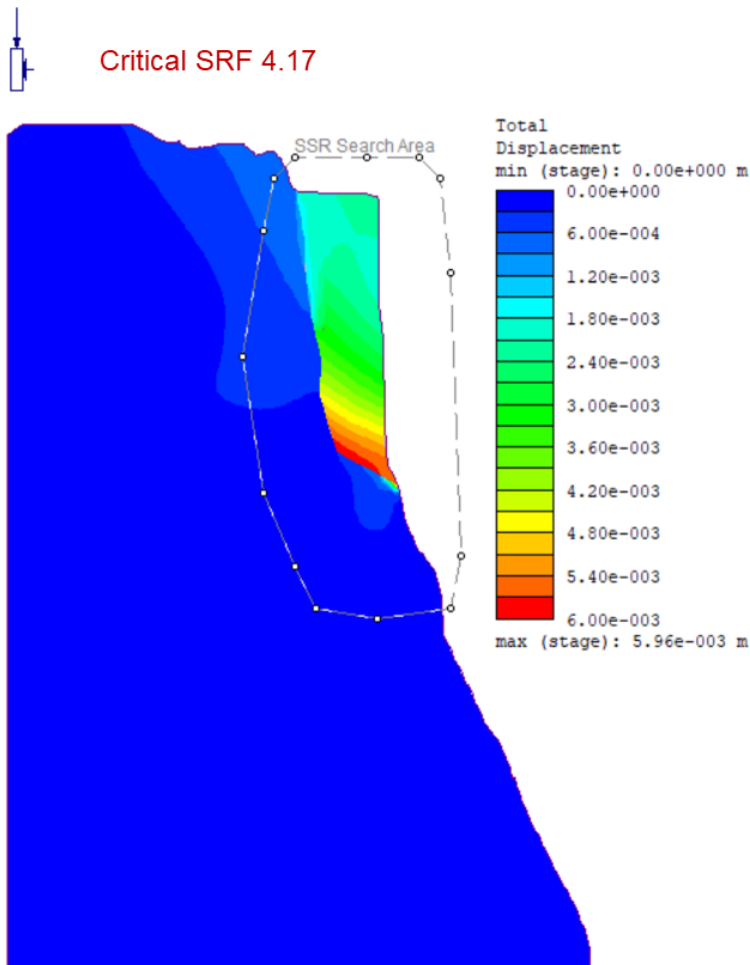
Figure 4.26: The total displacement found in model 2a (plastic material) shows a large displacement in the block that is detached from the slope by the thoroughgoing joint. The max stage is colored in red, and represents movement of up to 6 mm.

4.5.6 Yielded Elements

To get a better understanding of how the rock might fail, figure 4.27 is included. As seen in figure (4.27), that yielded elements appear only at SRF value higher than 1.5. However, the first yielding of the joint appears already at a SRF of 1.1. The circular dots represents tension failure, and mainly appear in the upper part of the slope. At lower elevation in the rock formation, the shear failure is more dominant.

The failure in model 2 is a combination of failure along the joint and shear failure at the bottom of the rock formation. This combination is interpreted to be the one that defined the slide-area. In model 2, the only joint that is yielding is the joint at the back of the plateau. This joint fails in several stages, as explained in detail in figure 4.28.

The joint set J3 is the first to fail, at a SRF value of 1.1, and occurs in both rock masses. This joint set had the lowest JRC measured in the field with a JRC of 10. For comparison joint set J2 has a JRC of 16. As the SRF increases, the joints continue to fail. The whole joint fails before the CSRF is reached, and is yielding at 5.85.
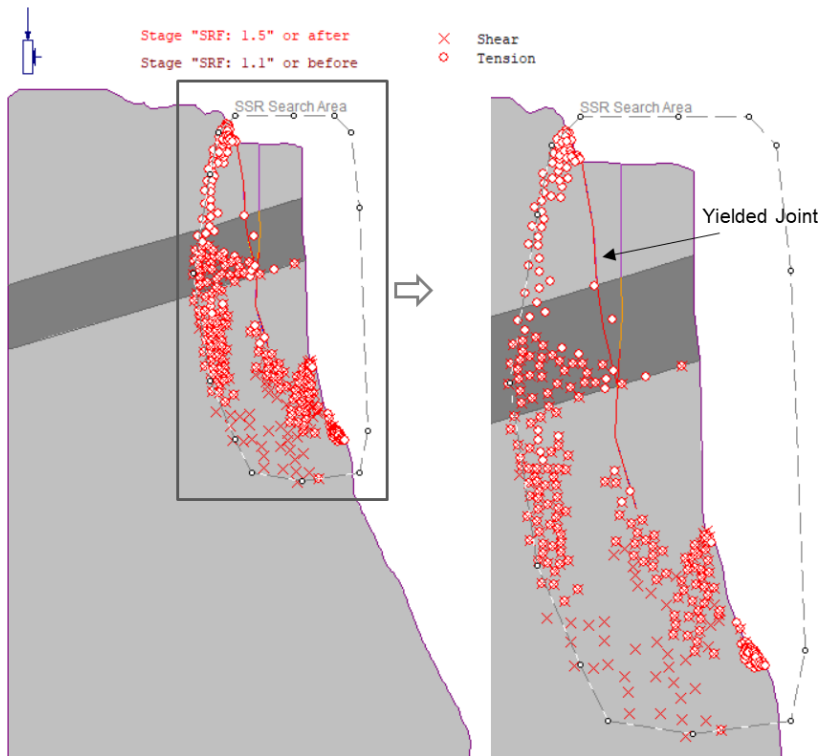
Figure 4.27: Figure showing the yielded elements in model 2 (plastic material). The upper part is dominated by tension failure (red dots), while in the lower part, the failure occur mainly in shear (red crosses). The included joint is fully yielded at the CSRF. All yielded elements appear after the strength reduction factor exceeds 2.1, except the joint, where the first yielding occurs at SRF of 1.1 (Figure 4.28).
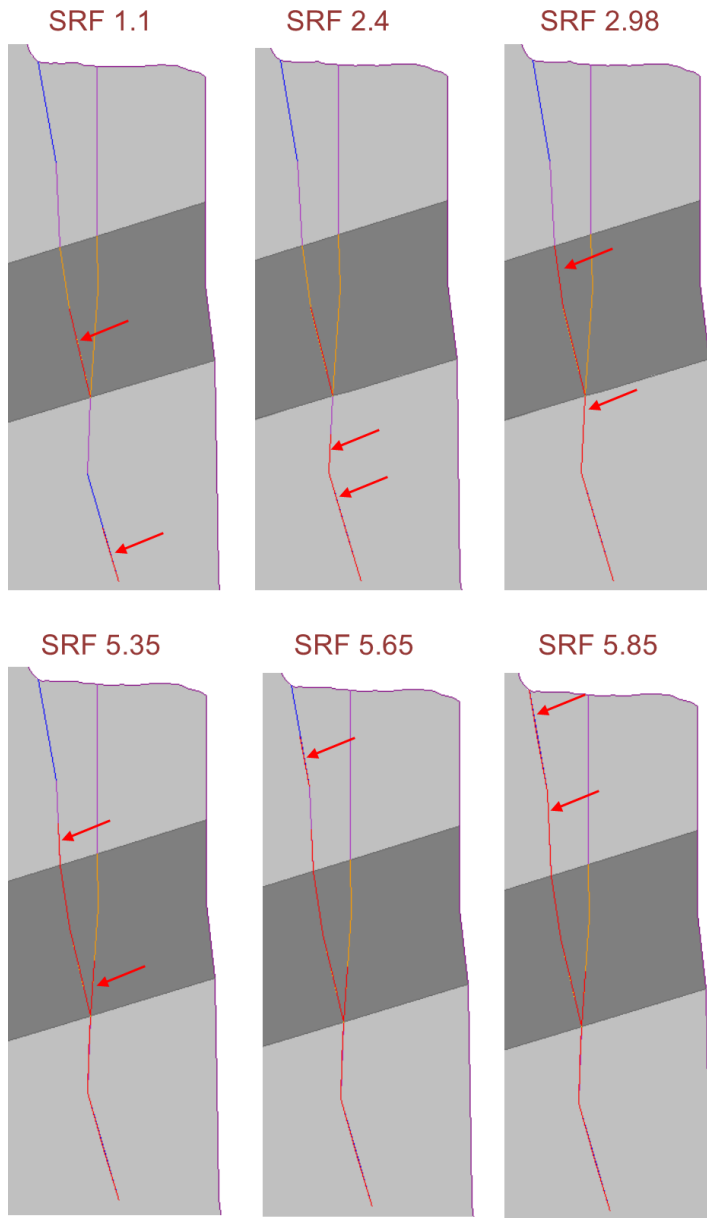
Figure 4.28: The yielding of the join in model 2 (plastic material) shown in several steps. The joints with the most gentle dip (J3) is the first to fail at SRF = 1.1. After this the joint furthest to the left in the granitic gneiss, and the lower part of the porphyritic granite fails when the SRF is 2.98. The whole joint at the back of the plateau has failed at an SRF of 5.85.

4.5.7 Investigation of Parameters

As the input parameters in a numerical analysis are of great importance for the result, several sensitivity tests were carried out by varying the input parameters. However, not all parameters were varied in this study, and this should be kept in mind when evaluating the result. An overview of the test results are given in appendix 2.

Joints

To investigate how the reduction of the joint parameters effect the model, the friction angles for joint set J2 and J3, determined in chapter 3.5.6, were decreased. This was done by decreasing the friction angle by 5%, 10%, 20%, 30% and 50%. Simulations with the reduced friction angle were then run, while the other parameters remained constant.

For model 2, the reduction of the friction angle did not lower the CSRF, as shown in figure 4.29. Based on the changes in the CSRF shown in table 4.3 for model 2, the friction angle of the joints is not considered a sensitive parameter. For model 2a however, reducing the friction angle had a noticeable effect on the CSRF. There is a relatively even decrease in CSRF for model 2a in figure 4.29. At 50% reduction of the friction angle (ϕ_{peak}) the CSRF is 2.96, which decreased by 1.21 from the original value at ϕ_{peak} which is 4.17.

Table 4.3: The friction angle of J2 and J3 was reduced in both the granitic gneiss and the porphyritic granite. The lowest reduction was 50% of ϕ_{peak}.

	Model 2	**Model 2a**
Reduction of ϕ_{peak}	0% - 50 %	0% - 50 %
CSRF	6.14 - 6.25	4.17 - 2.96
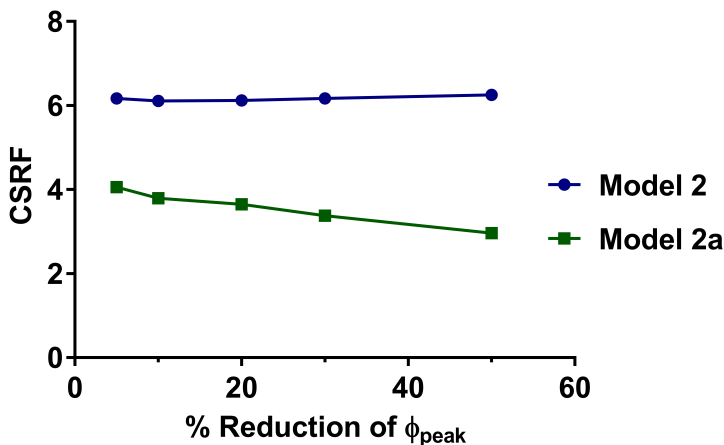
Figure 4.29: The reduction of the friction angle lowered the CSRF more in model 2a than in model 2.

Further, the same analysis was carried out by reducing the cohesion of the joints. The cohesion for all joints in the model was therefore reduced by 5%, 10%, 20%, 30% and 50%, while all other parameters were constant. Both model 2 and model 2a showed a decrease in CSRF when the cohesion was reduced (Figure 4.30).

Model 2 showed almost no reduction in the CSRF between $c_{5\%}$ and $c_{30\%}$. However, between $c_{30\%}$ and $c_{50\%}$ the CSRF dropped from 6.25 to 5.40 (Table 4.4). Model 2a decreased from 4.08 at $c_{5\%}$ to 3.02 at $c_{50\%}$, indicating that the reduction of the friction angle and the cohesion has a very similar effect on model 2a, as the graphs show an almost identical reduction of CSRF.

Table 4.4: Similar to the friction angle, also the cohesion was reduced, to investigate the sensitivity of the parameter.

	Model 2	Model 2a
Reduction of c_{peak}	0% - 50 %	0% - 50 %
CSRF	6.14 - 5.40	4.17 - 3.02
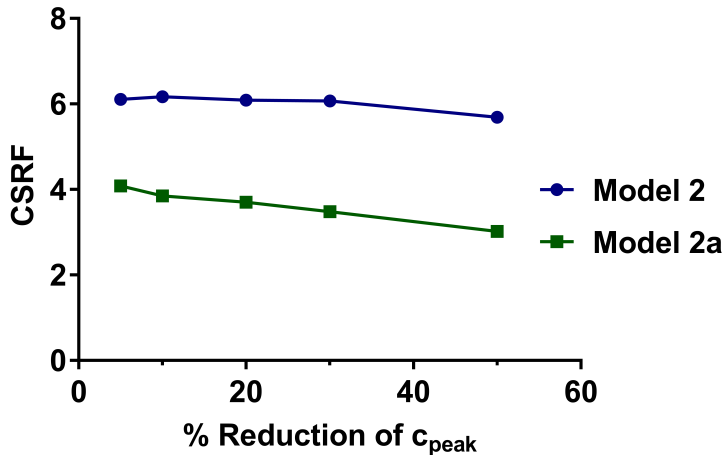
Figure 4.30: Reduction in the cohesion showed a decrease in the CSRF for model 2 and model 2a at 50% of c_peak. However for model 2a there was an increase in CSRF at 30% reduction.

In addition to investigating the cohesion and the friction angle, the joint shear stiffness (K_s) and normal stiffness (K_n) was also reduced by the same percentage as previously used. The results are shown in figure 4.31 for model 2 and model 2a.

Model 2 showed an increase in the CSRF from 5% to 20%. At 30% reduction of the stiffness parameters, the CSRF was higher, than for the same model at 5%. The CSRF then decreased at 30% reduction, and again increased at 50%. Despite the small variations, the CSRF did stay relatively constant for model 2 in all the simulations.

Even though the CSRF in Model 2a, is also relatively constant, there is a more defined

decrease than for model 2 (Table 4.5). The change in the CSRF was only at 0.11, from 4.17 at the peak values, 4.06 at 50% of peak values.

Table 4.5: The reduction in the stiffness parameters showed a small reduction in the CSRF for both models

	Model 2	**Model 2a**
Reduction of K_s and K_n	0% - 50 %	0% - 50 %
CSRF	6.14 - 6.10	4.17 - 4.06
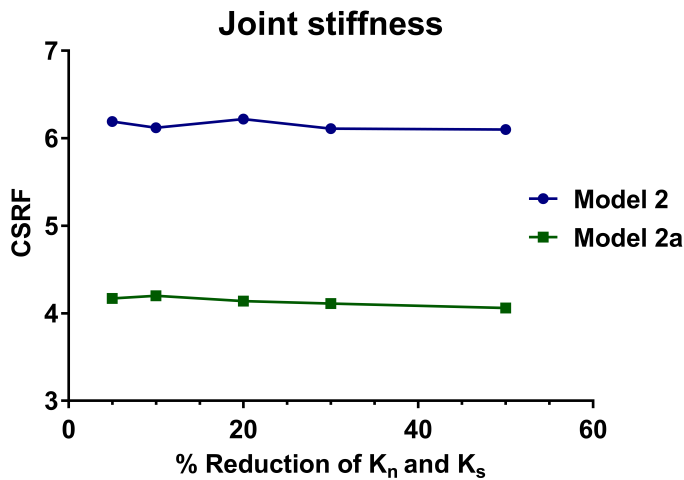
Figure 4.31: Reduction in the joint stiffness parameters, had a very little effect on the CSRF. Even though there was a minor decrease for model 2a, the CSRF shows very little sensitivity to changes in the joint stiffness.

Based on the parameter study of the joints, the biggest reduction of the CSRF in model 2 was the cohesion, which decreased the CSRF by 0.85, from 6.14 at c_{peak} to 5.69 at $c_{50\%}$. A small decrease from the peak joint stiffness to a 50% reduced joint stiffness also occurred, however, this was only a reduction of 0.04. The lowering of the friction angle to 50% of the peak value did not decrease the CSRF. Based on these results, model 2 seems to be most sensitive to a reduction in the cohesion, when investigating the joint parameters.

Model 2a was effected to a relatively large extent both by the reduction of the friction angle and the cohesion. The value at $\phi_{50\%}$ was the lowest obtained CSRF, at 2.96. The reduction from ϕ_{peak} at 4.17 was therefore at 1.21. From c_{peak} to $c_{50\%}$ the reduction was at 1.15, from 4.17 to 3.02. Unlike the two already mentioned values, the reduction in the stiffness parameters by 50%, only reduced the CSRF by 0.11. Both the cohesion and the friction angle are, based on the mentioned observations, interpreted the most sensitive parameters.

Stress-ratio

As the in-situ stress conditions can have a large effect of the slope stability, the ratio between the horizontal stress and vertical stress was tested. The out-of-plane ratio (σ_h/σ_v) and the in plane ratio (σ_H/σ_v) were investigated one at the time, while the other were held stable at the original value. The original ratio obtained from Hanssen (1998) was at 0.282 out-of-plane (σ_h/σ_v) and 0.296 in plane (σ_H/σ_v).

As the horizontal stress directed parallel to the model is interpreted to not have the potential of being very high, the ratio σ_H/σ_v was only run for values between 0.1 and 0.5. The ration out-of-plane however, can potentially be significantly higher, as it is oriented normal to the slope profile. Both models were therefore run for σ_h/σ_v values from 0.2 to 2.0.

The CSRF obtained when varying the in plane stress ratio is shown in figure 4.32. For model 2, the CSRF is highest when the ratio is 0.5. However there were no big differences from the values 0.1 to 0.5. The absolute lowest value for model 2 was 6.13, obtained when $\sigma_H/\sigma_v = 0.2$. The highest CSRF at $\sigma_H/\sigma_v = 0.5$ was 6.25.

For model 2a, the CSRF is highest when the ratio is set to 0.5, and lowest at 0.1. When σ_H/σ_v is set to 0.2, 0.3 and 0.4 there is almost no change in the CSRF, which was also seen in model 2.

The variation of the in plane stress ratio is therefore not unambiguous, as the result was different for both models. However, it seems that for both models, the σ_H/σ_v of 0.5 gives the highest CSRF. Based on the simulations, it seems like model 2a is slightly more sensitive to changes in the in-plane stress ratio.
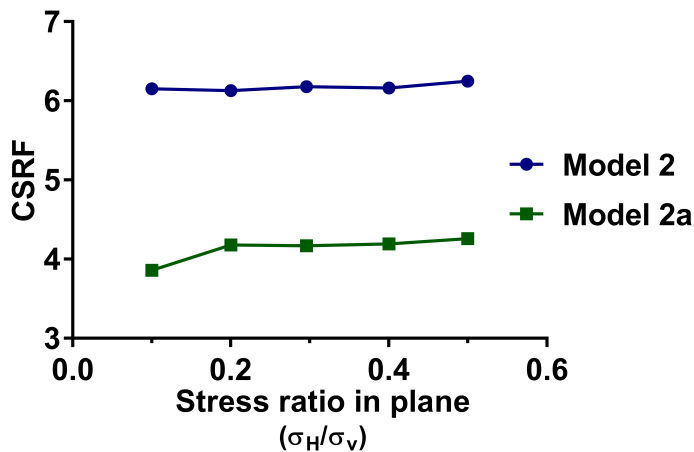
Figure 4.32: Figure showing the results of varying the stress ratio in plane (σ_H/σ_v) from 0.1 to 0.5. Both for model 2 and model 2a, the highest CSRF occurs when the ratio is 0.5. The lowest CSRF for the models was found at 0.2 for model 2, and 0.1 for model 2a.

The variations done for the out-of-plane stress ratio (σ_h/σ_v) and the obtained CSRF are presented in figure 4.33. Similar to the in plane stress measurements, the results were also in this case different for the two models.

Model 2 again showed a highest CSRF when the out-of-plane stress ratio was low. For the out-of-plane stress ratio of 0.2, 0.282 and 0.4 the ratio was almost identical, and the CSRF ranged between 6.14 to 6.17. When the ratio was increased to 0.6, 0.8 and 1, the CSRF dropped and ranged between 6.10 to 6.11 for the three simulations. However, when the ratio was increased 2, the CSRF fell to 5.92.

The CSRF in model 2a was less influenced by the changes in the out-of-plane stress ratio. The lowest value of 4.14 was found when the ratio was 0.2 and 0.6. When the stress ratio was increased to 0.8, 1 and 2, the CSRF increased slightly. The behaviour with the increasing CSRF for the high stress ratio is therefore opposite in model 2a than for model 2, which had a lower CSRF for high stress ratios.
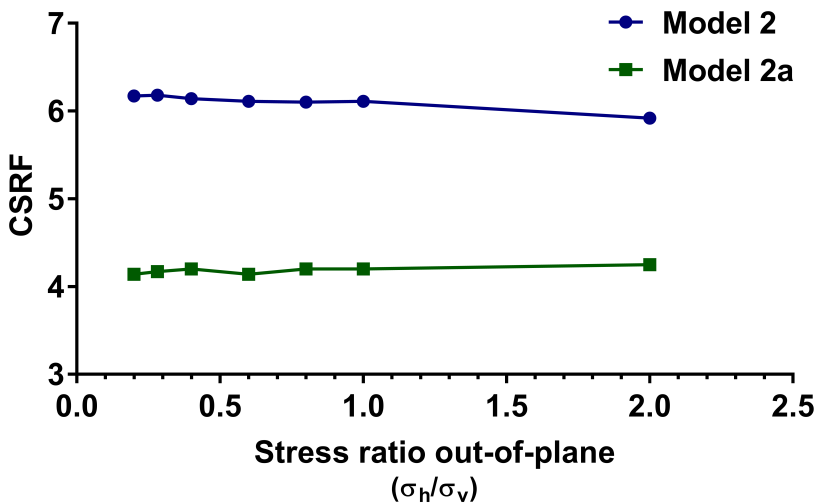
Figure 4.33: Figure showing the results obtained by varying the out-of-plane stress ratio. Model 2 had the highest CSRF when the ratio was low. However, the CSRF decreased for model 2, when the ratio was increased to 2. For model 2a, on the other hand, the CSRF increased when the ratio was high, showing an opposite behaviour than model 2.

Based on the presented data in figure 4.32 and figure 4.33 both models are not effected to a large degree by the changes in the in plane and out-of-plane stress ratios. In the investigation of the out-of-plane stress ratio (σ_h/σ_v), the models behaved in an opposite manner. For the in plane stress ratio (σ_H/σ_v), both models increased in CSRF when the ratio was high. Generally, the changes in the in plane ratio had a larger effect on the CSRF than changes in the out-of-plane stress ratio, especially on model 2a.

4.6 Hazard and Risk Classification

The risk analysis was carried out as described in chapter 2.1.3, following the work flow produced by NGU. Basically, nine criteria are given a score based on the structural settings, geomorphology and the activity/deformation. The analysis was carried out for both defined scenarios (scenario A and scenario B). As no accurate displacement measurements exist at Preikestolen, the matrix in figure 4.34 (scenario A) and figure 4.35 (scenario B) have a high uncertainty. The tables produced for both scenario A and scenario B are can be found in appendix 3.

Both scenarios have a defined back scarp, however, it is only fully developed for scenario B. In scenario A, the back scarp is only partly open. This is the main difference for the two scenarios, as all the other factors are almost identical.

Both scenarios have fully developed lateral release surfaces on both sides, and failure is kinematically possible (as previously explained). Furthermore no lower boundary or a developed sliding surface were observed. However, due to the risk of toppling, an uncertainty was included in the score given by the morphological expression of the rupture surface.

Other than the mentioned factors, the score of the hazard classification is based on past events, deformation and activity. A few measurements exist for the back-scarp in scenario B. However, these measurements are not very precise, and smaller movements could have been overlooked. Furthermore, no acceleration measurements, bathymetric data or displacement rates are available for the slope. Thus the uncertainty of the hazard score will be relatively high.

Prior to the risk analysis, a quick estimate of the possible displacement wave was carried out by NGU. The estimate showed a maximum run-up of 6 m on the opposite side of the fjord from Preikestolen, and a rather quick decrease in wave-height further out in the fjord. However, this estimate is very approximately, and more precise estimations should be followed up to delimit the uncertainties. As the estimations showed a low run up, no life are interpreted to be threatened by the possible displacement wave.

The main risk was therefore interpreted to be connected to the amount of humans located at the plateau during a failure. The number of visitors at Preikestolen has been up to 250 000 each year. This accounts for almost 700 visitors on average each day. For both scenarios, the average value of potential life losses was set to 100, placing both scenario A and scenario B in the light red part of the risk matrix (moderate risk).

Both scenarios show relatively similar result and are within the medium to low hazard class. However the consequences are highly variable, especially since no detailed analyses of the secondary effects are done. The input for both models was also relatively similar, however, the joint in scenario A, is not fully developed. The joint in scenario B, is crossing the whole plateau and is thus fully developed, resulting in a higher score on the y-axis.

However these risk matrix show a large uncertainty, mainly as three of the sections are given points based on the deformation. As no deformation measurements is yet available from Preikestolen, this was given a high uncertainty number in the calculation. To delimit the uncertainties, deformations measurements should be included in the evaluation when they are available. The large span in the uncertainties when it comes to the consequences is however hard to narrow down. A more detailed analysis of the possible displacement wave is however recommended.
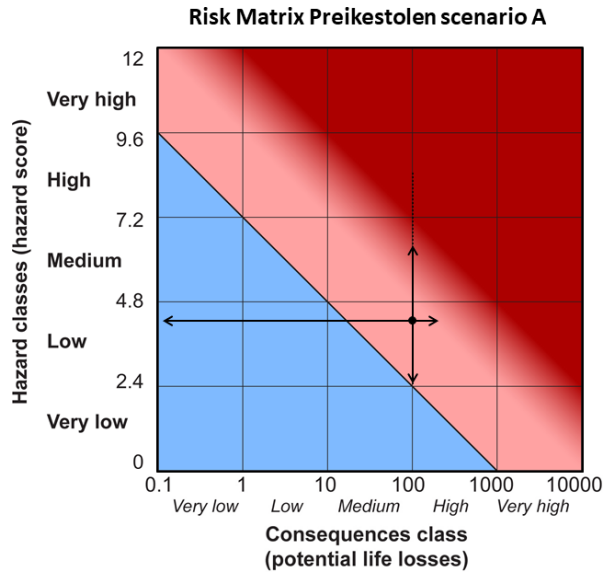
Figure 4.34: Risk matrix for scenario A, which is the largest scenario. A large uncertain is applied due to the huge variation of potential life losses, as this is highly variable. The hazard class is also uncertain, as no measurements of deformation exist.
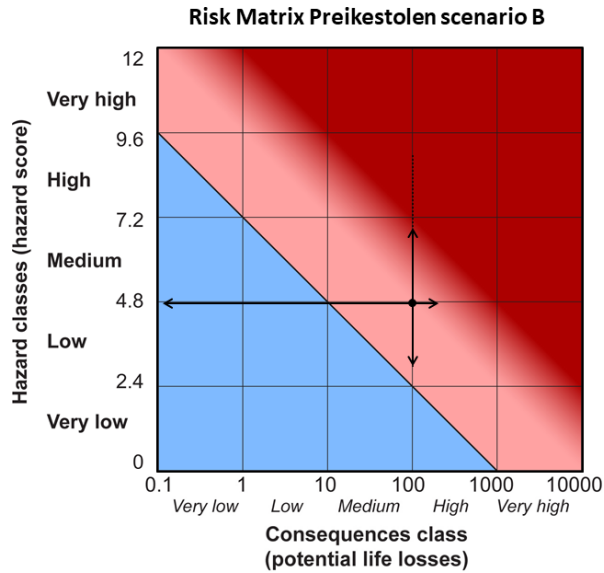
Figure 4.35: Risk matrix for scenario B, which has the smallest volume. The hazard class is slightly higher in scenario B, than for scenario A. However, the same uncertainties as previously mentioned for scenario A, also applies for scenario B.

Chapter 5

Discussion

5.1 Evaluation of 3D Models

In this chapter, the evaluation of the 3D models created will be discussed based on expectations, the result of the comparisons and published literature. First, the techniques will be discussed by themselves, followed by a more throughout comparison of photogrammetry versus LiDAR. The models were used for the purpose of gathering geological observations and measurements, and this has effected the evaluation of the models. The models were evaluated mainly based on how they perform in connection with a geological study.

Both the SLR 1, Drone and LiDAR model were used to identify the extension of the joints along the plateau. The only model that was not directly used in the investigation is the SLR 2 model. For extraction of structural measurements, the SLR 1 and the LiDAR models were used.

Several reasons for not using the SLR 2 model appeared during the evaluation of the model. When the cloud to cloud distance was compared between the SLR 2 model to both the drone and the LiDAR point cloud, it became especially evident that the SLR 2 model had several issues. The reasons for the unsatisfying result of the georeferencing will be discussed in more detail in chapter 5.1.2.

The quality of the georeferencing of the point clouds was variable, as presented in chapter 4.2.1. To include an overview of the comparisons, a summary of the cloud to cloud distances from the comparisons is presented in figure 5.1. These graphs show an even spread of errors along figure 5.1 a and b, while the graphs in figure 5.1 c, d and e, which contains the LiDAR data, show a more uneven curve.

The drone model and the SLR 1 model are very similar. The distance between the two clouds is generally low, and large parts of the cloud to cloud distances are less than 0.15 m (Figure 5.1 a). The models does however distinguish from each other towards the bottom of the point-clouds. As the SLR 1 model has a very consistent point spacing throughout the model, the drone point cloud have a significantly larger spacing between the points towards the lower elevations.
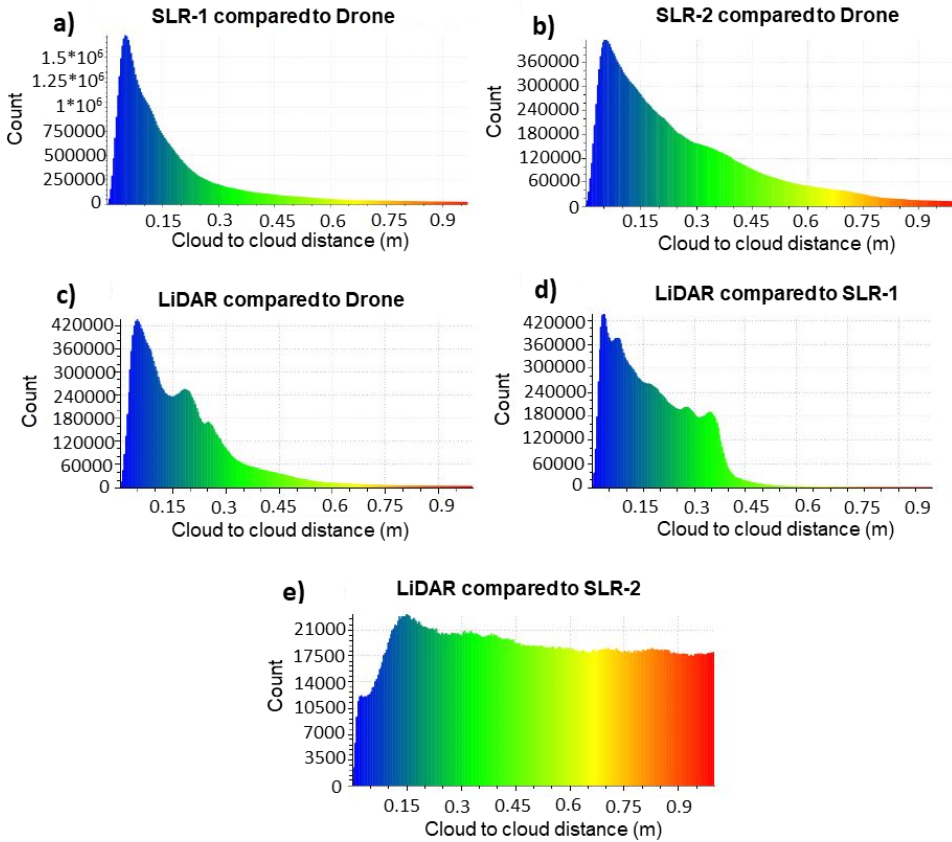
Figure 5.1: Overview of the five comparisons of the 3D models. Only areas where point spacing is below 1 meter are included in the graphs. a) The SLR 1 model compared to the drone model.; b) The SLR 2 model compared to the drone model.; c) The LiDAR model compared to the drone model.; d) The LiDAR model compared to the SLR 1 model.; e) The LiDAR model compared to the SLR 2 model.

The error due to the low drone quality in the lower part, was visible in several of the other comparisons (Figure 5.2 d.). However, this could also have been effected by the low point density of the LiDAR data in the area. Both factors are interpreted to have effected the low quality towards the lower elevations of the model. In the comparison between the drone and the LiDAR model, the top plateau had a distance of approximately 0.2 m between the two point clouds (Figure 5.2 b.). The best match is however at the sides if Preikestolen, where the main cloud to cloud distance measured is approximately 5 cm (Figure 5.2 c).
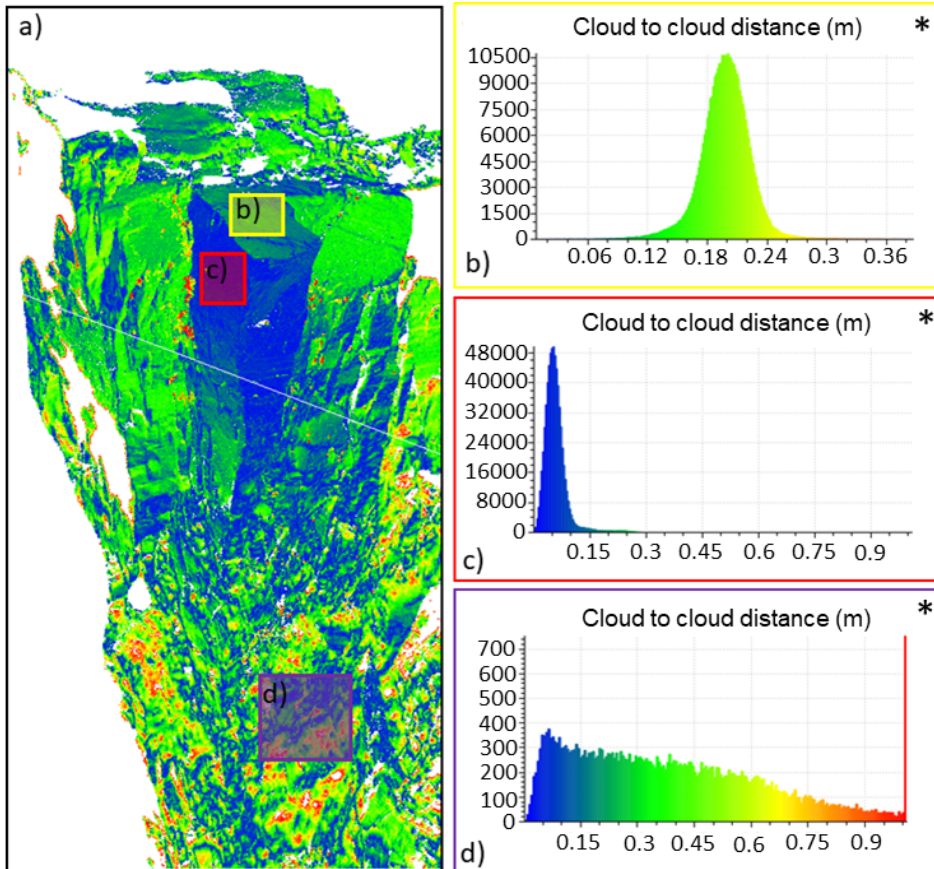
Figure 5.2: Cloud to cloud distances between the drone and the LiDAR point cloud. a) Overview of the detailed compared areas.; b) Distances at the top plateau.; c) Distances measured at the side of the plateau.; d) Distances measured at the lower part.

In the comparison of the SLR 1 point cloud and the LiDAR point cloud (Figure 5.3), the quality of the lower part of the model (Figure 5.3 d) was relatively good compared to figure 5.2. This support the assumption that the helicopter model is better towards the lower elevations of the model compared to the drone model, and that the error is not only an effect of the relatively large point spacing in the LiDAR model. The match between the SLR 1 and the LiDAR point cloud at the Preikestolen plateau, is very good, and the main distance is approximately 3-4 cm (Figure 5.3 b). The point distances along the steep side of Preikestolen are approximately 15 cm.
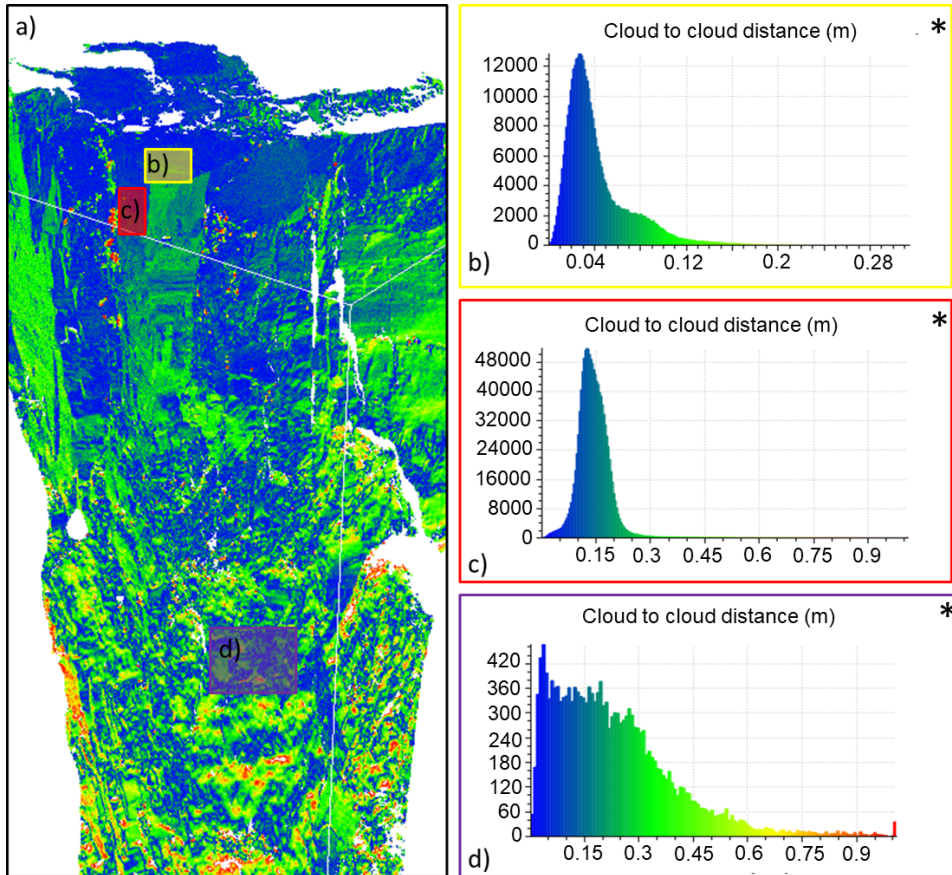
Figure 5.3: Cloud to cloud distances between the SLR 1 and the LiDAR point cloud. a) Overview of the measured areas.; b) Parts of the top cover is less accurate.; c) The sides of Preikestolen is a good match, however, slightly poorer than for the top surface.; d) The lower part shows that the cloud to cloud distances are large in the area.

5.1.1 Drone

One of the main advantages with the drone was expected to be the accessibility in the field. In the study from Eisenbeiß (2009), the use of Unmanned Aerial Vehicles (UAV), like drones, in (among others) high risk situations and inaccessible areas is mentioned as a major advantage. However at Preikestolen, the accessibility in the field was one of the main challenges. Due to the steep plateau, it was decided not to fly the drone too far down along the slope. Hence the model was based on photos taken from high up on the rock formation, and above the plateau. Therefore the model was very good in the upper part, with decreasing quality towards the fjord. The vegetation was also an issue with the drone model, which will be further described in section 5.1.4, as it applies for all models made with the SfM method.

An advantage with the drone was however the ability to define the route with pre-programmed way points. This secures an even coverage of the pictures and makes the fieldwork more efficient. Having an georeferenced model after processing, was also evaluated as an advantage, especially if only one model would have been used. For the case at Preikestolen, the georeferencing would have been a major challenge without the drone model. This is mainly due to the lack of high quality terrain data in the area, as only a 10 m DEM was available during the study. However, as large parts of Norway are soon expected to be covered with a higher quality 1m DEM from airborne LiDAR scanning, the lack of high quality terrain-data is not expected to be a problem for much longer.

Another advantage with the drone, is the low cost. Drones are relatively inexpensive and have a low operating cost compared to manned air crafts (Eisenbeiß, 2009). As all the processing tools that were used are freely available, the cost is almost entirely dependent on the price of the drone and the camera attached. However, the processing of the huge amount of data, requires a large computer capacity and can be extremely time consuming. How time consuming the computation will be is however dependent on the size of the investigated area. The computation time is highlighted by Shahbazi et al. (2015), which states that efficient data processing is one of the factors that still requires further investigations.

5.1.2 SLR

A large variation in the quality of the two SLR models was early noticed. The SLR 1 model was evaluated to be of very high quality, and the point density was both high and even throughout the model. The SLR 2 model on the other hand, was not as good. For the SLR 2 model, the point density was lower and not as even as in the SLR 1 model. Furthermore, the cloud to cloud measurements carried out after the georeferencing indicated that there was a problem with the SLR 2 point cloud, as shown in chapter 4.2.1. The best model (SLR 1) was created from photos taken at 9 a.m., in acceptable light conditions. The SLR 2 model is based on photos taken at 5 p.m., where the light conditions were poorer. Furthermore, it was discovered that the settings of the camera were not optimal during the photographing for the SLR 2 model.

Even though the SLR 1 model was of high quality, and the point density seemed to be even throughout the model, the vegetated areas are of poorer quality. This can be seen in the comparison between the SLR 1 model and the LiDAR model (Figure 5.3). The study

from Nicolet (2017), supports the statement that SfM photogrammetry is most appropriate in areas lacking vegetation. Thus the result from the top of Preikestolen showed very good results, while the vegetated areas had larger holes, which were especially evident in the comparisons of the cloud to cloud distances.

A major issue with the SLR 2 model, was the poor quality of the photos. Poor light conditions combined with wrong camera settings resulted in too long exposure times and blurred images. As a short exposure time will reduce blur in pictures (Raskar et al., 2006), the long exposure time during the photographing is interpreted to lower the quality of the photos, and making then more blurry. Thus it is difficult to distinguish to what extent the settings and the light conditions have effected the quality of the photos. Therefore no evaluation of how sensitive the quality of the SLR 1 and SLR 2 models were to light conditions was made.

Even though it is hard to distinguish between the error applied by each factor, both are interpreted to lower the photo quality. This is supported by the study from Nicolet (2017) which mentions variation in light condition as one of the drawbacks for SfM modeling. Light conditions are interpreted to have a large effect on the quality of the photos, and hence the quality of the photogrammetry model. According to Raczynski (2017) the lighting will effect the photos in several ways, as sunny conditions will produce good visibility but also shadows, and cloudy conditions can produce a uniformly exposed terrain that can also be pale. Hence, a compromise between the mentioned factors should be made to capture photos of high quality (Raczynski, 2017).

With some easy adjustments prior to the fieldwork, the quality of the SLR 2 model might have been significantly improved. Checking the camera setting prior to photographing could have drastically enhanced the quality of the SLR 2 model, which further could have lead to a more precise indication of how the light conditions effected the model.

5.1.3   LiDAR

The quality of the LiDAR model was evaluated as relatively good as previously explained, and the model was used in Coltop 3D to gather structural measurements. For the definition of the structures and their extent, the LiDAR point cloud was also very convenient, as it made it easy to follow the extension of the various joints.

As was shown in chapter 4.2, a large variation in the point density is present in this model. This was expected, as the point density of the scan is dependent on the distance from the scanner and the scanned object. The point density was very good for the scans directed towards the NE and SE. These scans were taken with a short distance between the scanner and Preikestolen, resulting in point spacing's of 2.5 cm and 2 cm. As the scan position at the opposite side of the fjord was more than 2000 m apart from the scan object, the point spacing in this scan was poor, at approximately 20 cm.

As presented in chapter 3.2.2 the scanner used in this project (Optech ILRIS-3D LR) has a theoretical range of 3000 m with a reflectively of 80% (Optech, 2018). The range of the scanner is to a large extent affected by the reflectivity of the target (Buckley et al., 2008). However, bare rock surfaces often have good reflecting properties, and can provide a return of up to 75% (Wehr and Lohr, 1999; Buckley et al., 2008). The scan from 2000 m distance resulted in a point spacing of approximately 20 cm.

Since the structures mapped at Preikestolen generally have a relatively large extent they are still visible on the scans. However, it was more convenient to use the more even point cloud of the SLR 1 model, instead of the LiDAR point cloud for the areas that were not covered with the more closer scans. Using a point cloud with a low point spacing reduced the risk of missing structures when imported to Coltop 3D. Even though the part of the model scanned from a 2000 m distance had a low point density, it was very helpful during the processing of the scans. Thus it was used as a basis for matching the closer scans, as it had shared surfaces with several of them.

As previously mentioned, several problems with the LiDAR model from Preikestolen became clear during the processing of the scans. The problem was connected to the poor overlap between the scans. The poor overlap especially applied for the scan of the top plateau, which had very few reference points in the other scans. In Buckley et al. (2008), the importance of ensuring suitable levels of overlap is highlighted. Approximately 10 % overlap is needed (Bellian et al., 2005; Buckley et al., 2008).

This issue could have been avoided with a more throughout planning of the scanning positions prior to fieldwork. For example, an additional scan could have been included covering both the top plateau, and one part of the steep sides of Preikestolen. Planning of the survey is highlighted by Sturzenegger and Stead (2009) as an extremely important aspect when remote sensing techniques are used for characterization of rock slopes.

5.1.4 Photogrammetry VS LiDAR

At Preikestolen photogrammetry has been evaluated as a very good model for the slope. This is mainly due to the lack of vegetation. However, some of the lower parts are vegetated. The georeferenced models all show a large discrepancy in the areas that are vegetated. According to Nicolet (2017) the presence of even sparse vegetation can cause problems when using the SfM technique (Figure 5.4).

However, at Preikestolen, the main reason for the poor quality of the drone model in the lower areas was interpreted as a combination of low photo cover and vegetation. Hence there were several factors that effected the quality. The SLR 1 model has a better coverage all over the slope, since the accessibility was much higher. However this model also showed some holes when compared to the LiDAR model. Therefore the vegetation is interpreted to have effected all the photogrammetry models.

The high point spacing of the LiDAR model for the scan taken at a long distance from the slope, is a factor that could have influenced the comparisons between the photogrammetry models and the LiDAR model. Since the cloud to cloud distance measures the distance between the points in the two models, the large point spacing might have accompanied a larger spacing that was expected. Computing the cloud to cloud distance between the photogrammetry models and a LiDAR mesh would probably remove the additional distances induced by the large point spacing.

The following advantages (+) and disadvantages (-) can be summarized for photogrammetry as mentioned in the study from Nicolet (2017) and references therein.

+ Low-cost technique

+ Can be performed with standard field equipment
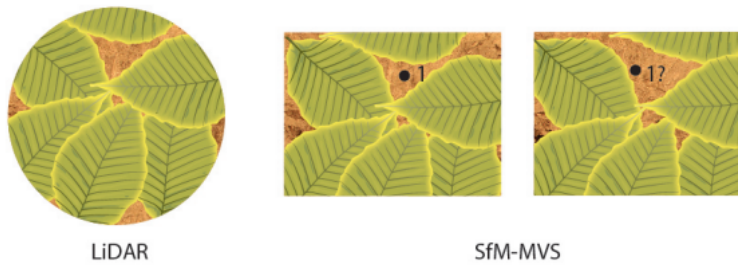
Figure 5.4: Example of how the problem with vegetation arise when using SfM. Point nr. 1 is identified on the left picture of the SfM-MVS, however it is hard to identify on the right picture. Figure from (Nicolet, 2017).

+ High portability (camera can be carried by drone or in a helicopter)

+ Allow for working with multiple scales

− Not error free

− Challenge with vegetated areas

− Variations due to light conditions

− Parameters like precision and point density are harder to control

The majority of the mentioned factors are in line with the ones experienced in this study. The disadvantage concerning the light conditions was interpreted as one of the factors that lowered the overall quality of the SLR 2 model. The vegetation lowered the quality for both models. In addition the following factors were seen as a huge advantage for using photogrammetry during this study.

+ Possibility of having a finished georeference model after processing of the model (Drone)

+ High point density throughout the model (except for the Drone-model)

The advantage of having the drone model that was already georeferenced became especially evident due to the lack of a high quality 1 m DEM in the area. As the remaining models were georeferenced to the drone model, it made the task a lot faster, as this could easily be done in CloudCompare. However, the georeferencing issue also could have been solved with high quality GPS coordinates from the field in combination with the 10 m DEM. Thus this would have required more work, and would have made the work flow significantly less efficient.

Furthermore, the list below shows some of the advantages with using the LiDAR as remote sensing method that was experienced during this thesis.

+ Parameters like point density were known during the scan

+ High resolution, with point spacing's of 2 and 2.5 cm for the closest scans

 – Lower portability in the field

 – Variations in point density due to different distance

In addition to the mentioned factors, several advantages and disadvantages with using LiDAR for structural mapping are given in literature. The study from Jaboyedoff et al. (2012) mentions some of the main advantages with the TLS technique as fast data acquisition, easy portability and setup, in addition to high resolution. Even though the latter statement was true for the investigation at Preikestolen, the factors like easy portability and easy set up were not seen as major advantages. Compared to the photogrammetry, the setup and transportation of the LiDAR scanner was a time demanding process. The LiDAR equipment is relatively heavy, and transportation without a helicopter would have been difficult. The lack of accessible ground is mentioned in Obanawa and Hayakawa (2015) as one limitation with TLS, an this was also experienced at Preikestolen, with very few scanning positions possible on the opposite side of the fjord.

The article from Jaboyedoff et al. (2012) also highlights several disadvantages with the use of a ground based LiDAR scanner. Among these are existence of shadows caused by large variations in the topography. Furthermore Jaboyedoff et al. (2012) mentions an extensive post-processing especially when large areas are scanned, including filtering and alignments of the data sets.

Another factor that was seen during the mapping of structures, is that the LiDAR model is slightly more objective than the models from the photogrammetry. As the photogrammetry models were colored, the evaluation of the extension of the structures was slightly more subjective. The point cloud based on the LiDAR scans however, is grey-toned, and gives a more objective interpretation. However, the option of using an external calibrated SLR with the LiDAR scanner exists.

Lastly, three of the models were evaluated as good enough to carry out structural measurements on. This was the SLR 1, drone, and LiDAR model. However, only the SLR 1 and LiDAR model were used for this purpose. Even though the quality of the drone model was not as good at the lower elevations in the model, it could have worked for measuring in locations higher up. Measurements in the drone model on the lower parts of the slope may result in inaccurate data. To summarize, all the remote sensing techniques worked well for gathering structural measurements. However, care must be taken when evaluating the quality of the model.

To evaluate which technique that is best suited for structural mapping in landslide studies, is challenging, as it will depend on the study site. For remote areas where LiDAR scanner can not be used, photogrammetry with either drone or helicopter would be most suitable. In vegetated areas, photogrammetry is considered inappropriate, and LiDAR scanning is preferable. However, when using a terrestrial LiDAR scanner heavily vegetated areas can cause problems. A huge advantage of the photogrammetry with drone is the low price, and the possibility of planning the route prior to the fieldwork. Furthermore drone surveys will be weather dependent. Therefore, prior to the fieldwork, the site should be evaluated based on several factors, like exposure to wind, expected light conditions (time of the day or weather), vegetation, appropriate scan positions (LiDAR) among others.

5.2 Evaluation of the Numerical Model

In this chapter the numerical model of Preikestolen will be discussed with the focus on the quality of the input, and the interpretation of the result. As the quality of the numerical model will be highly dependent on the quality of the input parameters, these were investigated in a parameter study. However, even though the effect of several of the important parameters are investigated, not all parameters are included. The parameter study was focused on the joint parameters, hence an additional study of the rock parameters are lacking. Hence several uncertainties still exists.

The numerical simulation done at Preikestolen, generally shows a stable situation, as the CSRF and thus the factor of safety, is high. An extension of the joint (model 2a) out towards the slope face, did decrease the safety from 6.14 to 4.17. However, the situation was still stable.

It is important to keep in mind that a numerical model is a simplification of the actual situation, and requires idealization. Therefor not all details and changes within the rock mass can be included into the model. As described in Wyllie and Mah (2004) rock is a unpredictable material, as the behaviour of rock masses is effected by several uncertain factors. Numerical simulation can be used as a tool to reduce the uncertainties, but does not provide the full answer.

5.2.1 Using a 2D Software and the Quality of the Profile

Using a 2D software like RS^2 has some limitations. As mentioned in chapter 3.5.3, the usage of 3D numerical models is preferred in some cases. According to Wyllie and Mah (2004), a three dimensional analysis is preferred when the direction of the principal in-situ stresses are not parallel or perpendicular to the slope. At Preikestolen, the in-situ stress measurements were not perpendicular or parallel, hence if only seen in connection with the in-situ stress, a 3D-model would be preferred. However, the in-situ stress measurements that were used are from a location 25 km away from Preikestolen, and in another topographic location. Due to this, the parameter study presented in chapter 4.5.5 was carried out, and the topography was taken into consideration when evaluating the span of the tested stresses. Therefore, the orientation of the stress is not a strong argument for not using a 2D software in this study.

One of the main factors that makes Preikestolen suitable for 2D modelling, is the orientation of the main structures J2 and J3. The two important joint sets are oriented with a strike almost perfectly perpendicular to the profile, making the situation suitable for 2D modelling. As previously mentioned, Wyllie and Mah (2004) mentions the orientation of important structures as one factor that determines if 2D modelling is suitable. This is supported by Alfonsi et al. (2004), who state that 2D modelling requires cross-sections perpendicular to the strike of important fracture sets to produce a reliable representation of the real situation.

However, one large uncertainty is connected to the use of a 2D model. In previous studies like Böhme (2014) and Sandøy et al. (2017), RS^2 has been shown useful for large slopes, where an infinite extension out of plane is considered to not have a large effect on the simulation. However, the profile of the rock formation crossing Preikestolen, is not representative for the whole slope. For example, if the profile was placed only about

20 meters to the left of Preikestolen, it would have looked entirely different. According to Wyllie and Mah (2004) *"The slope geometry in plan cannot be represented by two-dimensional analysis, which assumes axis-symmetric or plain strain."* Hence the geometry of Preikestolen is not optimal for a 2D-analysis.

When it comes to the profile used for the numerical simulation, the geometry had to be manually adjusted. Originally the profile was exported from a raster created by combining the drone point cloud and a 10 m DEM. However, the profile was exported to RS^2 from a DEM raster, which does not include overhangs or vertical part. Therefore the steepest area in the profile was only represented by a vertical line. To correct for this, several profiles were created in CloudCompare, and used to manually adjust the shape of the steep area. There was a relatively large variation between the shape of the profiles, dependent on the relative placing of it.

Furthermore, the bedrock included in the model was based on observations from the field, and measurements in the 3D model. However, even with the useful measuring-tools in CloudCompare, the boundaries between the granitic gneiss and the porphyritic granite were hard to identify precisely. The boundaries were included in the model as linear boundaries. In reality, the boundary might be more gradient, and hence the rock properties as well. However, a gradual change between the granitic gneiss and the porphyritic granite could not be included in the simulation.

5.2.2 Settings and Input Parameters

A numerical model is not better than the quality of the input data. Hence, high quality input parameters are very important for a good result. According to Manfredini et al. (1975), the parameters in table 5.1 are the minimum parameters needed when analyzing a jointed rock mass. The relative importance of the parameters are also included, ranging from small to considerable.

Table 5.1: Parameters needed to analyse jointed rock mass and their relative importance. Table from Krogh (2017) after Manfredini et al. (1975).

Characteristics	Parameters	Importance
Joint peak strength	Cohesion and friction angle	Basic
Joint brittleness	Residual cohesion and friction angle	Basic
Original state of stress	Horizontal and vertical stress	Considerable
Joint deformability prior to failure	Joint normal and shear stiffness	Moderate
Elastic parameters of the rock mass	Young's modulus and Poisson's ratio	Small

In addition to the mentioned parameters, the effect of groundwater is interpreted as a controlling factor for rock slope failures, and are highlighted in several studies of slope stability like Sandersen (1996) and Grøneng (2010). A lowering of the safety factor due to presence of water was experienced in the numerical simulations from Krogh (2017), Langeland (2014) among several others.

However presence of water is not included in the investigation at Preikestolen. The critical joint at Preikestolen is open on both sides and water pressure can not built up. Besides this crack, the bedrock is very intact and possible water infiltration will be neg-

ligible. However, the presence of water during winter season and the build up of ice, are uncertainties in this study. This would require further investigations.

Furthermore, the orientation of discontinuities are also one of the main controlling factors on slope stability (Hoek and Bray, 1981b; Nilsen, 2000; Wyllie and Mah, 2004; Grøneng, 2010). At Preikestolen, the foliation is oriented with a low dip into the slope. However, the two joint sets J2 and J3 are oriented relatively unfavourable for the stability as presented in chapter 4.4. Hence the joint sets J2 and J3 were included in the numerical simulation.

Stress

Due to the lack of stress measurements at Preikestolen, measurements from Lysebotn found in Hanssen (1998) were used. The stress parameters are expensive and difficult to measure, and hence it is rarely done for slope stability investigations. The stress condition can however have a significant effect on the deformation, and hence the stability. In cases where the material is weakened by internal deformation, the in-situ stresses can have a large effect on the stability Hoek et al. (2000).

Due to the large distance between the stress measurements used, there is a risk that the stress input in the model is slightly wrong. Furthermore, the measurements were taken at a location with the opposite aspect compared to the slope at Preikestolen. As presented in Nilsen and Broch (2011), the stress in mountainous areas will change from location to location dependent on the topography.

The sensitivity of the stress parameters was investigated in the parameter study in chapter 4.5.5. The ratio of the horizontal in plane stress and the vertical stress (σ_H/σ_v) was tested for values from 0.1 to 0.5. Similar, the ratio between the out-of-plane horizontal stress and the vertical stress (σ_h/σ_v) was tested for values ranging from 0.2 to 2.

Due to the topography, the out-of-plane horizontal stress is interpreted to have to potential of being significantly higher than the in plane stress ratio. The stress directed towards the valley sides, have a small potential of building up stress far out on the slope (Figure 5.5). Which of the specific parameters that is best suited is however hard to verify, and this remains one of the largest uncertainties in the model.

As expected, varying the stress parameters in the numerical analysis did change the CSRF, as it both decreased and increased dependent on which of the parameters that were changed. For model 2, the lowest CSRF, 5.92, was found when the stress ratio out-of-plane was increased to 2, while the in plane stress remained unchanged. For this stress setup, also the 2a model resulted in a relatively high CSRF. None of the models were evaluated as sensitive to the out-of-plane stress ratio.

Model 2a obtained the lowest CSRF (for the stress analysis) when the ratio in plane was 0.1. The opposite applies for model 2, as it in fact increased the CSRF from 6.14 (reference value) to 6.15 (at in plane stress ratio of 0.1)

Based on the parameter study, it seems like the factor of safety is lowered when the in plane stress ratio is reduced. This applies for both models. Changing the in plane stress ratio from 0.5 to 0.1 for model 2, while the out of plane stress remained stable, reduced the factor of safety from 6.25 to 6.15. The reduction in the safety factor for model 2a was larger, as it decreased from 4.26 at $\sigma_H/\sigma_v = 0.5$, to 3.86 at $\sigma_H/\sigma_v = 0.1$.
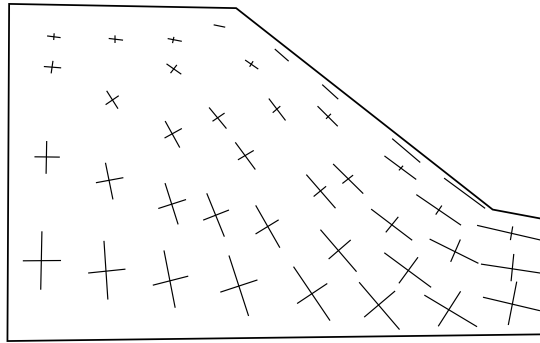
Figure 5.5: Illustration of a homogeneous, isotropic model with interpreted normal tectonic stresses. The lines/crosses represent the direction and the aspect ratio of the stress. Figure from Nilsen and Broch (2011).

However, as increasing the out of plane stress ratio to a factor of 2 did not drastically increase the CSRF, it seems reasonable to base the evaluation of the stability on the measurements from Hanssen (1998).

5.2.3   Rock Mass Parameters

The rock samples were collected in the field from areas nearby Preikestolen, where the rocks had a similar appearance and rock type as the once from Preikestolen. There is a possibility that the samples have a slightly different behaviour than the rocks at Preikestolen itself. It was a challenge to sample bedrock with little or no weathering, as the number of lose blocks in the area were delimited. This resulted in several samples tested in the lab having weathered zones/ weaknesses within them (Figure 5.6). However, there were still enough sample material without visible weathering, which resulted in a sufficient amount of cores.

Due to the lack of sample material of the porphyritic granite, the cores used for the uniaxial compression test, had to be reduced from a planned diameter of 54.2 mm to 40 mm. This issue mainly arised, as one of the blocks had a through going discontinuity cutting the entire block, which made it useless for sampling. As the porphyritic granite contained large crystals of feldspar (Figure 5.7) , this reduction in size was not fortunate.

As explained in chapter 3.3.2, decreasing the sample size might have an effect on the measured UCS. Equation 3.3 can, according to Hoek and Brown (1980a), be used to adjust for variation in sample size. However, the studies from Hawkins (1998) showed that this equation does not apply for samples with a diameter less than 54 mm. In the study from Hawkins (1998), decreasing the diameter of the sample, also reduced the UCS. Nevertheless, no adjustments of the UCS value for the porphyritic granite was done. There might therefore be a possibility of this value being to low.

Furthermore, all remaining values were determined by standards in published literature, explained in chapter 3.5. All parameters thus seems to be in the range of expected values. The samples that showed an odd behavior in the lab, were not used when deter-

Figure 5.6: Granitic gneiss with failure located along a weakness zone in the core. The measurements for this sample were not included in the calculation of the rock mass parameters

Figure 5.7: Sample of the porphyritic granite with several large feldspar crystals present in the sample.

mining the mean value. This especially applied for samples containing weaknesses, where failure occurred along those, before reaching the UCS of the intact rock specimen.

The values were further converted to the equivalent Mohr-Coulomb parameters. This criterion was evaluated as the best suited for model 2 and 2a, as the two joints seen on the plateau of Preikestolen were interpreted as the controlling factors of the stability. The instantaneous Mohr-Coulomb sampler tool in RocData was used for the conversion, in line with the study from Hammah et al. (2004). However, this method is sensitive to the range of normal stress which the envelope is determined at (Hammah et al., 2005). The normal stress was calculated in a very simple manner (Chapter 3.5.5). Due to this, there is an uncertainty related to the instantaneous cohesion and friction angle applied in model 2 and 2a.

Joint parameters

The parameters used when gathering measurements from the joints in this study, were the Barton-Bandis criterion. Therefore the JRC, JCS and ϕ_r were mapped in the field and through laboratory testing. The parameters were determined as presented in chapter 2.2.2, following standards from Wyllie and Mah (2004) and Barton (1973).

Joint shear strength

Some uncertainties are applied to the model by the large amount of parameters. These are especially connected to the joint parameters, JRC and JCS. The JRC for joint set J2 and J3 were only measured in one direction (5.8). In the study from Kveldsvik et al. (2008), the JRC measurements consisted of readings in four directions. Optimally, several directions should have been included at Preikestolen. Furthermore the JRC was only measured on J2 and J3 in the porphyritic granite. Therefore, the JRC used for J2 and J3 in both the granitic gneiss and the porphyritic granite was only measured at the porphyritic granite.
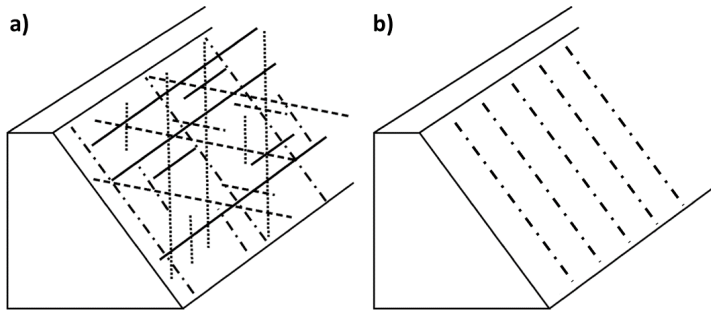
Figure 5.8: Figure modified from Kveldsvik et al. (2008). a) Principle of measuring the JRC in the study from Kveldsvik et al. (2008), including four directions.; b) Representation of how the JRC was measured at Preikestolen.

Furthermore, the JCS used in the modelling corresponds to the UCS measured in the lab. According to Barton and Choubey (1977), the JCS and the UCS can be assumed equal for unweathered rock. The joint surfaces does show little degree of weathering, hence it was evaluated as sufficient to use the UCS as the JCS value. The estimated JCS at Preikestolen was also compared to the standards from ISRM (1981)

Due to a small degree of weathering of the joint surfaces the residual friction angle was estimated to be similar to the basic friction angle measured in the laboratory. According to Bandis (1993), $\phi_r = \phi_b$ can be assumed for most natural unweathered rock samples.

The parameters in the Barton-Bandis criterion were converted to fit the Mohr-Coulomb criterion. This was done in RocData by using the instantaneous Mohr-Coulomb sampler (Appendix 1). The instantaneous friction angle and cohesion of the joints are interpreted to be within a realistic range. Values between $34°$ to $40°$ are typical values for high friction discontinuities (in rocks like granite and basalt) (Wyllie and Mah, 2004).

Changing of the friction angle and the cohesion showed a relatively identical reduction for model 2a. Lowering the friction angle to 50% of the peak value reduced the CSRF

from 4.17 to 2.96. Lowering the cohesion to 50% of peak value gave a almost similar result, reducing the CSRF from 4.17 to 3.02.

When the same analysis was carried out on model 2, the result was different. Reducing the friction angle from peak value to 50% actually increased the CSRF from 6.14 to 6.25, which was an unexpected result. Similar, reducing the cohesion from peak value to 50% reduced the CSRF from 6.14 to 5.69. Based on these findings, the ϕ and c are not interpreted to have the same effect on model 2 as on model 2a, as model 2 is dependent on fracture of the rock at the toe of the slope prior to failure.

Joint stiffness parameters

Even though it exists precise methods for estimating the joint stiffness parameters, the parameters were determined as recommended by Rocscience (2018). Other methods of estimating these parameters are for example tri-axial testing, in-situ measurements and direct shear testing (Rosso, 1976). The calculation used in this study followed the equations from Hoek (2007), as explained in chapter 3.5.6.

The resulting values for the shear (K_s) stiffness of the joints J2 and J3, ranged from K_s = 17.2 GPa/m (J3 in the granitic gneiss) to K_s = 40 GPa/m (J2 in porphyritic granite). Similar the normal stiffness ranged from K_n = 43.3 GPa/m (J3 in the granitic gneiss) to K_n = 105.8 GPa/m (J2 in the porphyritic granite). According to the user manual from UDEC (Itasca, 1996), the shear stiffness for rock joint with clay fillings range from approximately 10-100 MPa/m. For tight joints in for example granite, the shear stiffness can exceed 100 GPa (Itasca, 1996; Wines and Lilly, 2003). The joint stiffness parameters used in the numerical model from Preikestolen therefore seems to be within the expected range. A comparison between the used joint stiffness parameters in this study, and determined stiffness parameters in literature, is given in table 5.2.

When investigating the sensitivity of the joint stiffness parameters, the values were reduced to a value between 5% and 50%. However, the joint stiffness parameters had little effect on the CSRF for both the models. Following table 5.1 from Manfredini et al. (1975), previously presented in this chapter, the joint deformability prior to failure are of moderate importance.

Table 5.2: Joint stiffness parameters for various rock types found in literature.

Rocktype	K_n (GPa/m)	K_s(GPa/m)	Reference
Amphibolite	102.8	40.5	Krogh (2017)
Granitic Gneiss	7	3	Sandøy et al. (2017)
Phyllite	7	1	Böhme et al. (2013)
Gneiss	45	12	Kveldsvik et al. (2008)
Diorite	10	1	Fischer et al. (2010)
Granitic gneiss J2	**65**	**25.8**	**Preikestolen**
Granitic gneiss J3	**43.3**	**17.2**	**Preikestolen**
Porphyrytic granite J2	**105.8**	**40**	**Preikestolen**
Porphyrytic granite J3	**70.5**	**26.7**	**Preikestolen**

5.2.4 Limitations of the Numerical Analysis

Despite a parameter study on several of the parameters used as input was carried out, not all parameters are varied.

Even though the gathering of input data could have been improved, the most uncertain values, are all estimated in a way that is evaluated as sufficient. Furthermore, the values seems to be within the expected range when compared to values obtained in literature. As the samples gathered at Preikestolen were single blocks found in the field, they were to some extent effected by weathering. Also, they were sampled from similar bedrock within the area of Preikestolen, hence the rock properties can vary to some extent from the bedrock at Preikestolen.

I possible, coring of the bedrock in the area to get precise data from the exact rock type in the Preikestolen area should be done. However, this is rarely done for slope stability cases, unless the sliding surface is complex and the consequence of a slide is large, like at the °kneset rock slope. Thus it must be kept in mind that the actual conditions of the rocks might be slightly different than for the once tested in the lab.

To limit the numerical analysis, the effect of earthquakes were not included in the simulation. Crustal earthquakes have triggered many catastrophic rock slope failures (Hermanns and Longva, 2012).

Strong earthquakes can work as trigger mechanisms of massive rock slope failures (Evans et al., 2006). According to Olesen et al. (2013), the highest number of neotectonic earthquakes are reported from the counties Rogaland, Hordaland and Nordland. However, as presented by Olesen et al. (2013), seismicity rates in Norway from the 20th, indicates one magnitude 5 earthquake (or larger) every 8-9 years, and one magnitude 6 (or larger) every 90-100 years.

According to Keefer (1984) and Jibson (1996) the lower value for causing a rock avalanche is magnitude 6. Besides the Storegga slide, there are evidence of earthquake triggered rock avalanches in Norway (Blikra et al., 2006). However, as stated in Keefer (1984) and Evans et al. (2006), rockfalls are the most frequent landslide type triggered by earthquakes. Thus an investigation of the effect of an earthquake at Preikestolen with a magnitude within the expected seismic rates for Norway would be optimal.

As previously stated, it is important to keep in mind that a numerical model is a simplification, and hence requires idealization of the conditions. The numerical simulation produced at Preikestolen, is therefore not an exact estimation, but a useful basis when evaluating the stability.

5.3 Investigation of the Stability at Preikestolen

The geological site investigation done at Preikestolen revealed three important joint sets that dissects the bedrock in the area. The joint sets were J1, J2 and J3 in addition to the foliation. Supplementary investigations of the structural geology was done with the software Coltop 3D, on the LiDAR and SLR 1 model. All joint sets were included in both data sets, hence no important joint sets were overlooked.

All of the joint sets were visible in the field, both in the area around Preikestolen, and close the the rock formation itself. The foliation was measured mainly in the granitic gneiss, and was hard to recognize in the porphyritic granite. This was also the case in the data from the 3D models.

However, the foliation was oriented differently on both measurements from Coltop 3D when compared to the field measurements. The only measurements of foliation included from Coltop 3D were taken from the top plateau at Preikestolen. This plane has a undulating surface, and can explain the change in orientation seen between the field measurements, and the Coltop 3D measurements.

Kinematics

The kinematic analysis was based on the field measurements, as the comparison between the three data-sets from fieldwork, LiDAR and SLR 1 was similar. In theory all failure mechanisms are possible. The kinematic analysis was focused on the Domain 2, that was the domain of Preikestolen.

1. Planar sliding is feasible as failure mechanism, due to the orientation of J3 and (partly) J2. These are oriented with a trike almost perpendicular to the slope, lies within the daylight envelope. The joint sets are also steeper than the friction cone for both the granitic gneiss and the porphyritic granite.

2. Wedge sliding is feasible due to the intersection of the joint sets J1 and J3. The plunge of this intersection is steeper than the friction angle for both rock types.

3. Toppling is feasible due to the orientation of J1 which is steeper than the slip limit (slope angle - friction angle).

The kinematic analysis had some adjustments from the standards recommended in Hermanns et al. (2012b). As explained in chapter 4.4, no lateral limits were included, due to the unusual span of the slide/failure direction. However, as the main focus was on the main rock formation formed by the two joints crossing the plateau. Sliding towards NE and SW was not the main focus. Thus, there might be smaller blocks that are feasible for failure in these directions. The investigations from Sweco (Rohde, 2017) did reveal that smaller potentially unstable blocks are located along the sides of the plateau.

The slope angle used in the kinematic analysis is based on the steep vertical frontal side of Preikestolen. Due to this, the joint set J2 ans J3 seem to daylight the slope. However, further down towards the fjord, the slope is significantly less steep, and day-lighting of joint set J2 and J3 is not possible. Furthermore, in the lower elevations of Preikestolen, the sliding is theoretically not possible in all directions.

Scenarios and Hazard classification

According to the results obtained from the hazard classification, two main scenarios are possible at Preikestolen. Scenario A is calculated to have a volume of approximately 120 000 m^3, and is thus the biggest scenario. Scenario B is calculated to contain a volume of 55 700 m^3. The back scarp is fully open, as can be seen easily in the field and on photographs from the location.

The hazard classification done of the basis of these scenarios, are shown in chapter 4.6. The difference between scenario A and scenario B is mainly due to the difference in opening of the joints crossing the plateau. This does however have a relatively large effect on the risk estimate, as scenario B has a higher hazard score than scenario A.

Otherwise, the values used as input was similar for the two models. A large uncertainty is included in the determination of the hazard class, as no precise deformation measurements exists. This can easily be upgraded whenever measurements are done on the extensometers put up by NGU in September 2017. An upgrade when the first measurements are available will reduce the uncertainty of the hazard score in the risk matrix.

There is a large span in the risk, as it is highly dependent on the number of humans situated at the plateau at the time of failure. The number of humans is highly dependent on the time of year, weak and day. It was estimated that a number exceeding 200 humans at the plateau at the same time would be unlikely or very rear. Therefore the maximum value was set to 200. However, also the amount of humans effected by a potential displacement wave is uncertain. In the evaluation of the consequences for both scenario A and scenario B, no casualties caused by a displacement wave are included in the risk matrix.

The evaluation of not including any casualties caused by a potential displacement wave is based on an unpublished estimate by NGU, indicating a displacement wave that is interpreted to not cause casualties due to a low run-up. However, as no precise simulation of a potential displacement wave is done for Preikestolen, this remains a large uncertainty.

Most part of the possible hazard score for both scenarios, is beneath the 1/5000 annual probability limit (Figure 5.9). However, further investigations to limit the extension of the hazard score are needed prior to determine if Preikestolen should be continuously monitored or not.

5.4 Recommendations for Further Investigations

It is recommended to update the risk matrix for both scenario A and B, once deformation measurements are available. This will limit the uncertainty in the risk-matrix for both scenarios, and will make the decision if Preikestolen should be monitored continuously rather than the present periodic measuring. After this, the further recommendations will be dependent on the updated risk matrix. As the first measurements were read off by NGU during September 2017, the first follow up measurements are planned approximately one year after.

The run out of Preikestolen should also be calculated, as follows in the flowchart in figure 2.3. Furthermore a detailed run up of a potential displacement wave can be calculated, to limit the uncertainties applied by the large span in number of casualties.

Furthermore, a detailed analysis of how a potential earthquake can effect the stability
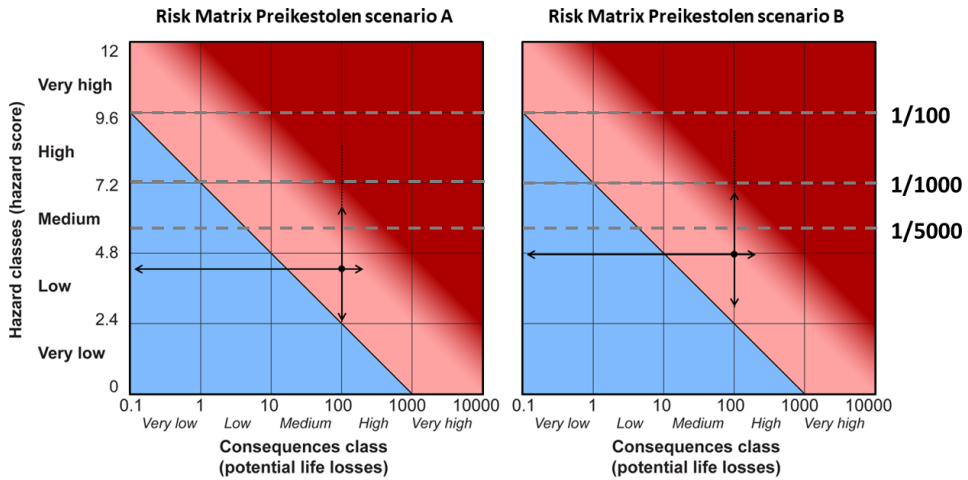
Figure 5.9: The annual probability of failure is added to the matrix of scenario A and scenario B as given in Blikra et al. (2016).

of Preikestolen should be done. Also, the effect of ice/water in the joint and melt freeze cycles can give information, and further delimit the uncertainties of the numerical model. An additional investigation in a 3D software (like FLAC 3D) is also recommended, as the geometry of Preikestolen is interpreted as not optimal for a 2D simulation.

Chapter 6

Conclusion

Based on the factors discussed in chapter 5.1, the following conclusions have been made on 3D modelling:

- Photogrammetry with a high quality SLR camera (in this case a Nikon D 800 with 40 megapixels) is an appropriate method for the use of structural mapping. However, the result is highly dependent on variations in the light conditions. Both situations with brights sun and no clouds (causes shadows) and cloudy conditions (uniformly exposed terrain) can cause challenges.

- The low quality of a photogrammetry model (as shown in SLR 2) can't always be detected in the point spacing. Hence the model should be georeferenced to an existing 1 m DEM, or similar, to investigate the quality.

- Photogrammetry with drone is recommended if the topography allows for en even spread of photos. At Preikestolen, the point spacing in the drone model was significantly higher at the lower elevations, because the majority of the pictures were taken from above the plateau.

- Prior to the collection of field data, throughout planning and evaluations of factors that can effect the quality of the data is important. Such factors include scan position (ground based LiDAR), effect of vegetation (all methods), light conditions (especially photogrammetry), accessibility in the field, etc. Planning is especially important due to challenging topographic and related light conditions in Norway.

The evaluation of the slope stability is based on the obtained results from the numerical analysis, the site investigation and structural analysis of Preikestolen and the surrounding slope.

- Two possible scenarios are present at Preikestolen with calculated volumes of approximately 120 000 m^3 (scenario A) and 55 700 m^3 (scenario B).

- According to the methods used in this study, the critical strength reduction factor (and factor of safety) at Preikestolen indicates a stable situation, as it is larger

than 1, even when important joint parameters obtained from laboratory testing, and RocData are reduced to a value of 50%. Variations of the stress conditions, also produced CSRF significantly higher than 1.

- The lack of a shallow joint set in the rock mass that daylights the slope, and the orientation of the foliation orientation with a shallow dip towards the NW, are to a large degree the reasons for the high CSRF. At present day situation (model 2), the rock mass at the toe at Preikestolen has to fail in order for sliding to occur. However visual inspections from helicopter and on the photogrammetric model do not allow the conclusion that the failure process of the rock mass has initiated.

- The high uniaxial compressive strength for both rock types present at Preikestolen, is also interpreted as a factor that increases the factor of safety significantly.

- Introducing an imaginary joint set in model 2a did lower the stability from a critical strength reduction factor of 6.14 (in model 2) to 4.17. However, the situation is still stable.

- Several uncertainties still exist. These are not expected to change the factor of safety to any severe extent, but nevertheless they should be investigated further. The uncertainties of the evaluation of the stability can be limited to some extent by investigating factors like ice, water, earthquakes. Investigating those further will reduce some of the uncertainties.

Bibliography

Aarseth, I., Austbø, P., Risnes, H., 1997. Seismic stratigraphy of Younger Dryas ice-marginal deposits in western Norwegian fjords. Norsk Geologisk Tidsskrift 77 (2), 65–85.

Abdullah, Q., Bethel, J., Hussain, M., Munjy, R., 2013. Photogrammetric project and mission planning. American Society for Photogrammetry and Remote Sensing: Bethesda, MD, 1187–1220.

Alfonsi, P., Fouche, O., Bourgeois, E., 2004. Foundation on rock: effect of rock fractures on settlement of bridge piers. In: Numerical Modelling of Discrete Materials in Geotechnical Engineering, Civil Engineering and Earth Sciences: Proceedings of the First International UDEC/3DEC Symposium, Bochum, Germany, 29 September-1 October 2004. CRC Press, p. 257.

Alzoubi, A., 2016. Rock slopes processes and recommended methods for analysis. International Journal 11 (25), 2520–2527.

Ambrosi, C., Crosta, G. B., 2011. Valley shape influence on deformation mechanisms of rock slopes. Geological Society, London, Special Publications 351 (1), 215–233.

Ballantyne, C. K., 2002. Paraglacial geomorphology. Quaternary Science Reviews 21 (18), 1935–2017.

Bandis, S., 1993. Engineering properties and characterization of rock discontinuities. Comprehensive Rock Engineering: Principles, Practice and Projects 1, 155–183.

Barton, N., 1973. Review of a new shear-strength criterion for rock joints. Engineering geology 7 (4), 287–332.

Barton, N., 1976. The shear strength of rock and rock joints. In: International Journal of rock mechanics and mining sciences & Geomechanics abstracts. Vol. 13. Elsevier, pp. 255–279.

Barton, N., Bandis, S., 1991. Review of predictive capabilities of JRC-JCS modelin engineering practice.

Barton, N., Choubey, V., 1977. The shear strength of rock joints in theory and practice. Rock Mechanics and Rock Engineering 10 (1), 1–54.

Barton, N., et al., 1978. Suggested methods for the quantitative description of discontinuities in rock masses. ISRM, International Journal of Rock Mechanics and Mining Sciences & Geomechanics Abstracts 15 (6).

Bellian, J. A., Kerans, C., Jennette, D. C., 2005. Digital outcrop models: applications of terrestrial scanning lidar technology in stratigraphic modeling. Journal of sedimentary research 75 (2), 166–176.

Bemis, S. P., Micklethwaite, S., Turner, D., James, M. R., Akciz, S., Thiele, S. T., Bangash, H. A., 2014. Ground-based and UAV-based photogrammetry: A multi-scale, high-resolution mapping tool for structural geology and paleoseismology. Journal of Structural Geology 69, 163–178.

Besl, P. J., McKay, N. D., 1992. Method for registration of 3-D shapes. In: Sensor Fusion IV: Control Paradigms and Data Structures. Vol. 1611. International Society for Optics and Photonics, pp. 586–607.

Birdseye, C. H., 1940. Stereoscopic phototopographic mapping. Annals of the Association of American Geographers 30 (1), 1–24.

Blikra, L., Longva, O., Braathen, A., Anda, E., Dehls, J., Stalsberg, K., 2006. Rock slope failures in Norwegian fjord areas: examples, spatial distribution and temporal pattern. In: Landslides from massive rock slope failure. Springer, pp. 475–496.

Blikra, L., Majala, G., Anda, E., Berg, H., Eikenæs, O., Helgås, G., Oppikofer, T., Hermanns, R., Böhme, M., 2016. Fare-og risikoklassifisering av ustabile fjellparti. Faresoner, arealhandtering og tiltak. In: NVE Report 77/2016, Norwegian Water Ressources and Energy Directorate, Oslo.

Böhme, M., 2014. Spatial and temporal variability of rock slope instability in western Norway:: Implications for susceptibility and hazard assessment.

Böhme, M., Hermanns, R. L., Oppikofer, T., Fischer, L., Bunkholt, H. S., Eiken, T., Pedrazzini, A., Derron, M.-H., Jaboyedoff, M., Blikra, L. H., et al., 2013. Analyzing complex rock slope deformation at Stampa, western Norway, by integrating geomorphology, kinematics and numerical modeling. Engineering geology 154, 116–130.

Bovis, M. J., 1982. Uphill-facing (antislope) scarps in the Coast Mountains, southwest British Columbia. Geological Society of America Bulletin 93 (8), 804–812.

Brady, B. H., Brown, E. T., 2013. Rock mechanics: for underground mining. Springer Science & Business Media.

Buckley, S. J., Howell, J., Enge, H., Kurz, T., 2008. Terrestrial laser scanning in geology: data acquisition, processing and accuracy considerations. Journal of the Geological Society 165 (3), 625–638.

Bungum, H., Lindholm, C., Faleide, J., 2005. Postglacial seismicity offshore mid-Norway with emphasis on spatio-temporal–magnitudal variations. Marine and Petroleum Geology 22 (1), 137–148.

Chen, Y., Medioni, G., 1991. Object modeling by registration of multiple range images. In: Robotics and Automation, 1991. Proceedings., 1991 IEEE International Conference on. IEEE, pp. 2724–2729.

Chugh, A. K., 2003. On the boundary conditions in slope stability analysis. International journal for numerical and analytical methods in geomechanics 27 (11), 905–926.

CloudCompare, 2018. User manual, retrieved 10.02.18 from: http://www.cloudcompare.org/doc/qCC/CloudCompare%20v2.6.1%20-%20user%20manual.pdf.

Coint, N., Slagstad, T., Roberts, N., Marker, M., Røhr, T., Sørensen, B. E., 2015. The Late Mesoproterozoic Sirdal Magmatic Belt, SW Norway: relationships between magmatism and metamorphism and implications for Sveconorwegian orogenesis. Precambrian Research 265, 57–77.

Cruden, D., Varnes, D., 01 1996. Landslide Types and Processes, Special Report , Transportation Research Board, National Academy of Sciences, 247:36-75 247, 76.

Deere, D. U., Miller, R., 1966. Engineering classification and index properties for intact rock. Tech. rep., Illinois Univ At Urbana Dept Of Civil Engineering.

Devoli, G., Eikenæs, O., Taurisano, A., Hermanns, R., Fischer, L., Oppikofer, T., Bunkholt, H., 2011. Plan for skredfarekartlegging–Delrapport steinsprang, steinskred og fjellskred. NVE rapport 15, 2011.

Eardley, A. J., et al., 1942. Aerial photographs: their use and interpretation. Aerial photographs: their use and interpretation.

Eberhardt, E., 2012. The Hoek–Brown failure criterion. In: The ISRM Suggested Methods for Rock Characterization, Testing and Monitoring: 2007-2014. Springer, pp. 233–240.

Eisenbeiß, H., 2009. UAV photogrammetry. Ph.D. thesis, ETH Zurich.

El Bedoui, S., Guglielmi, Y., Lebourg, T., Pérez, J.-L., 2009. Deep-seated failure propagation in a fractured rock slope over 10,000 years: the La Clapière slope, the south-eastern French Alps. Geomorphology 105 (3), 232–238.

Evans, S., Mugnozza, G. S., Strom, A., Hermanns, R., Ischuk, A., Vinnichenko, S., 2006. Landslides from massive rock slope failure and associated phenomena. In: Landslides from massive rock slope failure. Springer, pp. 03–52.

Fischer, L., Amann, F., Moore, J. R., Huggel, C., 2010. Assessment of periglacial slope stability for the 1988 Tschierva rock avalanche (Piz Morteratsch, Switzerland). Engineering Geology 116 (1-2), 32–43.

Fonstad, M. A., Dietrich, J. T., Courville, B. C., Jensen, J. L., Carbonneau, P. E., 2013. Topographic structure from motion: a new development in photogrammetric measurement. Earth Surface Processes and Landforms 38 (4), 421–430.

Furseth, A., 2006. Skredulykker i Norge. Tun Forlag, Oslo 207.

Geertsema, M., Clague, J. J., Schwab, J. W., Evans, S. G., 2006. An overview of recent large catastrophic landslides in northern British Columbia, Canada. Engineering Geology 83 (1), 120–143.

Grøneng, G., 2010. Stability analyses of the Åkneset rock slope, Western Norway.

Grøneng, G., Christiansen, H. H., Nilsen, B., Blikra, L. H., 2011. Meteorological effects on seasonal displacements of the åknes rockslide, western Norway. Landslides 8 (1), 1–15.

Grøneng, G., Nilsen, B., 2008. Procedure for determining input parameters for Barton–Bandis joint shear strength formulation. Tech. rep., Technical Report, Department of Geology and Mineral Resources Engineering, Norwegian University of Science and Technology.

Hammah, R., Yacoub, T., Corkum, B., Curran, J., 2005. The shear strength reduction method for the generalized Hoek-Brown criterion.

Hammah, R., Yacoub, T., Corkum, B., Wibowo, F., Curran, J., 2007. Analysis of blocky rock slopes with finite element shear strength reduction analysis, 329–334.

Hammah, R. E., Curran, H., Yacoub, T., Corkum, B., et al., 2004. Stability analysis of rock slopes using the finite element method.

Hanssen, T., 1998. Rock stresses and tectonic activity. In: Proceedings of the Norwegian National Rock Mechanics Conference. Oslo. pp. 29–1.

Harbitz, C., Glimsdal, S., Løvholt, F., Kveldsvik, V., Pedersen, G., Jensen, A., 2014. Rockslide tsunamis in complex fjords: from an unstable rock slope at åkerneset to tsunami risk in western Norway. Coastal engineering 88, 101–122.

Hawkins, A., 1998. Aspects of rock strength. Bulletin of Engineering Geology and the Environment 57 (1), 17–30.

Hermanns, R., Hansen, L., Sletten, K., Böhme, M., Bunkholt, H., Dehls, J., Eilertsen, R., Fischer, L., LHeureux, J., Høgaas, F., et al., 2012a. Systematic geological mapping for landslide understanding in the Norwegian context. Landslide and engineered slopes: protecting society through improved understanding. Taylor & Francis Group, London, 265–271.

Hermanns, R., Oppikofer, T., Anda, E., Blikra, L., Böhme, M., Bunkholt, H., Crosta, G., Dahle, H., Devoli, G., Fischer, L., et al., 2012b. Recommended hazard and risk classification system for large unstable rock slopes in Norway. NGU report.

Hermanns, R., Oppikofer, T., Anda, E., Blikra, L., Böhme, M., Bunkholt, H., Crosta, G., Dahle, H., Devoli, G., Fischer, L., et al., 2013a. Hazard and risk classification for large unstable rock slopes in Norway. Italian Journal of Engineering Geology and Environment.

Hermanns, R. L., Blikra, L. H., Anda, E., Saintot, A., Dahle, H., Oppikofer, T., Fischer, L., Bunkholt, H., Böhme, M., Dehls, J. F., et al., 2013b. Systematic mapping of large unstable rock slopes in Norway. In: Landslide science and practice. Springer, pp. 29–34.

Hermanns, R. L., Longva, O., 2012. Rapid rock-slope failures. Landslides (types, mechanisms and modeling). Cambridge University Press, Cambridge, 59–70.

Hermanns, R. L., LHeureux, J.-S., Blikra, L. H., 2013c. Landslide triggered tsunami, displacement wave. In: Encyclopedia of Natural Hazards. Springer, pp. 611–615.

Hermanns, R. L., Oppikofer, T., Molina, F. X. Y., Dehls, J. F., Böhme, M., 2014. Approach for systematic rockslide mapping of unstable rock slopes in Norway. In: Landslide Science for a Safer Geoenvironment. Springer, pp. 129–134.

Highland, L., Bobrowsky, P. T., et al., 2008. The landslide handbook: a guide to understanding landslides. US Geological Survey Reston.

Hodgetts, D., 2013. Laser scanning and digital outcrop geology in the petroleum industry: a review. Marine and Petroleum Geology 46, 335–354.

Hoek, E., 1994. Strength of rock and rock masses. ISRM News Journal 2 (2), 4–16.

Hoek, E., 2007. Rock mass properties. Practical rock engineering. Available at www. rocscience. com/learning/hoek-s-corner.

Hoek, E., Bray, J., 1981a. Graphical presentation of geological data. Rock Slope Engineering. Institution of Mining and Metallurgy, Spon Press. London.

Hoek, E., Bray, J. D., 1981b. Rock slope engineering. CRC Press.

Hoek, E., Brown, E. T., 1980a. Empirical strength criterion for rock masses. Journal of Geotechnical and Geoenvironmental Engineering 106 (ASCE 15715).

Hoek, E., Brown, E. T., 1980b. Underground excavations in rock. No. Monograph.

Hoek, E., Carranza-Torres, C., Corkum, B., 2002. Hoek-Brown failure criterion-2002 edition. Proceedings of NARMS-Tac 1, 267–273.

Hoek, E., Kaiser, P. K., Bawden, W. F., 2000. Support of underground excavations in hard rock. CRC Press.

Hungr, O., Leroueil, S., Picarelli, L., 2014. The Varnes classification of landslide types, an update. Landslides 11 (2), 167–194.

ISRM, 1981. Rock characterization testing & [and] monitoring: ISRM suggested methods. Pergamon Press, Oxford, UK.

Itasca, U., 1996. Universal distinct element code. Users Manual 1.

Jaboyedoff, M., Couture, R., Locat, P., 2009. Structural analysis of Turtle Mountain (Alberta) using digital elevation model: toward a progressive failure. Geomorphology 103 (1), 5–16.

Jaboyedoff, M., Metzger, R., Oppikofer, T., Couture, R., Derron, M., Locat, J., Turmel, D., 2007. New insight techniques to analyze rock-slope relief using DEM and 3D-imaging cloud points: Coltop-3d software. In: Rock mechanics: Meeting Societys Challenges and demands. Vol. 1. pp. 61–68.

Jaboyedoff, M., Oppikofer, T., Abellán, A., Derron, M.-H., Loye, A., Metzger, R., Pedrazzini, A., 2012. Use of LIDAR in landslide investigations: a review. Natural hazards 61 (1), 5–28.

Jakobsen, V. U., 2016. An empirical approach for determining the evolution and behavior of rockslide dams.-Development of a empirical tool based on geomorphic parameters of rockslide dams and impounded valleys to predict future rockslide dam heights and their relative longevity. Master's thesis, NTNU.

Jibson, R. W., 1996. Use of landslides for paleoseismic analysis. Engineering geology 43 (4), 291–323.

Jørstad, F., 1956. Fjellskredet ved Tjelle. et 200-årsminne. Naturen". Bergen.

Keefer, D. K., 1984. Landslides caused by earthquakes. Geological Society of America Bulletin 95 (4), 406–421.

Kraus, K., 2007. Photogrammetry: geometry from images and laser scans. Walter de Gruyter.

Kraus, K., Waldhäusl, P., 1993. Photogrammetry: fundamentals and standard processes. Dümmler Köln.

Krogh, K., 2017. The Unstable Rock Slope Kassen-A Hazard, Consequence and Stability Assessment of the Rock Slope. Master's thesis, NTNU.

Kveldsvik, V., Einstein, H. H., Nilsen, B., Blikra, L. H., 2009. Numerical analysis of the 650,000 m2 åknes rock slope based on measured displacements and geotechnical data. Rock mechanics and rock engineering 42 (5), 689.

Kveldsvik, V., Nilsen, B., Einstein, H. H., Nadim, F., 2008. Alternative approaches for analyses of a 100,000 m^3 rock slide based on Barton–Bandis shear strength criterion. Landslides 5 (2), 161–176.

Langeland, H. A., 2014. Utvikling av revidert geologisk modell og stabilitetsanalyser for øvre deler av ustabil fjellside på åknes. Master's thesis, Institutt for geologi og bergteknikk.

Li, C., Zhang, N., Ruiz, J., 2017. Measurement of the basic friction angle of planar rock discontinuities with three rock cores. Bulletin of Engineering Geology and the Environment, 1–10.

Longley, P. A., Goodchild, M. F., Maguire, D. J., Rhind, D. W., 2015. Geographic information science and systems. John Wiley & Sons.

Lorig, L., 1999. Lessons learned from slope stability studies. FLAC and Numerical Modeling in Geomechanics, 17–21.

Manfredini, G., Martinetti, S., Ribacchi, R., et al., 1975. Inadequacy of limiting equilibrium methods for rock slopes design. In: The 16th US Symposium on Rock Mechanics (USRMS). American Rock Mechanics Association.

Marinos, P., Marinos, V., Hoek, E., 2007. Geological Strength Index (GSI). A characterization tool for assessing engineering properties for rock masses. Underground works under special conditions. Taylor and Francis, Lisbon, 13–21.

Marinos, V., Marinos, P., Hoek, E., 2005. The Geological Strength Index: applications and limitations. Bulletin of Engineering Geology and the Environment 64 (1), 55–65.

Markland, J. T., 1973. A useful technique for estimating the stability of rock slopes when the rigid wedge slide type of failure is expected. Interdepartmental Rock Mechanics Project, Imperial College of Science and Technology.

Masoumi, H., Douglas, K., Saydam, S., Hagan, P., et al., 2012. Experimental study of size effects of rock on UCS and point load tests. In: 46th US Rock Mechanics/Geomechanics Symposium. American Rock Mechanics Association.

Moreels, P., Perona, P., 2007. Evaluation of features detectors and descriptors based on 3D objects. International Journal of Computer Vision 73 (3), 263–284.

Morken, O. A., 2017. Integrated analysis of past, and potential future rock slope failures of various size from Rombakstøtta, Nordland. Master's thesis, NTNU.

NGI, 2014. Skred, skredfare og sikringstiltak. Universitetsforlaget.

Nicolet, P., 2017. Quantitative Risk Analysis for Natural Hazards at Local and Regional Scales. Ph.D. thesis.

Nilsen, B., 2000. New trends in rock slope stability analyses. Bulletin of Engineering Geology and the Environment 58 (3), 173–178.

Nilsen, B., Broch, E., 2011. Ingeniørgeologi-berg grunnkurskompendium. Institutt for geologi og bergteknikk, NTNU.

Nilsen, B., Lindstrm, M., Mathiesen, T., Holmy, H., Olsson, R., Palmstrm, A., 2011. Veileder for bruk av Eurocode 7 til bergteknisk prosjektering. bergmekanikkgruppe ed, 7.

Obanawa, H., Hayakawa, Y. S., 2015. High-resolutional topographic survey using small UAV and SfM-MVS technologies in hardly accessible area. In: The International Symposium on Cartography in Internet and Ubiquitous Environment 2015 C. Vol. 4.

Olesen, O., Bungum, H., Dehls, J., Lindholm, C., Pascal, C., Roberts, D., 2013. Neotectonics, seismicity and contemporary stress field in Norway–mechanisms and implications. Quaternary Geology of Norway, Geological Survey of Norway Special Publication 13, 145–174.

Oppikofer, T., 2009. Detection, analysis and monitoring of slope movements by high-resolution digital elevation models.

Oppikofer, T., Böhme, M., Nicolet, P., Penna, I., Hermanns, R., 2016a. Metodikk for konsekvensanalyse av fjellskred. NGU Report 2016.047.

Oppikofer, T., Bunkholt, H., Fischer, L., Saintot, A., Hermanns, R., Carrea, D., Longchamp, C., Derron, M., Michoud, C., Jaboyedoff, M., 2012. Investigation and monitoring of rock slope instabilities in Norway by terrestrial laser scanning. In: Landslides and Engineered Slopes. Protecting Society through Improved Understanding: Proceedings of the 11th International & 2nd North American Symposium on Landslides, Banff, Canada. pp. 3–8.

Oppikofer, T., Hermanns, R., Sandøy, G., Böhme, M., Jaboyedoff, M., Horton, P., Fuchs, H., 2016b. Quantification of casualties from potential rock-slope failures in Norway. In: Landslides and Engineered Slopes. Experience, Theory and Practice-Proceedings of the 12th International Symposium on Landslides. Vol. 3. pp. 1537–1544.

Oppikofer, T., Nordahl, B., Bunkholt, H., Nicolaisen, M., Jarna, A., Iversen, S., Hermanns, R. L., Böhme, M., Molina, F. X. Y., 2015. Database and online map service on unstable rock slopes in NorwayFrom data perpetuation to public information. Geomorphology 249, 69–81.

Optech, 2018. ILRIS-LR Terrestrial Laser Scanner , Summary Specification Sheet, Retrieved 09.05.18 from http://www.teledyneoptech.com/wp-content/uploads/ilris-lr-spec-sheet-140730-web.pdf.

Panthi, K. K., Nilsen, B., 2006. Numerical analysis of stresses and displacements for the Tafjord slide, Norway. Bulletin of Engineering Geology and the Environment 65 (1), 57–63.

Patton, F. D., et al., 1966. Multiple modes of shear failure in rock. In: 1st ISRM Congress. International Society for Rock Mechanics.

Penna, I. M., Abellán, A., Humair, F., Jaboyedoff, M., Daicz, S., Fauqué, L., 2016. The role of tectonic deformation on rock avalanche occurrence in the Pampeanas Ranges, Argentina. Geomorphology.

Raczynski, R. J., 2017. Accuracy analysis of products obtained from UAV-borne photogrammetry influenced by various flight parameters. Master's thesis, NTNU.

Raghuvanshi, T. K., 2017. Plane failure in rock slopes–A review on stability analysis techniques. Journal of King Saud University-Science.

Raskar, R., Agrawal, A., Tumblin, J., 2006. Coded exposure photography: motion deblurring using fluttered shutter. ACM Transactions on Graphics (TOG) 25 (3), 795–804.

Rem, Ø. B., 2016. The Rock Slope Instability at Tytefjell in Vindafjord, Rogaland-Hazard Assessment for Different Failure Scenarios. Master's thesis, NTNU.

Richards, L., Leg, G., Whittle, R., 1978. Appraisal of stability conditions in rock slopes. Foundation engineering in difficult ground. Newnes-Butterworths, London, 449–512.

Rocscience, 2018. RS2, Retrieved 09.05.18 from https://www.rocscience.com/rocscience/products/rs2.

Rohde, K. J., 2017. Stability assessment of the Pulpit Rock. Master's thesis, SWECO.

Rosso, R., 1976. A comparison of joint stiffness measurements in direct shear, triaxial compression, and in situ. In: International Journal of Rock Mechanics and Mining Sciences & Geomechanics Abstracts. Vol. 13. Elsevier, pp. 167–172.

Saintot, A., Henderson, I., Derron, M.-H., 2011. Inheritance of ductile and brittle structures in the development of large rock slope instabilities: examples from western Norway. Geological Society, London, Special Publications 351 (1), 27–78.

Sandersen, F., 1996. Influence of meteorological factors on rock falls and rock slides in Norway. NGI Report, 585910–8.

Sandøy, G., 2012. Back-analysis of the 1756 Tjellefonna rockslide, Langfjorden.

Sandøy, G., Oppikofer, T., Nilsen, B., 2017. Why did the 1756 Tjellefonna rockslide occur? a back-analysis of the largest historic rockslide in Norway. Geomorphology 289, 78–95.

Selby, M. J., et al., 1982. Hillslope materials and processes. Hillslope materials and processes.

Shahbazi, M., Sohn, G., Théau, J., Ménard, P., 2015. UAV-based point cloud generation for open-pit mine modelling. The International Archives of Photogrammetry, Remote Sensing and Spatial Information Sciences 40 (1), 313.

Shan, J., Toth, C. K., 2008. Topographic laser ranging and scanning: principles and processing. CRC press.

Sjöberg, J., 1999. Analysis of large scale rock slopes. Ph.D. thesis, Luleå tekniska universitet.

Slagstad, T., Marker, M., Roberts, N., Coint, N., 2017. NGU Report 2017.030. Norges Geologiske Underskelse 2017.030.

Slagstad, T., Roberts, N. M., Marker, M., Røhr, T. S., Schiellerup, H., 2013. A non-collisional, accretionary Sveconorwegian orogen. Terra Nova 25 (1), 30–37.

Snavely, K. N., 2009. Scene reconstruction and visualization from internet photo collections.

Snavely, N., Seitz, S. M., Szeliski, R., 2006. Photo tourism: exploring photo collections in 3D. In: ACM transactions on graphics (TOG). Vol. 25. ACM, pp. 835–846.

Snavely, N., Seitz, S. M., Szeliski, R., 2008. Modeling the world from internet photo collections. International Journal of Computer Vision 80 (2), 189–210.

Stead, D., Eberhardt, E., Coggan, J., 2006. Developments in the characterization of complex rock slope deformation and failure using numerical modelling techniques. Engineering Geology 83 (1), 217–235.

Sturzenegger, M., Stead, D., 2009. Close-range terrestrial digital photogrammetry and terrestrial laser scanning for discontinuity characterization on rock cuts. Engineering Geology 106 (3-4), 163–182.

Sturzenegger, M., Yan, M., Stead, D., Elmo, D., 2007. Application and limitations of ground-based laser scanning in rock slope characterization. In: Proceedings of the first Canadian US rock mechanics symposium. Vol. 1. pp. 29–36.

Thuro, K., Plinninger, R., Zäh, S., Schütz, S., 2001. Scale effects in rock strength properties. Part 1: Unconfined compressive test and Brazilian test. EUROCK 2001: Rock Mechanics-A Challenge for Society, 169–174.

Varnes, D. J., 1978. Slope movement types and processes. Special report 176, 11–33.

Vestøl, O., 2006. Determination of postglacial land uplift in Fennoscandia from leveling, tide-gauges and continuous gps stations using least squares collocation. Journal of Geodesy 80 (5), 248–258.

Vorren, T., Mangerud, J., 2008. Glaciations come and go. The making of land: geology of Norway. Geological Society of Norway, Trondheim, 481–533.

Wehr, A., Lohr, U., 1999. Airborne laser scanningan introduction and overview. ISPRS Journal of photogrammetry and remote sensing 54 (2-3), 68–82.

Wines, D., Lilly, P., 2003. Estimates of rock joint shear strength in part of the Fimiston open pit operation in Western Australia. International Journal of Rock Mechanics and Mining Sciences 40 (6), 929–937.

Wyllie, D. C., Mah, C., 2004. Rock slope engineering, Civil and Mining, 4 edition, Chapter 4. CRC Press.

Wyrwoll, K.-H., 1977. Causes of rock-slope failure in a cold area: Labrador-Ungava. Geological Society of America Reviews in Engineering Geology 3, 59–67.

Appendix

6.1 Appendix 1
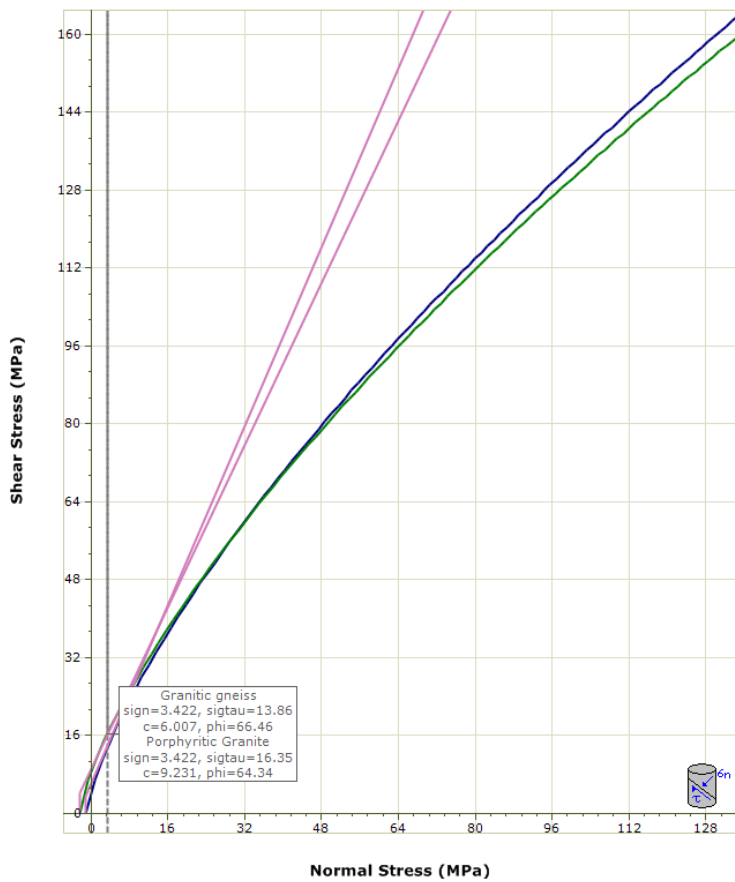
Figure 6.1: Values obtained by using the instantaneous Mohr-Coulomb sampler in RocData. Values obtained for both rock types

Granitic gneiss	
Hoek Brown Classification	
intact uniaxial compressive strength	227 MPa
GSI	75
mi	33
disturbance factor	0
intact modulus	88300 MPa
Hoek Brown Criterion	
mb	13.513
s	0.062
a	0.501
Failure Envelope Range	
application	general
sig3max	56.75 MPa
Mohr Coulomb Fit	
cohesion	22.596 MPa
friction angle	48.15 deg
Rock Mass Parameters	
tensile strength	-1.044 MPa
uniaxial compressive strength	56.46 MPa
global strength	118.192 MPa
modulus of deformation	72083.711 MPa

Figure 6.2: Granitic gneiss from RocData

Porphyritic Granite	
Hoek Brown Classification	
intact uniaxial compressive strength	141 MPa
GSI	90
mi	28
disturbance factor	0
intact modulus	45700 MPa
Hoek Brown Criterion	
mb	19.591
s	0.329
a	0.5
Failure Envelope Range	
application	general
sig3max	35.25 MPa
Mohr Coulomb Fit	
cohesion	18.226 MPa
friction angle	50.736 deg
Rock Mass Parameters	
tensile strength	-2.369 MPa
uniaxial compressive strength	80.881 MPa
global strength	102.189 MPa
modulus of deformation	43808.792 MPa

Figure 6.3: Porphyritic granite from RocData
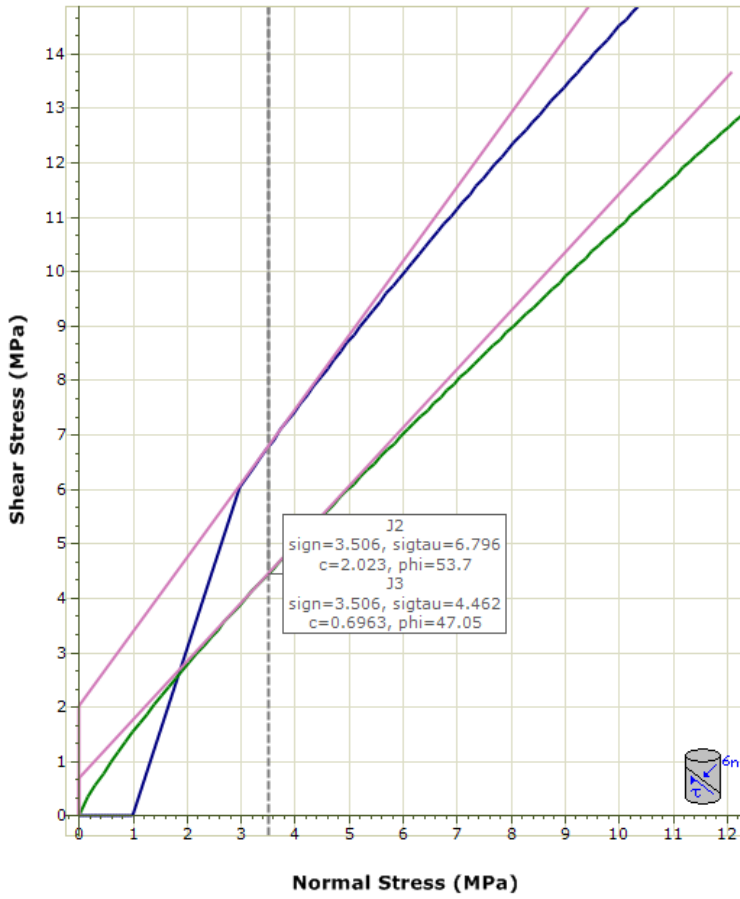
Figure 6.4: Values obtained by using the instantaneous Mohr-Coulomb sampler in RocData. J2 and J3 in granitic gneiss.
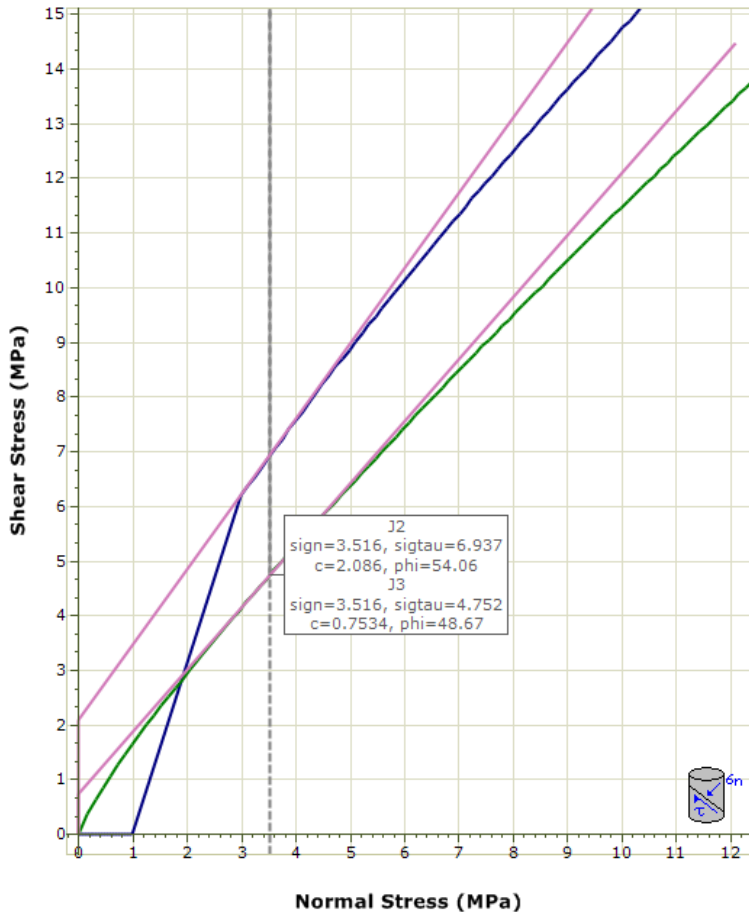
Figure 6.5: Values obtained by using the instantaneous Mohr-Coulomb sampler in RocData. J2 and J3 in porphyritic granite.

J2	
Barton Bandis Criterion	
residual friction angle	37.47 deg
JRCn	16
JCSn	141 MPa
Failure Envelope Range	
application	custom
signmax	10 MPa
Mohr Coulomb Fit	
cohesion	2.406 MPa
friction angle	51.646 deg

Figure 6.6: Values obtained for J2 in porphyritic granite in RocData.

J3	
Barton Bandis Criterion	
residual friction angle	37.47 deg
JRCn	10
JCSn	141 MPa
Failure Envelope Range	
application	custom
signmax	12.08 MPa
Mohr Coulomb Fit	
cohesion	0.828 MPa
friction angle	47.035 deg

Figure 6.7: Values obtained for J3 in porphyritic granite in RocData.

J2	
Barton Bandis Criterion	
residual friction angle	33.73 deg
JRCn	16
JCSn	227 MPa
Failure Envelope Range	
application	custom
signmax	10 MPa
Mohr Coulomb Fit	
cohesion	2.32 MPa
friction angle	51.322 deg

Figure 6.8: Values obtained for J2 in granitic gneiss in RocData.

J3	
Barton Bandis Criterion	
residual friction angle	33.73 deg
JRCn	10
JCSn	227 MPa
Failure Envelope Range	
application	custom
signmax	12.08 MPa
Mohr Coulomb Fit	
cohesion	0.764 MPa
friction angle	45.405 deg

Figure 6.9: Values obtained for J3 in granitic gneiss in RocData.

6.2   Appendix 2

Table 6.1: Table showing the CSRF for model 2a, when decreasing the peak cohesion and peak friction angle by 5%, 10%, 20%, 30% and 50%d .

% reduction of ϕ_{peak}	% reduction of c_{peak}	Model	Joints	CSRF
Peak value	Peak value			4.17
5%	Peak value			4.06
10%	Peak value	2	J2 and J3	3.79
20%	Peak value			3.65
30%	Peak value			3.38
50%	Peak value			2.96
Peak value	Peak value			4.17
Peak value	5%			4.08
Peak value	10%	2	J2 and J3	3.85
Peak value	20%			3.70
Peak value	30%			3.49
Peak value	50%			3.02

Table 6.2: Table showing the CSRF for model 2, when decreasing the peak cohesion and peak friction angle by 5%, 10%, 20%, 30% and 50%.

% reduction of ϕ_{peak}	% reduction of c_{peak}	Model	Joints	CSRF
Peak value	Peak value			6.14
5%	Peak value			6.17
10%	Peak value	2	J2 and J3	6.11
20%	Peak value			6.12
30%	Peak value			6.17
50%	Peak value			6.25
Peak value	Peak value			6.14
Peak value	5%			6.11
Peak value	10%	2	J2 and J3	6.17
Peak value	20%			6.09
Peak value	30%			6.07
Peak value	50%			5.69

Table 6.3: Parameter study of the in plane and out-of-plane stress in model 2 and model 2a.

Stress ratio in plane	Stress ratio out-of-plane	CSRF model 2	CSRF Model 2a
0.296	**0.282**	**6.14**	**4.17**
0.296	0.2	6.17	4.14
0.296	0.4	6.14	4.20
0.296	0.6	6.11	4.14
0.296	0.8	6.10	4.2
0.296	1	6.11	4.2
0.296	2	5.92	4.25
0.1	0.282	6.15	3.86
0.2	0.282	6.13	4.18
0.4	0.282	6.16	4.19
0.5	0.282	6.25	4.26

Table 6.4: Overview of the obtained values from simulations where the peak value of both the normal stiffness (K_n) and the shear stiffness (K_s) was reduced by 5%, 10%, 20%, 30% and 50%.

Reduction (K_n)	Reduction (K_s)	CSRF Model 2	CSRF Model 2a
Peak value	**Peak value**	**6.14**	**4.17**
5%	5%	6.19	4.17
10%	10%	6.12	4.2
20%	20%	6.22	4.14
30%	30%	6.11	4.11
50%	50%	6.10	4.06

6.3 Appendix 3

<div align="center">

Table 6.5: Scenario A

</div>

1. Back-scarp	Score	Norm. prob
Not developed	0	0.0%
Partly open over width of slide body (few cm to m)	0.5	100.0%
Fully open over width of slide body (few cm to m)	1	0.0%
Back-scarp partly open across the plateau		
2. Potential sliding structures		
No penetrative structures dip out of the slope	0	66.7%
Penetrative structures dip on average < 20 degree or steeper than the slope	0.5	0.0%
Penetrative structures dip on average > 20 degree and daylight with the slope	1	33.3%
One well developed joint set which also causes large surfaces outside of the unstable area.		
This could create a coherent sliding surface. Not certain if the joint set is really penetrative.		
3. Lateral release surface		
Not developed	0	0.0%
Partly developed on 1 side	0.25	0.0%
Fully developed or free slope on 1 side or partly developed on 2 sides	0.5	0.0%
Fully developed or free slope on 1 side and partly developed on 1 side	0.75	0.0%
Fully developed or free slope on 2 sides	1	100.0%
Both flanks are free to move.		
4. Kinematic feasibility test		
Kinematic feasibility test does not allow for planar sliding, wedge sliding or toppling	0	0.0%
Failure is partly kinematically possible (movement direction is more than ± 30 ° to slope orientation)	0.5	0.0%
Failure is kinematically possible (movement direction is less than ± 30 ° to slope orientation)	0.75	0.0%
Failure is partly kinematically possible on persistant discontinuities (movement direction is more than ± 30 ° to slope orientation)	0.75	0.0%
Failure is kinematically possible on persistent discontinuities (movement direction is less than ± 30 ° to slope orientation)	1	100.0%
Sliding is possible along one persistent joint set.		
5. Morphologic expression of the rupture surface		
No indication on slope morphology	0	60.0%
Slope morphology suggests formation of a rupture surface (bulging, concavity-convexity, springs)	0.5	20.0%
Continuous rupture surface is suggested by slope morphology and can be mapped out	1	20.0%
No indications of a lower boundary or a developed sliding surface. Because of the risk of		
toppling, the uncertainty is included.		
6. Displacement rates		
No significant movement	0	50.0%
0.2 - 0.5 cm/year	1	33.3%
0.5 - 1 cm/year	2	16.7%
1 - 4 cm/year	3	0.0%
4 - 10 cm/year	4	0.0%
> 10 cm/year	5	0.0%
insecure measurements shows no movements, however small movements would not have		
been measured in these.		
7. Acceleration (if velocity is > 0.5 cm/yr and < 10cm/yr		
No acceleration or change in displacement rates	0	50.0%
Increase in displacement rates	1	50.0%
No information		
8. Increase of rock fall activity		
No increase of rock fall activity	0	100.0%
Increase of rock fall activity	1	0.0%
Similar as the surrounding rock slope		
9. Past events		
No post-glacial events of similar size	0	50.0%
One or several events older than 5000 years of similar size	0.5	25.0%
One or several events younger than 5000 years of similar size	1	25.0%
No bathymetric data available		

Table 6.6: Scenario B

1. Back-scarp	Score	Norm. prob
Not developed	0	0.0%
Partly open over width of slide body (few cm to m)	0.5	0.0%
Fully open over width of slide body (few cm to m)	1	100.0%

Back-scarp fully open across the plateau

2. Potential sliding structures

No penetrative structures dip out of the slope	0	66.7%
Penetrative structures dip on average < 20 degree or steeper than the slope	0.5	0.0%
Penetrative structures dip on average > 20 degree and daylight with the slope	1	33.3%

One well developed joint set which also causes large surfaces outside of the unstable area.
This could create a coherent sliding surface. Not certain if the joint set is really penetrative.

3. Lateral release surface

Not developped	0	0.0%
Partly developped on 1 side	0.25	0.0%
Fully developped or free slope on 1 side or partly developped on 2 sides	0.5	0.0%
Fully developped or free slope on 1 side and partly developped on 1 side	0.75	0.0%
Fully developped or free slope on 2 sides	1	100.0%

Both flanks are free to move.

4. Kinematic feasibility test

Kinematic feasibility test does not allow for planar sliding, wedge sliding or toppling	0	0.0%
Failure is partly kinematically possible (movement direction is more than ± 30 ° to slope orientation)	0.5	0.0%
Failure is kinematically possible (movement direction is less than ± 30 ° to slope orientation)	0.75	0.0%
Failure is partly kinematically possible on persistant discontinuities (movement direction is more than ± 30 ° to slope orientation)	0.75	0.0%
Failure is kinematically possible on persistent discontinuities (movement direction is less than ± 30 ° to slope orientation)	1	100.0%

Sliding is possible along one persistent joint set.

5. Morphologic expression of the rupture surface

No indication on slope morphology	0	60.0%
Slope morphology suggests formation of a rupture surface (bulging, concavity-convexity, springs)	0.5	20.0%
Continuous rupture surface is suggested by slope morphology and can be mapped out	1	20.0%

No indications of a lower boundary or a developed sliding surface. Because of the risk of
toppling, the uncertainty is included.

6. Displacement rates

No significant movement	0	50.0%
0.2 - 0.5 cm/year	1	33.3%
0.5 - 1 cm/year	2	16.7%
1 - 4 cm/year	3	0.0%
4 - 10 cm/year	4	0.0%
> 10 cm/year	5	0.0%

No information

7. Acceleration (if velocity is > 0.5 cm/yr and < 10cm/yr)

No acceleration or change in displacement rates	0	50.0%
Increase in displacement rates	1	50.0%

No information

8. Increase of rock fall activity

No increase of rock fall activity	0	100.0%
Increase of rock fall activity	1	0.0%

Similar as the surrounding rock slope

9. Past events

No post-glacial events of similar size	0	50.0%
One or several events older than 5000 years of similar size	0.5	25.0%
One or several events younger than 5000 years of similar size	1	25.0%

No bathymetric data available